Tactile Sensing Based on Gallium Nitride Light-Emitting Diodes

by

Nathan Dvořák

A dissertation submitted in partial fulfillment
of the requirements for the degree of
Doctor of Philosophy
(Electrical and Computer Engineering)
in the University of Michigan
2024

Doctoral Committee:

Professor Pei-Cheng Ku, Chair
Assistant Professor Nima Fazeli
Professor Zetian Mi
Professor Amit Misra
Professor Euisik Yoon

Nathan A. Dvořák

nadvorak@umich.edu

ORCID iD: 0000-0002-9925-649X

Dedication

To my family and those I met along the way.

Acknowledgements

I would like to express my deepest gratitude to all the people who have supported me throughout my graduate education. The support of my advisor, Dr. Pei-Cheng Ku, whose patience and persistence kept me focused with end goals always in sight. I was not destined for graduate school, but PC decided to take a chance on me. His willingness to “go out on a limb” allowed me to begin my career as an academic. I am especially appreciative of his hands-on advisement strategy, his method of advisement made sure I never struggled too long on a task. The inclusion of weekly meetings ensured I stayed motivated through my graduate studies. Thank you, PC.

My sincere gratitude goes to my dissertation committee members: Professors Zetian Mi, Euisik Yoon, Amit Misra, and Nima Fazeli for their constructive feedback and faith in my ability to produce meaningful research. I would like to thank Professor Nima Fazeli for offering his lab and group for collaboration. Together we found some interesting applications of MichTac, thank you.

To my family and friends who supported me during my graduate studies. Without your support I would not have been able to explore. Without your support I would not have been able to finish this.

I would like to thank the knowledgeable faculty and staff of the Lurie Nanofabrication Facility who have made this work possible through guidance and process education.

My deepest appreciation goes out to the National Science Foundation Graduate Research Fellowship Program. The NSF GRFP made this work possible.

Table of Contents

List of Tables

List of Figures

List of Appendices

Abstract

In this dissertation we propose and demonstrate a novel tactile sensor, MichTac. MichTac uses gallium nitride (GaN) light-emitting diodes (LED) nanopillars. Tactile sensing modes demonstrate shear force measurement in ambient and extreme conditions, contact patch measurement, force mapping, high frequency response, tactile morse code reading, and liquid leak detections. MichTac detects tactile sensation by monitoring the shear force applied on the nanopillars. This shear force causes the electrons and holes to separate in the radial direction and reduces the light intensity emitted from the nanopillars. We developed a toolkit to custom-design MichTac based on the intended application.

We demonstrate MichTac's directional sensitivity and capability of mapping at a high spatial resolution (3.72μm) with a dynamic range of 1 – 30 mN and an accuracy of ±1.3 mN. We also demonstrate tracking and mapping of an external force moving across the sensor array. We further reduce the footprint of MichTac by devising an electrically driven version. The functionality of the proposed tactile sensor was verified both numerically and experimentally.

After proof-of-concept experiments and numerical calculations are performed we calibrate the MichTac to measure the absolute magnitude and direction of an applied shear force without the need for any post-processing of data or finite element analysis. Calibration of the tactile sensor used a commercial force/torque (F/T) sensor. The results confirmed the direct measurement of shear stress from 3.71 to 50 kPa, which is in the range of interest for completing robotic tasks such as grasping, pose estimation, and item discovery.

Lastly, we use MichTac to perform real-world tactile sensing and perceptions tasks. The MichTac sensor decodes micro-scale messages (200 µm) like a robotic Braille reader, detects micro leaks in pipes, and achieves tactile perception within a region which simulates the hull of the International Space Station, a high vacuum (10^{-6} Torr) cryogenic (-196 ºC) environment. What sets this innovation apart is its incredible sensitivity, adaptability, and resilience. Its compact size and numerous sensing elements enable seamless integration into diverse applications, from artificial skins to expansive robotic systems. Furthermore, the sensor employs a sophisticated method of measuring intensity changes, adapting dynamically to different surfaces and maintaining accuracy even in the face of potential damage. In essence, our MichTac sensor provides a novel and robust method for tactile perception. Opening new frontiers in medicine, industry, and beyond, it enables robots with superhuman touch to comprehend, manipulate, and navigate the world.

Chapter 1 Introduction

Tactile sensing and perception is one of the important skills humans use every day. The simple act of grasping requires multiple types and a high density of mechanoreceptors. Humans develop skills of delicate manipulation and grasp at an early age [1]. We do not merely sense the pressure from touching an object, but a combination of different measurements (size, shape, temperature, etc.) view occur within our figure tips as we explore the world around us. We use our fingertips for recognizing subtle surface textures to prevent slips when grasping an object. Slip occurs when the shear force applied by the contact patch is insufficient to balance out external forces (e.g., gravity and/or external contacts) applied to the object. Studies have shown that humans modulate their grasp forces to maintain a margin above the minimum threshold required to prevent slipping [2]–[4]. Localized slip and shear forces are monitored by using mechanoreceptors at the fingertips which modulate grasping forces to ensure stable grasps. These mechanoreceptors sense low magnitude shear forces and their directions with high spatial resolution (40 μm) [2], [3], [5]. Monitoring and control are primarily subconscious and adaptive to various external factors, such as changes in physical properties (e.g., the addition of dirt or liquids) and external forces. When gliding across a surface, our fingertips send signals to the brain with both spatial and temporal patterns, further augmenting our ability to sense beyond the pitch of the ridges of our fingertips [6]. For example, studies have shown our ability to perceive sub-micron features on a surface [7].

1.1 Motivation of this Work

Imbuing robots with the ability to sense and interpret touch far beyond the capability of humans will unlock a new realm of dexterity, precision, and adaptability in both normal and extreme environments. Development of a tactile sensing platform will grant robots the ability to read micron-scale Braille which is hidden from human sight and touch, detect tumors and other pathologies through palpation, and detect minute leaks in critical flow systems. Beyond perception, robots will be able to perform intricate tasks that demand fine motor skills, such as threading a needle, assembling intricate electronic components, and handling fragile objects with unparalleled gentleness. In fields such as healthcare, robots with tactile perception can conduct delicate surgeries with greater precision and safety. Moreover, tactile perception has the potential to revolutionize human-robot collaboration, making it safer and more efficient across various industries, from logistics, construction, and space exploration to improving the lives of people who require at home care thus allowing them to have their needs fulfilled.

1.2 Tactile Sensor Platform Configuration

The pursuit of tactile sensing has resulted in various innovations aimed at replicating human tactile senses. This makes the task of replicating human capabilities with dexterous robotic hands extremely challenging. Each sensing element in a tactile sensor consists of two parts:

1. A transducer whose property is modified because of the mechanical interactions between the sensor and its surrounding environment.
2. A readout device that converts the physical property of the transducer to a signal conducive to digital computing [8].

Designing a tactile sensor which contains both parts often results in a battle between sensor size, speed, and accuracy. The premiere methods of tactile sensing and perception offer high accuracy but lack in sensing speed or generalizability grasping techniques due to their data hungry nature [9], [10]. In the next section we are going to cover the methods of transduction of tactile forces and specific applications.

1.3 State of the Art

Numerous transduction principles for tactile sensing and perception have been explored [11], such as resistance [12]–[18], capacitance [19]–[23], optics [24]–[26], magnetic and magnetoresistance [27]–[31], and barometric pressure [32]. The sensor's physical resolution is determined not only by the size of each sensing element but also by the practical considerations of reliably integrating a high enough density of sensing element to approach the resolution of human fingertips (~40 μm) and allowing for robust operation in real-world situations. One must also consider the overhead necessary to enable the detection of the contact force's direction, either in a form of increased physical dimension with additional sensing elements or complex signal processing extracting information from multiple sensing elements. Within the following subsections we will cover a few tactile sensors and their force transduction methods.

1.3.1 Resistive Tactile Sensors

The term resistive tactile sensors cover a wide range of methods for detecting tactile forces. Edward Simmons and Arthur Ruge invented the first resistive strain gauge in 1938. Simmons and Ruge used thin metallic wires to measure the strain on a surface. As the surface is strained the wires stretch or contract thus causing the length and cross-sectional area of the wires to change. Since the resistance of a wire is determined by

$$R = \frac{\rho L}{A} \tag{1-1}$$

where $R =$ resistance (Ω), $\rho =$ resistivity (Ωm), $L =$ length (m), and $A =$ cross-sectional area (m^2). Figure 1-1 demonstrates the effect of stain on the cross-sectional area and length of a strain gauge. For both tensile and compressive loads a change in resistance is observed.

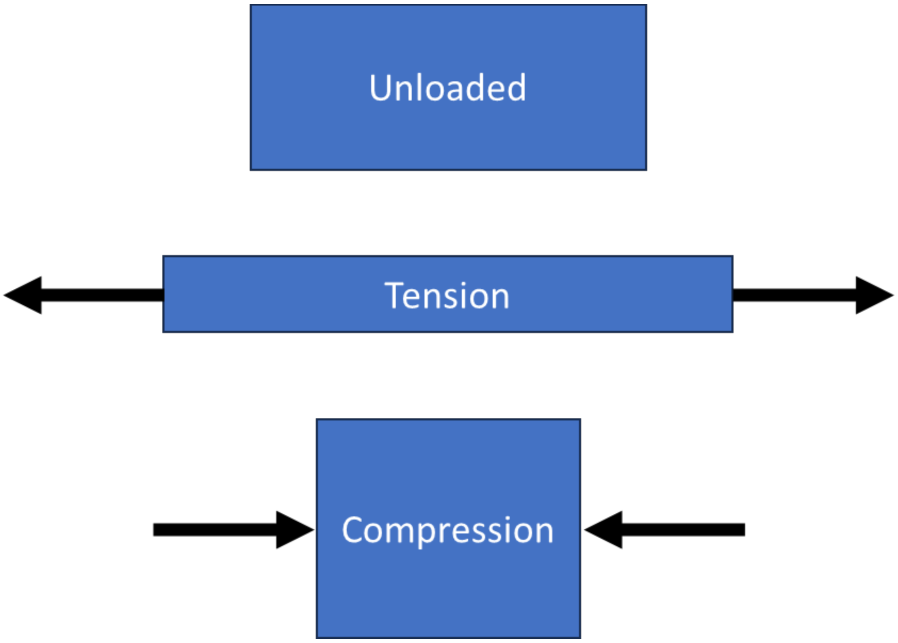

Figure 1-1: Example of the effect of uniaxial load on the length and cross-sectional area of a strain gauge.

Therefore, by monitoring the resistance across the strain gauge to a known reference the strain can be deduced. Modern strain gauges rely on metal foil on polymer substrates such as polyimide or epoxy resin. These metal foils typically consist of nichrome or constantan. Unfortunately, these sensors are subject to thermal expansion and creep effects. Changes in temperature cause changes in the length of the strain gauge and extreme temperature affect the stiffness of the polymer substrate which produces inaccurate measurements of strain. Under constant load or cyclic loading these strain gauges tend to walk out of calibration thus reducing the life of the strain sensor [33].

The figure of merit which determines the quality of a strain gauge is referred to as the Gauge Factor (GF), which is defined by

$$GF = \frac{\Delta R}{R} \cdot \frac{L}{\Delta L} \tag{1-2}$$

where metal-based strain gauges have Gauge Factors between 2.0 and 4.5. Semiconductors also can function as strain gauges, in fact semiconductor strain gauges have 2 to 3 orders of magnitude higher Gauge Factors (~150). Higher Gauge Factors are made possible within semiconductor strain gauges by taking advantage of piezoresistive effects. These effects are prominent within silicon, germanium, and gallium nitride [34]. An advantage of semiconductor strain gauges is their ability to be fabricated using standard microfabrication techniques, thus allowing for small yet highly sensitive strain gauges. With some clever engineering a metallic or semiconductor strain gauge can be configured into networks to perceive tactile forces such as shear and normal loads.

In recent years a method of measuring tactile forces using resistance measured across conductive polymers has been developed. Yellapantula et. al. 2020 developed a resistive array of carbon pillars embedded into a polymer skin. The carbon pillars have a height of 4 mm and were formed by embedding the polymer with carbon powder. Two grids of electrical grid are formed on each end of the carbon pillars using the same carbon powder embedded polymer. A schematic of Yellapantula's resistive tactile sensor is depicted in Figure 1-2.

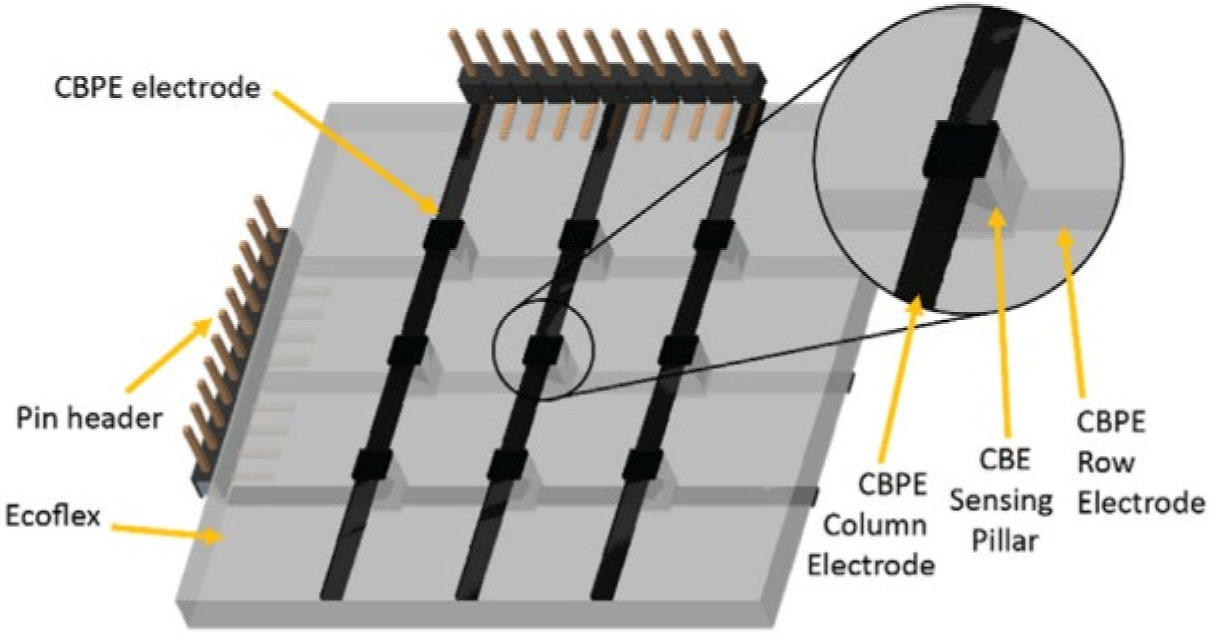

Figure 1-2: Schematic of a resistive tactile sensor which utilizes carbon embedded polymer as a transducer. Adapted from [35]

The sensing circuit sweeps across each three input and three output combinations, thus resulting in 9 combinations, and monitors the relative change in the resistance of each path. Under normal force applied to the carbon pillar grid a data processing unit can create a loading map and deduce the shape and distribution of force across the sensor grid. Increasing the number of sensing nodes would require complex circuitry and increase the power consumption and the polymer construction is not resilient enough for regions of extreme heat and cold.

1.3.1.1 Capacitive Tactile Sensors

Within our daily lives capacitive tactile sensors are considered essential for completing tasks demanded by work and society. The default method for sensing fingertip interaction is capacitance. Every day we interact with touch actuated displays and track pads on computers. Since 2010 the default method for operating a touch display has been capacitive sensing. The display is operated by measuring localized changes in capacitance induced through the display by our fingertips. This method of transduction is efficient in locating multiple points of contact with high precision. Capacitive touch displays benefit from microfabrication techniques which allow for a high density of transducers, but require high material quality, clean manufacturing spaces, and complex circuity. Traditional capacitive displays cannot measure forces directly.

A method of deducing forces using a capacitive tactile sensor is reported by Lee, et.al. in 2008. Lee's method utilizes a polymer-based MEMS (Micro Electrical Mechanical System) and FEM (Finite Element Method) simulations to decode measured capacitances into applied tactile forces. Figure 1-3 depicts the structure and operational principle of Lee's capacitive MEMS tactile sensor.

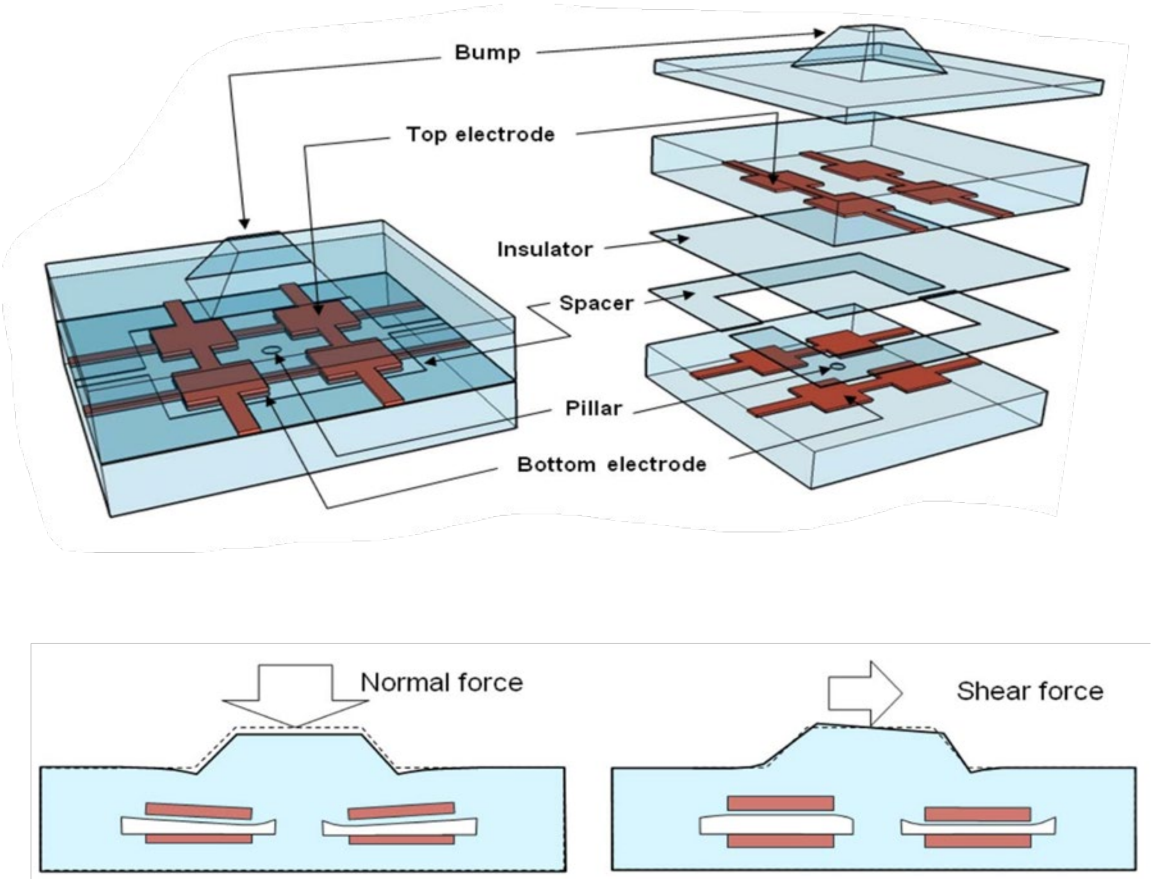

Figure 1-3: Schematic and operational principle of a capacitive tactile sensor. A polymer bump acts as a transducer. When normal and shear forces are applied to the transducer the airgap between the plates of four capacitive sensors changes, and by monitoring the relative change in capacitance between the four sensing elements the type of force (normal vs. shear) and the direction of the applied force can be deduced. Adapted from [36].

Lee's tactile sensor senses tactile forces by monitoring the change in conductance of four parallel plate capacitors. When tactile force is applied to the polymer bump either an increase or decrease of the capacitance in each parallel plate capacitor is observed. Capacitance (C) is defined as the ratio of the electric charge (Q) to the electric potential (V) which is depicted in Equation (1-3).

$$C = \frac{Q}{V} \tag{1-3}$$

For a parallel palate capacitor with a dielectric, such as air, between the plates the capacitance is defined as

$$C = \kappa \epsilon_0 \frac{A}{d} \tag{1-4}$$

where κ is the dielectric constant of the dielectric medium, $\epsilon_0$is the permittivity of free space, A is the area of the parallel plates, and d is the separation between the plates. Therefore, if all four plates observe an increase in measured capacitance, then a normal force pushing down the polymer bump is detected. If two of the plates detect a decrease in capacitance and the other two plates detect an increase in capacitance then a shear force is known to be applied to the polymer bump. The tactile sensor described above is excellent in determining type and direction of a tactile force, but FEM simulations are required to quantify the applied tactile forces, and the polymer construction is not durable enough for extreme environments.

1.3.2 Magnetic Tactile Sensors

Tactile sensing can be achieved using the Hall effect. Yan et. al. 2021 designed a tactile sensor which utilizes magnetic particles embedded into a Polydimethylsiloxane (PDMS) substrate and a Hall effect sensor separated by a polymer sheet. The hall sensor acts as compass and under no applied force the "virtual needle" points at the center of the PDMS substrate. When normal and shear forces are applied to the PDMS the magnetic field distorts within the polymer sheet thus deflecting the "virtual needle" of the hall sensor. The hall sensor measures the magnitude and direction of deflection to classify between normal and shear forces [11]. Yan's sensor can be fabricated into a sensing matrix using simple "pick and place" manufacturing. Machine learning can be used to increase the resolution of the sensing matrix by using multiple nodes to determine what forces act between the sensing elements. The spatial resolution is limited by the footprint of the Hall effect sensors (~25 mm^2) and achieving high spatial resolution would require minimization of the Hall effect sensor and added complex circuitry add more sensing nodes. The polymers used for this sensor are not suitable for regions of extreme cold due to the polymer becoming stiffer when cooled. High temperature applications would be damaging to the Hall effect sensor and its driving components.

1.3.3 Optical Tactile Sensors

Optical tactile sensors are viable alternative to the resistive, capacitive, and magnetic approaches while offering higher spatial resolution (5 – 30 μm) and high number of transducers (> 10^6) [25], [26], [45]–[53], [37]–[44]. Within the optical tactile sensor category there emerges two methods of transduction: material change monitoring and vison-based machine learning. Material change monitoring involves observing changes in optical properties to measure applied tactile forces. This type does not require imaging optics, thus making a thin-film sensor form factor possible by bonding the transducer directly to spectrometers or image sensors. One example utilizes ZnO nanowires coupled to a GaN LED substrate act as a material change force transducer. Under applied normal force a forward bias is induced within ZnO nanowires. This forward bias causes an increase in the depletion region of the GaN LED thus causing an increase in the recombination rate of the charge carriers. When the recombination rate of the charge carriers increases the GaN LED emits brighter underneath nanowires which experience compressive strain, therefore normal pressure can be deduced by observing the change in brightness of the GaN LED. Figure 1-4 shows a schematic of

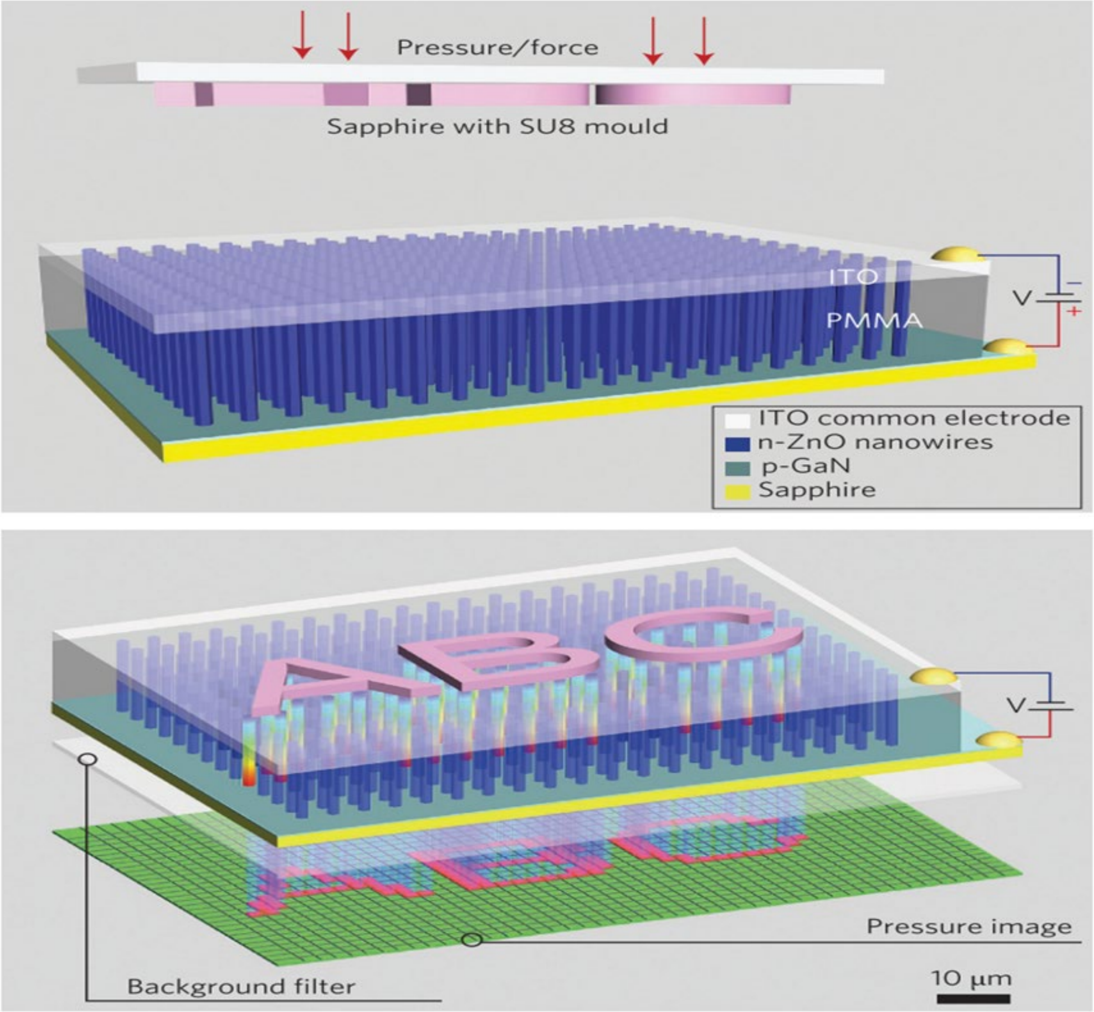

Figure 1-4: Schematic of and measurement output of ZnO nanowire tactile sensor. Adapted from [38].

Vision based tactile sensors measure imprints made on deformable media caused by contact with a surface [9], [10], [54], [55]. These measurements are made using RGB (red, green , blue) or depth cameras and have proven effective for pose estimation and extrinsic contact detection for the grasped object [56]–[58]. However, to convert these vision-based signatures to forces, inverse Finite Element Methods (FEMs) need to be employed [59] which can be computationally expensive and challenging to tune. Prior work has focused on detecting slip using a purely geometric approach (i.e., sensor gel deformation) without computing forces [60]. This approach relies on a rigidity assumption and careful thresholding that can be difficult to tune in practice. Further, it cannot estimate external forces applied to the grasped object without additional sensing apparatus.

There are two premiere vision based tactile transducers: GelSlim 3.0 and Soft Bubble. Both transducers employ a deformable membrane with printed tracking dots. Monitoring the motion of these tracking dots allows for classification of force types (normal, shear, and rotational) along with the contact patch measurements. A rotational force interaction with a GelSlim 3.0 sensor is depicted in Figure 1-5. Under normal force the shape and size of the contact patch is determined by monitoring translation direction and magnitude of the tracking dots. Within a GelSlim 3.0 sensor there are three colors of LED (red, green, and blue). When the face of a surface is parallel to one colored LED the transducer membrane reflects the respective color of light, thus allowing for 3D reconstructions of the contact patch. With reverse FEM and machine learning, forces applied to the transducer head of GelSlim 3.0 can be determined. Unfortunately, reverse FEM simulations can vary greatly depending on who designed the simulation and which assumptions are used to best approximate the ideal contact scenario. Machnine learning tends to require enormous data sets and experience generalization challenges.

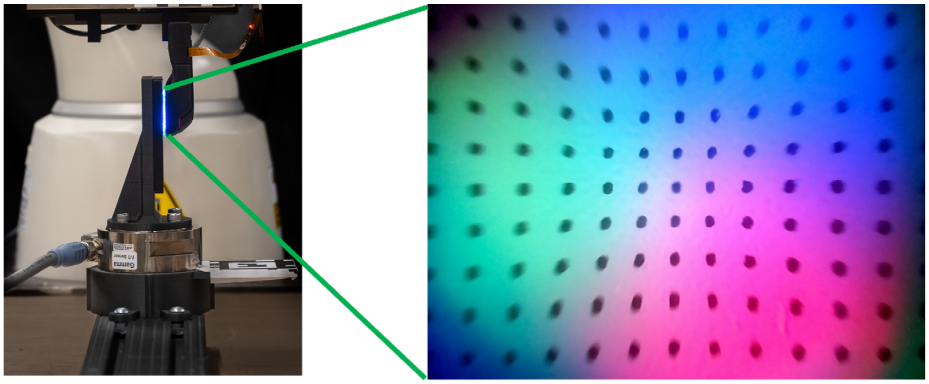

GeSlim 3.0 Dot Tracking Matrix

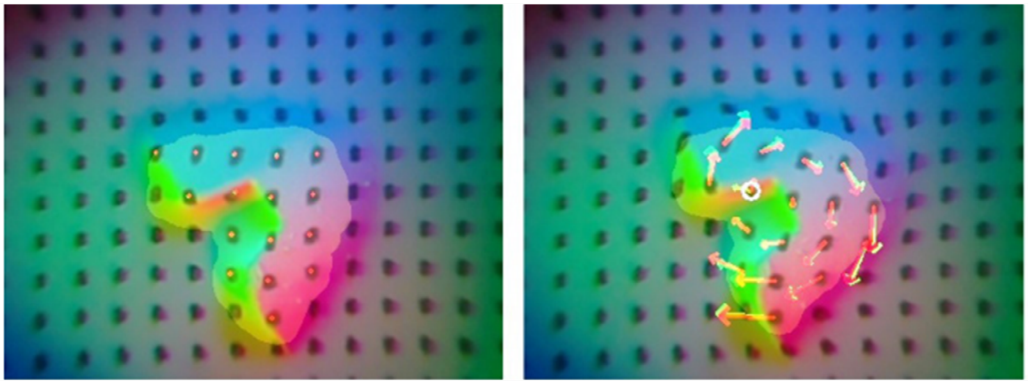

Normal Force Contact Rotational Force

Figure 1-5: Top Left – Gelslim 3.0 tactile sensor. Top Right – RGB image of the tracking dot matrix on the deformable sensing membrane. Bottom Left – Initial normal force contact on an arbitrary surface. Bottom Right – Example of an applied rotational force to the arbitrary surface. The center of rotation is determined by the tracking dot with the least amount of displacement. Bottom Left and Right are adapted from [54].

1.4 Tactile Sensors Figures of Merit

Shear stress sensing with a high spatial resolution, fast response, and good sensitivity are all crucial resources for robotic grasp and maneuvering [10], [26], [54], [57], artificial skin [12], [61], [62], rehabilitation engineering [63], [64], form metrology [35], [65], [66], and fluid shear force monitoring [67], [68]. A tactile sensor which surpasses current techniques will be able to:

1. Measure the direction and magnitude of applied shear forces. The measurement of these applied shear forces should match the dynamic range and perception of human fingertips. (0-1 MPa at 100 Hz) [69].

2. Have a spatial resolution which meets or exceeds the average density mechanoreceptors within a human hand (40 µm [2]).
3. Be fabricated from robust materials to survive many loading cycles.
4. Verification of application, which requires demonstration of tactile sensing in a non-laboratory environment.

Consideration of all these points during the sensor design process is essential for creating a tactile sensor which will survive outside an academic environment. A comparison of the different tactile sensing and perception techniques is collected in Table 1-1.

Table 1-1: Summary of tactile sensing and perception techniques previously discussed.

Senor Class	Transducer	Signal Detection	Pros	Shortcomings
Resistive	Conductive polymers or Strain Gauges	Current measurement or resistance change.	• Simple to manufacture single transducers.	• Requires complex circuitry. • Material quality affects sensor performance. • Difficult to scale. • Extremely sensitive to temperature fluctuations. • Not suited for extreme environments.
Capacitive	Polymer bumps	Parallel plate capacitors.	• Mature microprocessing techniques allow for repeatable production.	• FEM simulations are required to determine how forces effect the polymer. • Not suited for extreme environments.
Magnetic	Magnetic particles embedded in polymer.	Hall effect sensors.	• Simple to manufacture. • Advanced data processing techniques can increase sensor resolution.	• Low spatial resolution. • High number • Not suited for extreme environments.
Material Change	Semiconductors with novel geometries.	Commercial CMOS image.	• Transducer can be decoupled form data collection and processing equipment. • Sensor performance is not dependent on material quality. • Extreme environment applications.	• More expensive materials. • Less mature manufacturing techniques.
Vision Based	Deformable media	Commercial CMOS imager and machine learning.	• Mature technology. • Vison based approaches utilize machine learning for qualitative analysis.	• Vison based approaches detect tactile interaction through inference. • Vision based approaches are data hungry and lack generalizability. • Not suited for extreme environments.

1.5 Research Needs

Within this thesis we have explored various types of force transducers for tactile sensing. Optical transducers show the highest potential for development of a tactile sensor which mimics or exceeds human abilities. Such transducers sense tactile forces by monitoring the movement of an array of markers printed on an elastomeric material [26], detecting light leaked through an optical waveguide bent or deformed by the force [40], [52], deflecting the direction of light propagation from a deformed structure [25], [46]. These modalities rely on passive elastic materials illuminated by an external light source and the analysis of the optical images' time evolution because of the applied force. The system is often bulky to accommodate the light emitter, space necessary for a proper image formation, and photodetectors. Using an active elastic material eliminates the need for a separate light source and the optics necessary for the formation of a sharp image, allowing a low-profile tactile sensor to be designed with the chip scale integration of a silicon-based image sensor.

The study of tactile sensing and perception would benefit from a tactile sensor which mimics or exceeds human capabilities. A sensor which stands apart from current methodologies would address the following research challenges:

1. Development of a force transducer which is reactive to shear force to mimic the grasping feedback of human fingertips. A successful tactile sensor would have a high enough density of force transducers to mirror human fingertips [2]. These force sensors should be biocompatible and able to operate within a wide range of environments (low pressure and large temperature range).
2. Formalization of a methodology to predict the response and dynamic range of the force transducer.

3. Verification of tactile sensor calibration within laboratory and real-world applications.

Recently, a method of measuring the shear force based on GaN nanostructures was reported [71]. Instead of inducing a change of resistance or capacitance, the device used optically active piezoelectric nanostructures. The stress-induced change in the electronic band structure was monitored by measuring the light emission using a photodetector. The length scale of the band structure change is approximately 100 nm along the nanopillar's radial direction, which enables a potentially submicron spatial resolution for sensing [73]. The detection of the force’s direction is enabled by breaking the nanopillar’s structural symmetry, e.g., using an elliptically shaped nanopillar.

Gallium nitride is a relatively new material to be considered for tactile sensing applications [74]. While LEDs have been incorporated in optical tactile sensor designs, their utility is often limited to providing a baseline signal that is to be modulated by force transduction in another material, such as an elastomer. There are distinct advantages of using GaN semiconductors for tactile sensing. First, thanks to their large bandgap, the rugged nature of GaN semiconductors enables the sensor to function effectively beyond normal conditions, including a broad range of temperatures, corrosive environments, and radiation bombardments. Second, monitoring the optical intensity change can be achieved from a large selection of off-the-shelf image sensors without requiring a custom-design ASIC (application-specific integrated circuit). To date, however, while the feasibility of using GaN LEDs for pressure mapping and local force sensing with directional sensitivity and a spatial resolution far exceeding human capability has been demonstrated, no reports have directly documented the use case of a GaN tactile sensor on a robotic platform and benchmarked its performance against several widely used devices such as GelSight, GelSlim, and Soft Bubble.

1.6 Research Objectives

This research's main objective is to develop an ultrathin, modular tactile sensing platform, MichTac. A tactile sensing platform is not just a single device, but a system. The design of the device requires multiple parallel processes to ensure it can perform within the desired parameters of a specific application. The formalization and development of a simulation toolkit to intelligently inform device design and manufacture which will yield a device which performs as intended. Development of data collection hardware and analysis software which are light weight enough to make MichTac practical and field deployable. The creation of repeatable scenarios which mimic real world applications which evaluate the performance of MichTac. The major challenge this work faces is developing a sensor which brings novel functionality and superior performance when compared with other well established tactile sensing/perception techniques (GelSlim and Soft Bubble). Demonstration of MichTac within real world applications and comparison to GelSlim and Soft Bubble remains the key goal.

1.7 Research Contributions

The proposed research has provided the following key contributions:

- Development of a sensor design toolkit. This toolkit is used to tailor MichTac based on the operational parameter of a potential application [72].
- Determination of shear force direction and magnitude. Contact patch mapping of applied shear forces using time evolution analysis [72].
- Verification of magnitude of applied shear force [75].

- Development of ultrathin, conformal contacts for and electrically biased tactile sensor [76].
- Demonstration of unique tactile sensing applications which exceed the capabilities of existing tactile/touch perception sensors.

1.8 Thesis Overview

This work focuses on the utilization of GaN LEDs for tactile sensing where local strain engineering is used as the sensing mechanism. The application of tactile forces changes the band structure of the GaN LEDs in real time thus changing the optical properties of the LEDs. Chapter 2 offers an overview of the operational principle of MichTac sensing platform and the tested configuration of MichTac. A brief overview of device physics is discussed along with the manufacturing process is detailed. Chapter 3 provides and deep dive into the physics of a single sensing element on MichTac and how the mechanics of tactile sensing are handled within a simulation process. We call this simulation process the device design toolkit. The toolkit allows for multiple configurations of MichTac such as optically and electrically driven sensor along with contact patch calculations to explore how MichTac interacts with a deformable surface at a sub-micron scale (~650 nm). Chapter 4 covers the evaluation of MichTac's various configurations and sensing modes (static and time evolution analysis) and the calibration of MichTac. Chapter 5 delivers real world applications of MichTac. Comparison tasks are completed and MichTac is evaluated against other tactile sensors. Chapter 6 offers future work which could improve the MichTac platform.

Chapter 2 MichTac – A New Feeling

Within this chapter two chip level configurations of MichTac proposed and discussed: a standard image-optics-based configuration with a passive GaN sensing chip powered by an external light source such as a 405 nm laser diode or LED, and a thin-and-light configuration by directly stacking an active, electrically-pumped GaN sensing chip on top of the CMOS imager with no image optics.

2.1 Nanopillar Tactile Sensing

We designed the MichTac sensor based on local strain engineering in GaN LEDs. Local strain engineering locally modifies the strain in a material or structure to tune the optoelectronic properties. It has been initially applied to 2D materials and extended later to semiconductors with a large piezoelectric coefficient, such as GaN and ZnO. MichTac's main operation principle relies on locally changing the strain distribution in a GaN LED, which comprises a series of InGaN/GaN quantum wells sandwiched between a GaN pn junction. The InGaN/GaN quantum wells are responsible for light emission when electrons and holes are generated under excitation either electrically with an electric current injected via the GaN pn junction or optically with an external laser or LED. Fermi's golden rule governs the LED's light emission intensity, which depends on the electrons and holes' locations. Efficient light emission requires electrons and holes to be co-located. Any separation between the electrons and holes reduces the emission intensity. When a force is applied to an LED inside the MichTac sensor, the electrons and holes in the LED's quantum wells will be displaced, reducing the light emission intensity.

The first iteration of Optically Biased MichTac
was fabricated by Dr. Kunook Chung.

The strain can be intrinsic due to the lattice mismatch in a heterostructure or extrinsic due to an external force that deforms the crystal structure. The latter is typically negligible in a thin-film structure but can become significant in a nanostructure in which lattice deformation is possible even with a small external force. For example, in a GaN nanopillar structure shown in Figure 1B, a shear force applied at the top of the nanopillar can create a nonuniform strain profile in the radial direction, leading to the separation of electrons and holes along that direction and lowering the radiative efficiency. As the strain profile naturally terminates at the circumference of the nanopillars, the effect is localized, and the amount of electric potential change is entirely determined by an isolated strain profile within each nanopillar. We dub this phenomenon as local strain engineering, a method for one to tune the electronic and optoelectronic properties locally via simple geometric parameters including height, width, and shape of the nanopillars. Local strain engineering in GaN has enabled site-controlled single photon emitters as well as monolithic integration of multi-color LEDs and photodetectors by spatially modulating the intrinsic strain profile. Local strain engineering has also enabled force sensing with directional sensitivity by monitoring the light emission intensity from individual nanopillars which changes when the strain profile is modulated by an external force. As the width of the nanopillar is on the order of no more than a few hundred nanometers to provide sufficient sensitivity for tactile perception, a GaN-nanopillar-based tactile sensor has the potential to achieve superhuman capabilities.

We add directional sensitivity by further breaking the symmetry in the azimuthal direction, e.g., using nanopillars with an elliptical cross section. The electron-hole separation is less restricted along the ellipse's long axis, making the light intensity change more sensitive to the applied force. The long axis allows for greater separation of the electron-hole wavefunction due to the increased space available. This principle was previously demonstrated using optically excited GaN nanopillars. The force's direction can be unambiguously measured within a 90º range and expanded to 360º by analyzing the time evolution of the intensity map.

MichTac is designed to achieve two goals: 1.) measure the location, magnitude, and direction of a localized shear force; and 2.) generate the map of a force field. A matrix of sensing nodes allows for mapping of applied shear forces across MichTac. Each sensor node was comprised of two independent sensors responsible for identifying the force in two different directions. We will refer to these two sensors as "X Sensor" and "Y Sensor," respectively in the following discussions. The design is illustrated in Figure 2-1A in which the green-colored rectangular bars represent the X and Y sensors in each sensor node [77]. Both the X and Y sensors were made of an array of GaN nanopillars. The nanopillar's epitaxial structure is the same as that of a standard LED. Each nanopillar also has an elliptical cross-section, as shown in Figure 2-1B. The ellipse's orientations in the X and Y sensors are orthogonal to each other (Figure 2-1C). As an external shear force is applied on a nanopillar, its light emission intensity is reduced. The reduction is largest when the force's direction is parallel to the ellipse's long axis. Hence, using two orthogonally oriented, elliptically shaped nanopillar building blocks enables us to directly measure an external force's magnitude and direction. The height, width, and the shape (i.e., the ellipse's aspect ratio) were chosen to achieve a force sensitivity suitable for tactile perception in the range of 1 ~ 1 MPa. We validated the design using commercial CAD tools including Comsol and nextnano. The design was then transferred to a CAD drawing for patterning the nanopillar LEDs using lithography and etching. The fabrication process was the same as a standard thin-film LED.

Tactile sensing was achieved by monitoring the intensity change of individual nanopillar LEDs or a subset of them for a better signal-to-noise ratio from the CMOS imager. While strain-induced electric potential changes both the emission wavelength and intensity, we chose to monitor only the intensity as it is directly proportional to the external shear force and can be easily achieved by an off-the-shelf image sensor. It is also highly scalable and tolerant to fabrication nonuniformity. Figure 2-2 shows the image of individual nanopillars using fluorescent microscopy (Olympus BX 51). In more practical settings, lower-cost image sensors and simpler image optics will only detect a group of instead of individual nanopillars' emission. In the optics-free configuration, the spatial resolution can be even less without the image formation and without removing the substrate. In terms of the fabrication tolerance, as we are only concerned about the relative intensity change, the design intrinsically tolerant to nonuniformity in fabrication or aging. Dead emitters also do not affect the sensing performance of live ones.

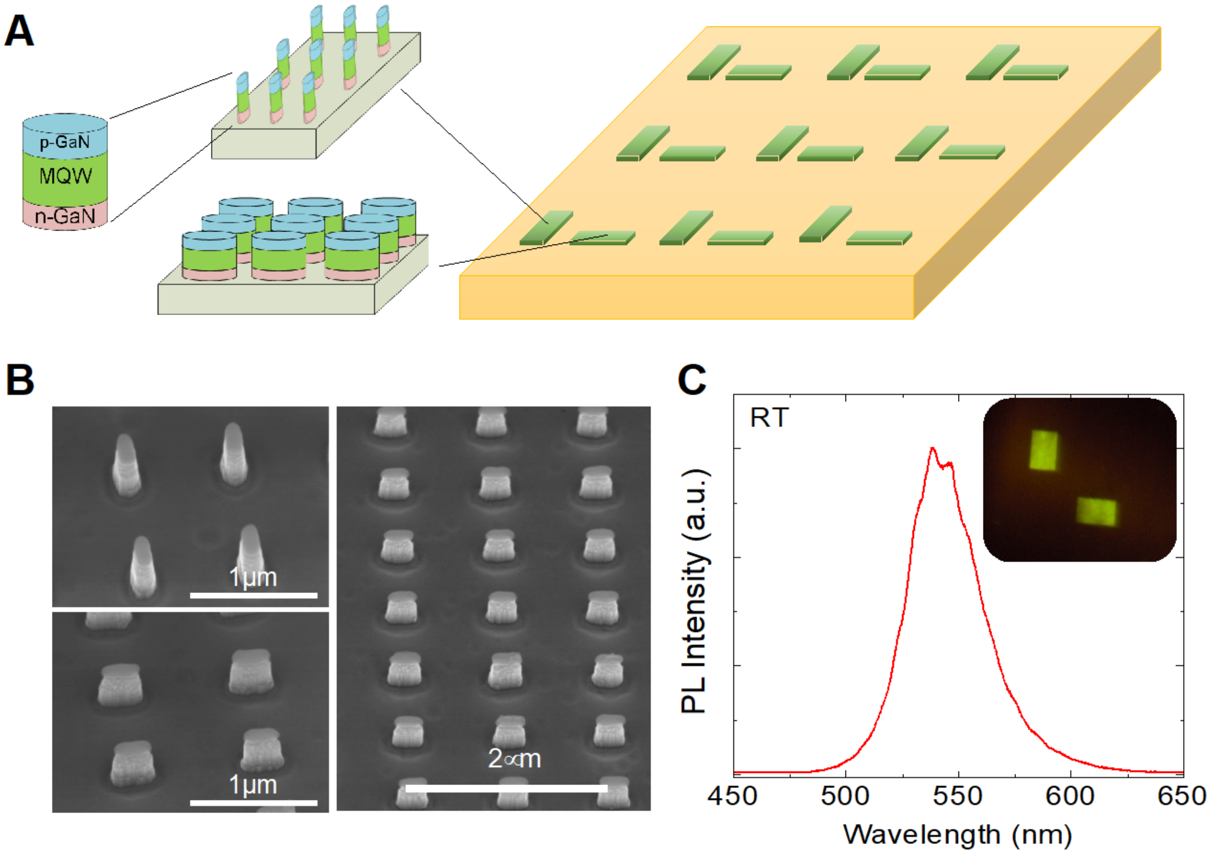

Figure 2-1: (A) The design and device structure of the proposed tactile sensor. The device consists of 64 sensor nodes arranged into an 8x8 pattern. Each sensor node further consists of two GaN nanopillar-LED-based sensors represented by the green-colored rectangular bars. Each LED's dimension is 100µm x 150µm and the distance between two sensor nodes is 1 mm, making the total sensor area the size of a person's fingertip. Each LED was made of 100 x 125 nanopillars with pillar-to-pillar spacings of 1µm and 1.2µm, respectively. The nanopillar's epitaxial structure is the same as a green-emitting LED. (B) Scanning electron microscope images of the elliptically shaped nanopillar LEDs. The left two images show the high-resolution images of the two LEDs of orthogonally oriented nanopillars. The right image shows the nanopillar array. (C) Room-temperature photoluminescence spectrum and optical image (inset) of a sensor node. The long edge of each rectangle was parallel to the constituent nanopillar's elliptical cross section's long axis, for the convenience of identifying the directionality of each sensor. Adapted from [72].

2.2 Optically Biased MichTac

Once the device is fabricated, the GaN sensing chip is integrated with a silicon CMOS image sensor. In practical applications, the image-optics configuration allows a protective housing to enclose all active and dedicate components and lets only the GaN sensing chip to be exposed to the environment while the optics-free configuration can be suitable for applications beyond robotics such as prosthetics in which case the substrates of the GaN sensing chip can be removed and a flexible image sensor can be chosen to enable a flexible version of the tactile sensor. Figure 2-2 shows an array of optically-pumped nanopillar LEDs.

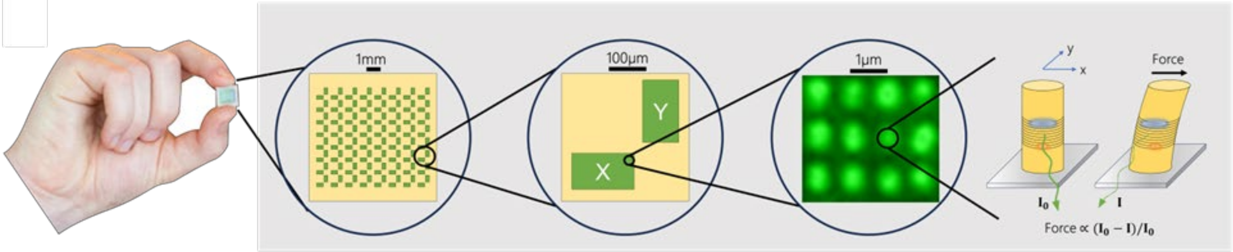

Figure 2-2: Demonstration of scale of MichTac. The scape progressively zooms in from left to right. The second from the right is an image of individual nanopillars. The image was captured on an Olympus BX-51 Fluorescence microscope. The furthest to the right demonstrates the operational principle of a single nanopillar under applied shear force.

We designed the tactile sensor based on an array of nanopillar-shaped GaN LEDs as shown in the scanning electron microscope image in Figure 2-3A. Each nanopillar's elliptical cross-section has dimensions of 360 nm × 120 nm. Upon the formation of the nanopillar geometry, the strain around the perimeter is relaxed more than that at the center, resulting in a slightly larger bandgap around the perimeter to confine the electrons and holes toward the center of the nanopillar [23].

When an external shear force is applied to the tip of the nanopillar, the nanopillar is deformed and the radial symmetry is broken, thus resulting in a redistribution of the electron and hole wavefunctions in the InGaN/GaN quantum wells as shown in Figure 2-3B, reducing the light emission intensity. The deformation of the nanopillar increases the tensile strain on one side and the compressive strain at the other, forcing the electron to move opposite to the force's direction, along the radial axis of the nanopillar. The hole's movement is restricted due to its large effective mass. The separation of the electron and hole reduces the light emission intensity. Owing to the strong piezoelectric effect, the GaN nanopillar LEDs can function as a tactile sensor in combination with a photodetector array, such as a CMOS imager, simply by monitoring the relative intensity change gives us a direct measurement of the force's magnitude.

Due to the elliptical cross-section, the wavefunction redistribution responds asymmetrically to the applied shear forces. The long (360 nm) axis of the nanopillar is more sensitive to forces than the short (120nm) because there is more space for the electron and hole to separate as opposed to the short axis. The sensor's capability to measure the force's direction is achieved by having two types of nanopillar arrays whose elliptical cross-sections are orthogonal to each other. Measuring the relative intensity changes of the two arrays simultaneously (see Figure 4-7) enables the reconstruction of a shear force at an arbitrary angle from orthogonal components parallel to the long and short axis of the elliptical cross-section and time evolution analysis.

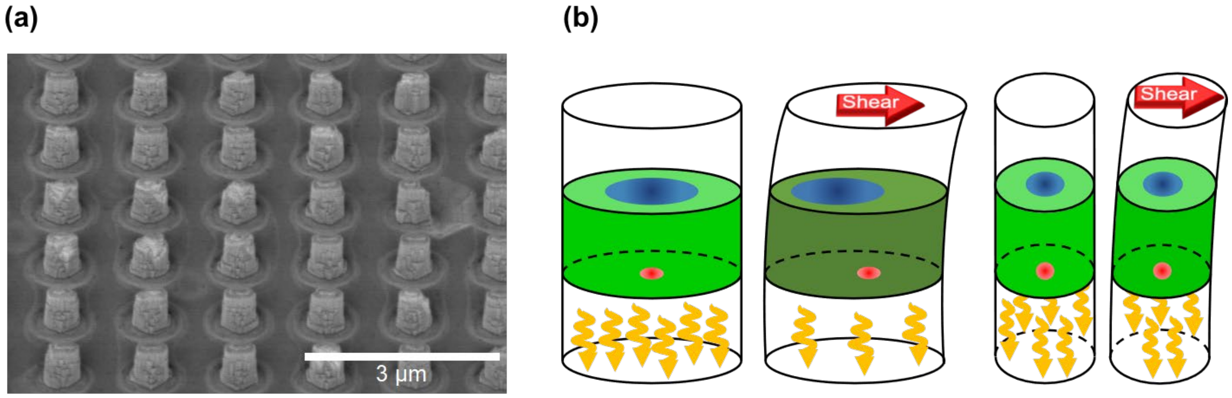

Figure 2-3: (A) Scanning electron micrograph (SEM) of an array of nanopillar-shaped light-emitting diodes. Each nanopillar has an elliptically shaped cross-section. Directional tactile sensing is achieved with two groups of nanopillar LEDs with their ellipses orthogonally oriented (the second orientation is not shown in the SEM image here). The height-to-width ratios are 2 and 4 when measured from the long and short axes, respectively. The nanopillar LEDs can be optically [72] or electrically biased [76]. (B) Illustration of the operating principle of the tactile sensor. The shear force applied to the tip of the nanopillar deforms the nanopillar and shifts the electron (blue) and hole (red) wavefunctions. Holes remain unmoved at the center due to their large effective mass. Electrons move against the direction of the force. When the electron and hole wavefunctions are misaligned, the emission intensity is reduced. Monitoring the relative change of the emission in-tensity allows one to measure the force's magnitude. The nanopillar's finite dimension limits the travel of the electrons. The elliptically shaped cross-section leads to a different number of travels for the electrons. The difference in emission intensity allows us to determine the force's direction. Adapted from [78].

2.3 Electrically Biased MichTac

In this section, we reduce MichTac's volume by eliminating the imaging optical path. Having imaging optics and a pump laser works fine for benchtop applications, but these imaging optics, CMOS imager, and pump laser all separate add significant bulk to our tactile sensor.

Removal of the imaging optics is essential for transitioning the nanopillar tactile sensor from laboratory applications to a field deployable system. Removal of the optical path for data acquisition is essential for the development of an all-in-one sensor.

We made an ultrathin platform by removing the need for imaging optics and a pump laser. fabricated an electrically biased tactile sensor. We eliminated the biasing laser by producing an electrically biased version of our tactile sensor. To enable electrical excitation while maintaining the flexibility of the GaN nanopillar geometry, we formed the p-contact using the atomic layer deposition (ALD; Veeco Fiji). The ALD technique allows us to deposit ultrathin layers of both dielectric and metallic materials that conform to the nanopillar structure as illustrated in Figure 2-5(C-F). We used SiO_2 to provide electrical insulation between the p-contact and the n-GaN. We chose Pt as the p-type Ohmic contact due to its excellent ductility [79]–[81].

The monitoring of the tactile sensor is achieved by mounting the tactile sensor directly to a CMOS imager, by having the tactile sensor and CMOS imager in direct contact there is no need for imaging optics to resolve the arrays on the nanopillars. We purchased a commercially available CMOS imager (Raspberry Pi Hi-Q Camera). The Raspberry Pi Hi-Q camera was chosen due to its small footprint, ease of programming, low cost, application flexibility, available documentation, and low light sensitivity. The Raspberry Pi Hi-Q camera was driven by a Raspberry Pi 3 Model B+ because the Cameral Serial Interface (CSI) port on the Raspberry Pi 3 allowed for control of the Raspberry Pi Hi-Q camera's gain, white balance, framerate, and saturation. Fixing all these image variables prevents the CMOS imager from automatically correcting the brightness and color of the nanopillar emissions, thus not causing false positives during tactile sensing. We 3D printed a housing for the tactile sensor. The 3D printed housing contains the CMOS imager, an infrared optical filter, and the nanopillar tactile sensor. The infrared optical filter increases the accuracy of

CMOS imager by removing intrinsic infrared noise from the environment. A cutaway schematic is depicted below in Figure 2-4.

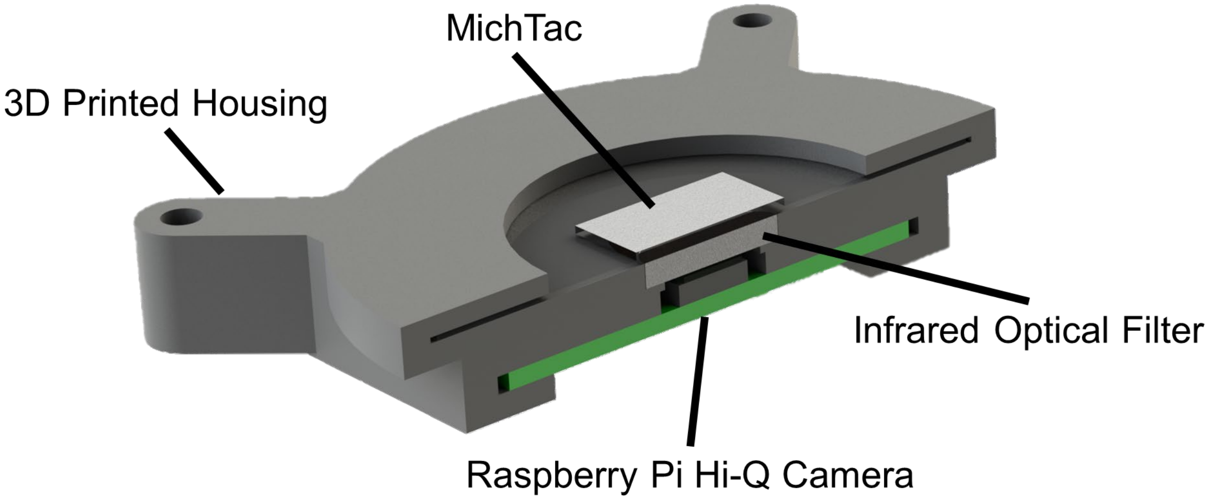

Figure 2-4: Cutaway schematic of the electrically biased MichTac configuration. For simplicity, the computer (Raspberry Pi 3 Model B+) has been omitted.

2.4 Fabrication

MichTac is fabricated from a commercially available thin film green emitting LED. The GaN semiconductor is shaped into a nanopillar geometry as illustrated in Figure 2-5(A-B). The sample was grown by metal-organic chemical vapor deposition (MOCVD) on a c-plane sapphire substrate. The epitaxial stack is grown in the order of n-doped GaN, then multi-quantum wells active region of InGaN alloy, followed by p-doped GaN. The inclusion of a series of InGaN/GaN multiple quantum wells (MQWs) within the nanopillar transforms the elastic structure into an active light emitter. The multi-quantum wells alloy was selected to emit green (540 nm) light. Under an optical or electrical excitation, electrons and holes are generated in the MQWs and are moved toward the center of the nanopillar along the radial direction due to a confinement potential induced by the nonuniform strain relaxation in the MQWs [73]. The nanopillar structure allows the rigid GaN to become flexible subject to an external shear force.

The tactile sensing nanopillars have an elliptical cross-section with dimensions 360 × 120 nm. The nanopillars have a height of 650 nm, which allows for 100 nm of n-GaN and p-GaN around the 450 nm multi-quantum well active region. The 100 nm thickness of p- and n-GaN was chosen to allow for electrical contacts to be fabricated. The nanopillars are organized into rectangular arrays with dimensions 100 × 150 μm with 100 rows and 125 columns. The nanopillars are all aligned with the long axes of the elliptical cross-section parallel to the long (150 μm) axis of the array and they are evenly spaced. Two arrays of nanopillars form a sensing node. In each sensing node, the arrays are aligned orthogonally. The orthogonal orientation allows for the deconstruction of arbitrary force vectors into orthogonal components. The whole sensor consists of an 8×8 matrix of sensor nodes with 1 mm spacing between sensing nodes. The 8×8 matrix allows for the mapping of forces across the tactile sensor. Demonstration and further explanation of this tactile sensor is reported in [71], [72], [75], [76]. The nanopillars were fabricated using standard semiconductor processing techniques. We first defined the nanopillars with electron beam lithography, then we used dry reactive ion etching (RIE) to remove the material between nanopillars. We ensure the nanopillars have vertical sidewalls by following the dry RIE with a wet potassium hydroxide (KOH) etch at room temperature. The KOH attacks the exposed nitrogen faces of the GaN structure, thus creating an anisotropic etch along the c-axis (vertical axis) of the nanopillar. At this point an optically biased MichTac has been fabricated.

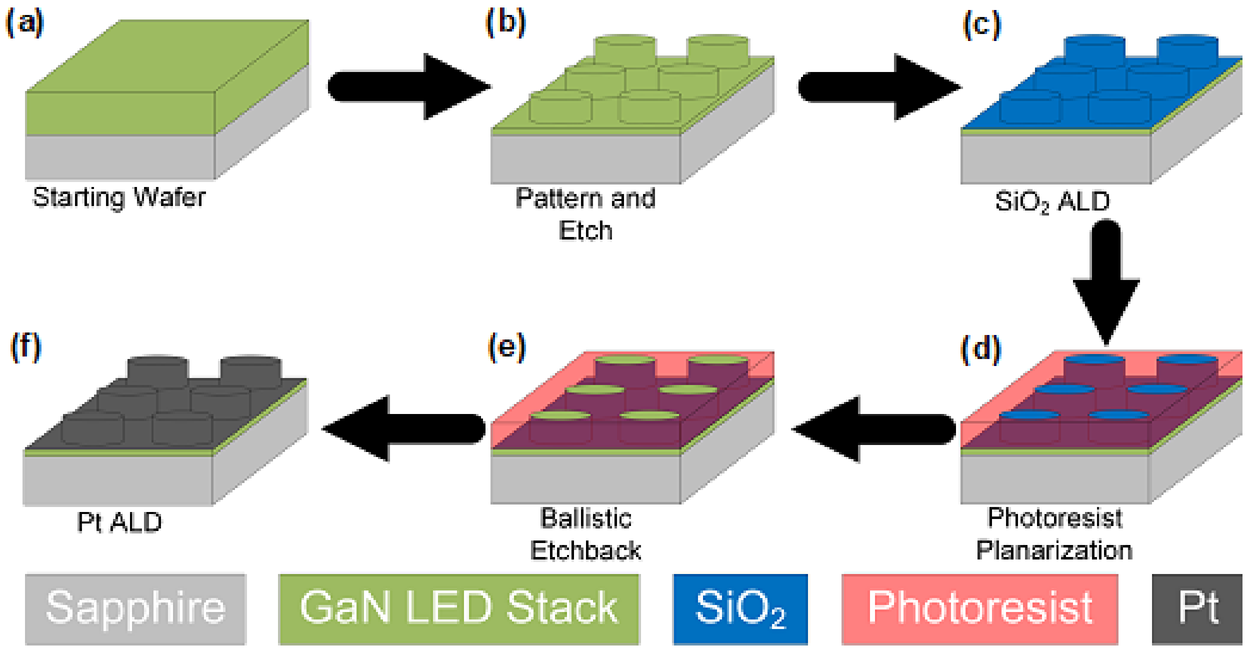

Figure 2-5: The schematic of the process flow for an electrically driven shear stress tactile sensor. (a) The starting wafer consists of an epitaxial stack (green) for a GaN LED grown on either a sapphire, SiC, or silicon substrate (grey). (b) The formation of an array of nanopillar structures which become flexible under an applied shear force. The InGaN MQW layers inside each nanopillar emit light. The emission intensity changes when the nanopillar is deformed. (c) The deposition of an insulating dielectric conformally coated around the nanopillars using ALD. (d-e) The planarization and etch back to expose the tip of the nanopillars for subsequent metallization. (f) The deposition of an ultrathin Ohmic contact for p-GaN using ALD. Adapted from [82].

To add electrical contacts, we conformally coat the entire sensor in 10 nm of silicon dioxide (SiO_2) which has been deposited by atomic layer deposition (ALD). The SiO_2 deposition is essential for creating electrical isolation between the p and n regions of the nanopillars. We then conduct a ballistic etch back with argon plasma to expose the tips of the nanopillars. The exposed tip becomes the p contact after a 10 nm conformal deposition of platinum (Pt) via ALD. An ultrathin conformal coating is essential for maintaining the tactile sensing capabilities of the nanopillars. Exact analysis of the contact design and fabrication is reported in [83]. We avoided thermal annealing of the Pt contact in the current device to prevent the formation of PtSi. Figure 2-6A depicts a cross-sectional view of a single nanopillar on the electrically biased MichTac and Figure 2-6B is an image of a single sensing array on the MichTac.

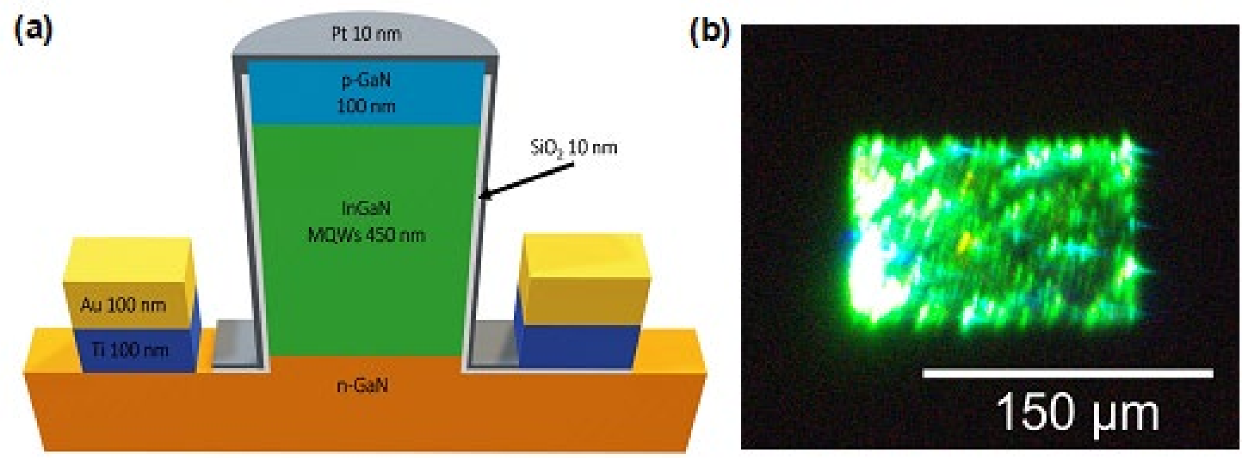

Figure 2-6: (A) The cross-sectional schematic of a nanopillar in the proposed tactile sensor. The epitaxial stack consists of a 100 nm p-GaN region, a 450 nm InGaN region MQW region, and an n-GaN region. The Ti/Au stack (100/100 nm) was used both as the Ohmic contact for n-GaN and as the electrical interconnect. (B) The optical microscope image of the tactile sensor comprising of 100 x 125 nanopillars. The image was taken when the sensor was biased at 6.9 V and 0.43 A with a 10% duty cycle at 100 Hz. The electroluminescence's peak wavelength is 540 nm. Adapted from [82].

Chapter 3 Tactile Sensor Design Toolkit

Designing a tactile sensor which will adequately perform for a given application requires careful selection of the nanopillar height, width, array density, and active area alloy composition. We developed a tactile sensor design toolkit. This toolkit uses commercially available software (nextnano and Comsol Multiphysics) to custom tailor the geometry of the nanopillar tactile sensors for design. For example, the diameter and height of the nanopillars impacts the sensitivity and dynamic range of the nanopillar. Figure 3-1 demonstrates the workflow for the simulation of a singular MichTac nanopillar LED under an applied shear force. This chapter aims to explain the simulation process which informs the design of MichTac.

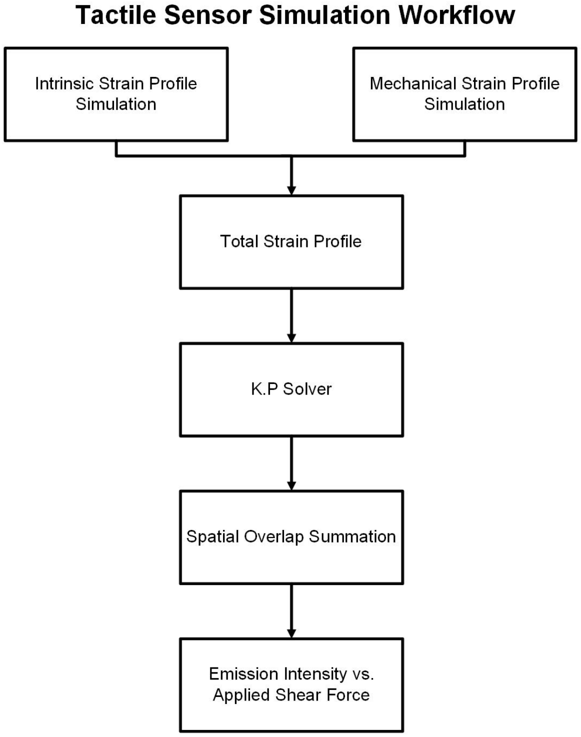

Figure 3-1: Visualization of the simulation workflow for a single nanopillar. Intrinsic strain profile refers to the strain profile generated by the lattice mismatch in the heterostructure. Mechanical strain profile refers to the strain profile generated by applying a shear force to the top of the nanopillars. Adapted from [72].

3.1.1 General Simulation Process Flow

The first step in designing a MichTac sensor is to consider the desired application. When a desired application is picked the dynamic range of the individual sensing elements becomes apparent. Figure 3-2 demonstrates the spectrum of applications and their desired dynamic ranges. MichTac is designed with the end application in mind.

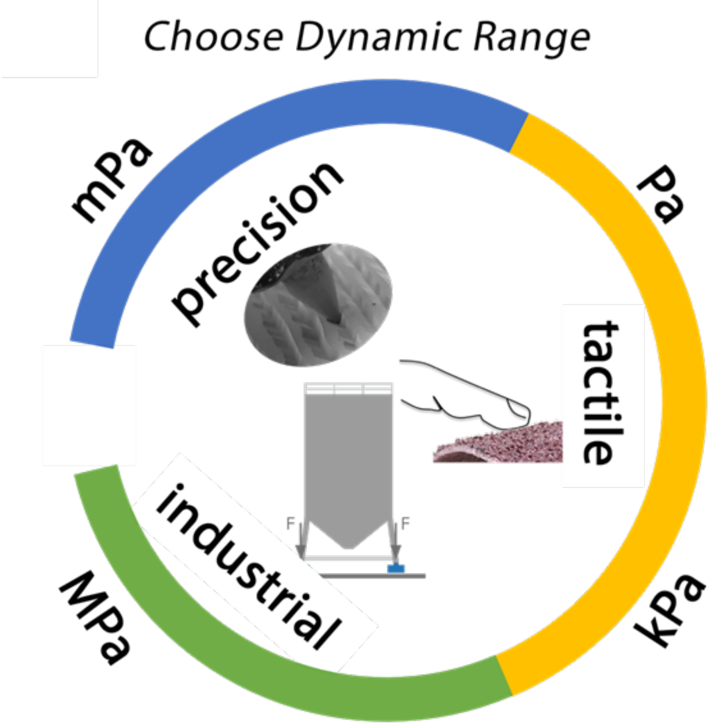

Figure 3-2: Demonstration of dynamic range for specific application environments.

The geometry, number of nanopillars, and density of nanopillars all contribute to the dynamic range of MichTac. For example, a gripper on a surgical robot needs to apply a few newtons of force with great precision as opposed to an industrial load cell which measures if a hopper containing a couple metric tons of material is full or not.

We designed a simulation environment which accurately describes a nanopillar tactile sensor under operation. We consider four aspects. First, the strain profile is generated on a nanopillar when a load is applied to the tip. Second, the intrinsic strains generated within the nanopillar due to lattice mismatch. Third, the band structure of the quantum well region of the nanopillar and the shape of the electron-hole wavefunctions created by the band structure. Finally, the relationships between the electron-hole wavefunction spatial overlap and the light emission of the nanopillar.

3.1.2 Mechanical Strain Profile Simulation

We begin by making assumptions to simplify our model. Our nanopillar is constructed from an isotropic linear elastic material. This means that our nanopillar exhibits the same mechanical properties in all directions and the nanopillar is never yielding. Therefore, our nanopillar stress and strains can be described by

$$\sigma = D\varepsilon \tag{3-1}$$

with

$$D = \frac{E}{(1+v)(1-2v)}\begin{bmatrix} 1-v & v & v & 0 & 0 & 0 \\ v & 1-v & v & 0 & 0 & 0 \\ v & v & 1-v & 0 & 0 & 0 \\ 0 & 0 & 0 & \frac{1-2v}{2} & 0 & 0 \\ 0 & 0 & 0 & 0 & \frac{1-2v}{2} & 0 \\ 0 & 0 & 0 & 0 & 0 & \frac{1-2v}{2} \end{bmatrix} \tag{3-2}$$

where σ refers to the stress, ϵ is the strain, E is the Young's, modulus, and v is Poisson's ratio. E and v can be found in the literature.

We use COMSOL's solid mechanics physics package for our simulation environment. For Mic we use a GaN/$In_{0.18}GaN_{0.82}$/GaN stack along the z-axis of the simulation system. The $In_{0.18}GaN_{0.82}$ region is 3 nm thick and centered at the center of the nanopillar along the z-axis. The listed structure was chosen to reflect a nanopillar LED with a peak emission of ~540 nm. The base of the nanopillar is fixed and non-slipping, and the force is applied parallel to the top face of the nanopillar with no normal force. COMSOL uses a finite element method to solve strains at discrete locations to generate a strain profile which is extracted and saved for later.

3.1.3 Intrinsic Strain

A commercial solid state device simulating package, nextnano, was used to simulate the strain profile due to lattice mismatch between $In_{0.18}GaN_{0.82}$ and GaN. We define our material system as wurtzite GaN with the c-axis of the GaN parallel to the z-axis of the simulation coordinate system. A GaN/$In_{0.18}GaN_{0.82}$/GaN stack was simulated with a 3 nm thick $In_{0.18}GaN_{0.82}$ single quantum well region and 10 nm of GaN on each side of the quantum well region. 10 nm was chosen to reduce simulation time and still capture the strain profile outside of the quantum well. The strain profile was calculated using elastic energy minimization

$$U[u(x)] = \int_{x_0}^{x_1} F(x,u,u')dx. \tag{3-3}$$

The resulting intrinsic strain profile was extracted and combined with the mechanical strain profile to generate a superposition of the mechanical and intrinsic strain to generate a new strain profile, which we will call the sensing strain profile, for quantum mechanical simulations.

3.1.4 Quantum Mechanical Wavefunction Simulations

The sensing strain profile is then fed back into nextnano to calculate the band structure of the active region, then determine the eigen values of the electrons and holes and the solve for the corresponding wavefunctions. We assume there is no interaction between the conduction and valence bands due to the large band gap of GaN (3.4eV). The assumption of no interaction allows us to calculate the eigen energies and wavefunctions using Luttinger-Kohn 6x6 k.p method for degenerate bands. We solve the time-independent solutions,

$$H^{LK}\Psi(\vec{r}) = E\Psi(\vec{r}) \tag{3-4}$$

with

$$H^{LK} = -\begin{bmatrix} P+Q & S & R & 0 & -\frac{S}{\sqrt{2}} & \sqrt{2}R \\ -S^{+} & P-Q & 0 & R & -\sqrt{2}Q & \sqrt{\frac{3}{2}}S \\ R^{+} & 0 & P-Q & S & \sqrt{\frac{3}{2}}S^{+} & \sqrt{2}Q \\ 0 & R^{+} & S^{+} & P+Q & -\sqrt{2}R^{+} & 0-\frac{S}{\sqrt{2}} \\ -\frac{S^{+}}{\sqrt{2}} & -\sqrt{2}Q^{+} & \sqrt{\frac{3}{2}}S & -\sqrt{2}R & P+\mathit{\Delta} & 0 \\ \sqrt{2}R^{+} & \sqrt{\frac{3}{2}}S^{+} & \sqrt{2}Q^{+} & -\frac{S}{\sqrt{2}} & 0 & P+\mathit{\Delta} \end{bmatrix} \tag{3-5}$$

where "+" superscript means Hermitian conjugate. P, Q, R, and S are defined as

$$P = \frac{\hbar^2\gamma_1}{2m_0}\left(k_x^2 + k_y^2 + k_z^2\right) \tag{3-6}$$

$$Q = \frac{\hbar^2\gamma_2}{2m_0}\left(k_x^2 + k_y^2 - 2k_z^2\right) \tag{3-7}$$

$$R = \frac{\hbar^2}{2m_0}\left[-\sqrt{3}\gamma_2\left(k_x^2 - k_y^2\right) + i2\sqrt{3}\gamma_3 k_x k_y\right] \tag{3-8}$$

$$S = \frac{\hbar^2\gamma_3}{m_0}\sqrt{3}\left(k_x - ik_y\right)k_z \tag{3-9}$$

where Δ, γ_1, γ_2, and γ_3 can be found in the literature.

To include the strain in our model, the Pikus-Bir substitutions are made such that

$$k_\alpha k_\beta = \varepsilon_{\alpha\beta} \tag{3-10}$$

$$\frac{\hbar^2}{2m_e^*} = a_c \tag{3-11}$$

$$\frac{\hbar^2\gamma 1}{2m_0} = -a_v \tag{3-12}$$

$$\frac{\hbar^2\gamma 2}{2m_0} = -\frac{b}{2} \tag{3-13}$$

$$\frac{\hbar^2\gamma 3}{m_0} = -\frac{\mathrm{d}}{\sqrt{3}} \tag{3-14}$$

where a_c, a_v, b, and d can be found in the literature, and the conduction band shape due to strain is calculated using the following relation

$$E(k) = E_c(0) + \frac{\hbar^2}{2m_e^*}\left(k_x^2 + k_y^2 + k_z^2\right) + a_c\left(\varepsilon_{xx} + \varepsilon_{yy} + \varepsilon_{zz}\right) \tag{3-15}$$

$$\varepsilon_{xx} = \varepsilon_{yy} = \frac{a_0 - a}{a} \tag{3-16}$$

$$\varepsilon_{zz} = -\frac{2C_{13}}{C_{33}}\varepsilon_{xx} \tag{3-17}$$

where Ɛ refers the the specific strain tensor from the strain profile and a_0, a, C_{13}, and C_{33} can be found in the literature. The overlapping integrals ($|\langle\psi_m|\psi_n\rangle|^2$) of all transition states are extracted for calculation of the light emission with m being the hole eigenstates and n being the electron eigenstates.

3.1.5 Light Emission Calculation

The emitted light from the nanopillar is calculated by assuming the concentration of electrons and holes to both be 10^{18}. Emission intensity light from a LED is determined by Fermi's Golden Rule.

$$\Gamma_{i\rightarrow f} = \frac{2\pi}{\hbar}|\langle f|H'|i\rangle|^2\rho\left(E_f\right) \tag{3-18}$$

We use a modified version of (3-18) to determine the intensity of the light emission (I).

$$I = \sum_{m=1}^{m'}\sum_{n=1}^{n'} f_n(E_n)f_p(E_m)|\langle\Psi_m|\Psi_n\rangle|^2 \tag{3-19}$$

$$f_n(E_n) = \frac{1}{1 + e^{\frac{E_n - F_n}{k_b T}}} \tag{3-20}$$

$$f_p(E_p) = \frac{1}{1 + e^{\frac{F_p - E_p}{k_b T}}} \tag{3-21}$$

$$n = \sum_{n=1}^{n'} \frac{m_e^* k_b T}{\pi \hbar^2 L_z} \ln\left(1 + e^{\frac{F_n - E_n}{k_b T}}\right) \tag{3-22}$$

$$p = \sum_{m=1}^{m'} \frac{m_h^* k_b T}{\pi \hbar^2 L_z} \ln\left(1 + e^{\frac{E_p - F_p}{k_b T}}\right) \tag{3-23}$$

where F_n represents the quasi-fermi level of the electrons, F_p the quasi-fermi level of the holes, E_n the eigen energy of the electrons, E_p the eigen energy of the holes, m_e^* the effective mass of the electron, and m_h^* the effective mass of the holes. We set L_z, the effective width of the quantum well, to be 3 nm and T, the temperature, to be 300K.

The emission intensity (I) of a load is calculated and divided by the intensity of the unsheared system (I_0) to determine the decrease in emission intensity, or relative intensity (R).

$$R = \frac{I}{I_0} \tag{3-24}$$

Therefore, since relative intensity is determined by the overlap integral, and overlap integral is determined by the force (F_s), we now have the relationship

$$F_s = R. \tag{3-25}$$

With the relationship

$$\mathrm{F_s} = \mathrm{R}. \tag{3-25}$$

we can infer the applied force on the MichTac sensor by monitoring the emission intensity of the nanopillar LEDs. Figure 3-3 depictes the movement of the electorn and hole wavefunctions under applies shear force.

3.2 Measuring Applied Force

To determine the force applied to MichTac, we combined experimental observations with simulation of electro-mechanical behavior of a single nanopillar. Figure 3-1 summarizes the simulation methodology. First, we calculated the strain profile in the nanopillar using the COMSOL Multiphysics simulator. We used an isotropic linear elastic model system for the nanopillar. We constrained the bottom face of the pillar with a no-slip condition and applied a shear pressure at the to the top face of the nanopillar. We then calculated the residual strain in the InGaN nanodisk region without the shear pressure using a commercial solid state device simulator, nextnano. The residual strain originates from the lattice mismatch between InGaN and GaN. The strain profile is nonuniform along the radial direction due to strain relaxation near the circumference of the nanopillar. The residual strain was added to the mechanical strain due to the external pressure, which was then fed into nextnano again to calculate the electronic band structure in the InGaN region using the k-dot-p method.

We used the six-band Pikus-Bir Hamiltonian for wurtzite semiconductors for the hole states and the effective mass theory for the electron states. Multiple eigenstates were calculated for both the electrons and holes. Figure 3-3 shows examples of the lowest electron and hole wavefunctions under different external shear forces. The spatial overlap integral between the electron and hole states was weighted by the Fermi-Dirac statistics. This Fermi's golden rule was then used to determine the emission intensity for each electron-hole transition. The emission intensity was determined by summing over all the transitions. The emission wavelength was determined by fitting the intensity versus wavelength plot with a single gaussian function.

We obtained the dynamic range of the sensor by plotting the emission intensity versus the external force which is equal to the pressure multiplied by the top surface area of the nanopillar and then multiplied by the total number of nanopillars in contact with the stress applicator. The relationship was found to be linear except when the relative intensity has become incredibly low. The linear region corresponds to 0-200 kPa.

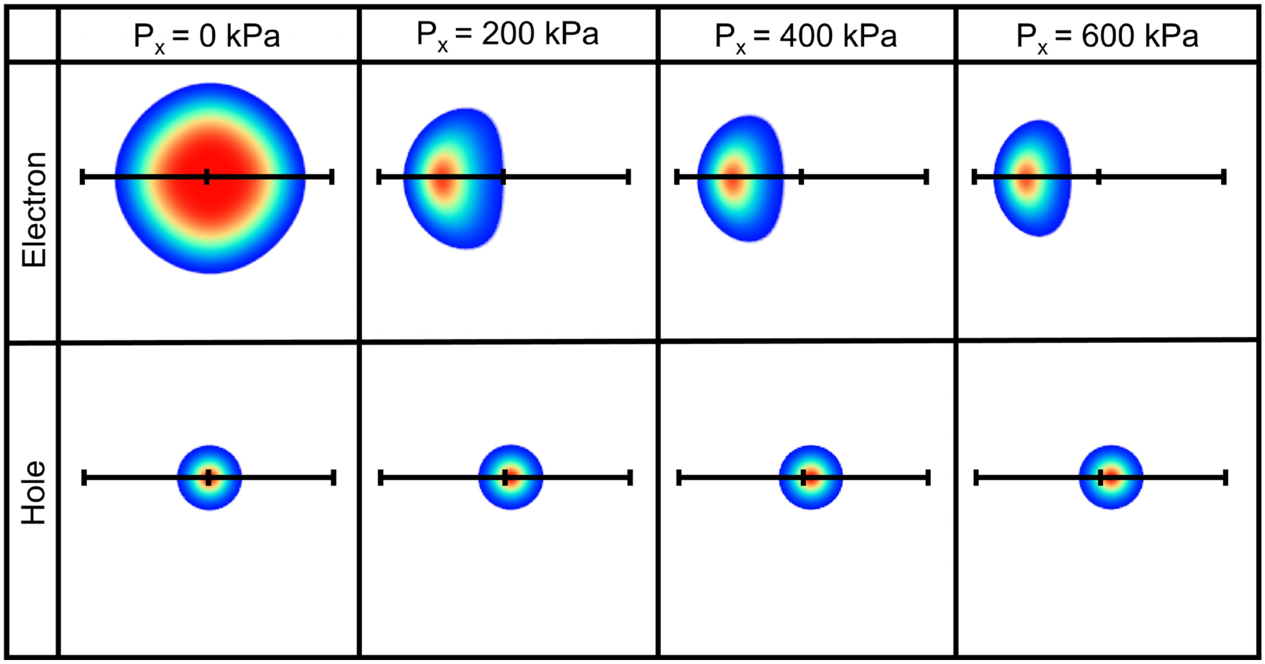

Figure 3-3: Examples of wavefunctions corresponding to the lowest electron and hole states under different external shear forces applied to the top surface of the nanopillar. The force's direction is from left to right in the above figure. The axis represents the long axis of the elliptical cross section. The left, center, and right tick marks represent the left edge, center, and right edge of the nanopillar. The electron (hole) wave functions shown here are contour plots sliced at the top (bottom) of the InGaN nanodisk. The misalignment of the electron and hole wavefunctions under an external force leads to the reduction of emission intensity. Adapted from [72].

3.3 Simulation of Nanopillar Cladding

Numerical simulations were performed to verify the functional feasibility of the GaN/SiO_2/Pt structure. The change of light emission intensity in responding to an external shear force was simulated. We first calculated the strain distributions due to the external force and the lattice mismatch between InGaN and GaN using Comsol and nextnano, respectively. In Comsol, the nanopillar's bottom face was confined to a no-slip condition and its body was modeled as an isotropic linear elastic system. The mechanical force was applied using a non-slipping shear pressure with no pressure applied normal to the nanopillar. In nextnano, we used the continuum elasticity approximation to allow the sidewall of the nanopillar to freely relax. A 3 nm thick InGaN quantum well was placed at the center of the nanopillar.

The two strain profiles calculated from Comsol and nextnano were added together to calculate the electron and hole wavefunctions. The calculation employed a six-band Luttinger-Kohn Hamiltonian and included the strain using the Pikus-Bir method. 32 conduction- and 32 valence-band eigenstates were calculated. The wavefunctions were then plugged into Fermi's golden rule to determine the emission intensity. The quasi-Fermi levels were based on $10^{18}/cm^3$ electron and hole concentrations in the MQWs. Two nanopillar structures were compared: a bare GaN nanopillar with an elliptical cross-section of 360 nm x 120 nm and a height of 650 nm; a GaN nanopillar of the same dimensions conformally coated SiO_2 and Pt layers, each with a 10 nm thickness. The top of the SiO_2 layer was removed such that the Pt can contact the GaN. We did not consider the surface states at the perimeter of the nanopillar. In the range of interests for tactile sensing, on the order of 0 - 200 kPa, the electrons and holes are still confined toward the center of the nanopillar.

Figure 3-4 shows the simulation result. Both bare and coated GaN nanopillars show a similar trend in responding to the external force. Both respond more strongly to a force parallel to the elliptical cross section's long axis. The coated nanopillar is stiffer, evidenced by the reduced sensitivity to the external force.

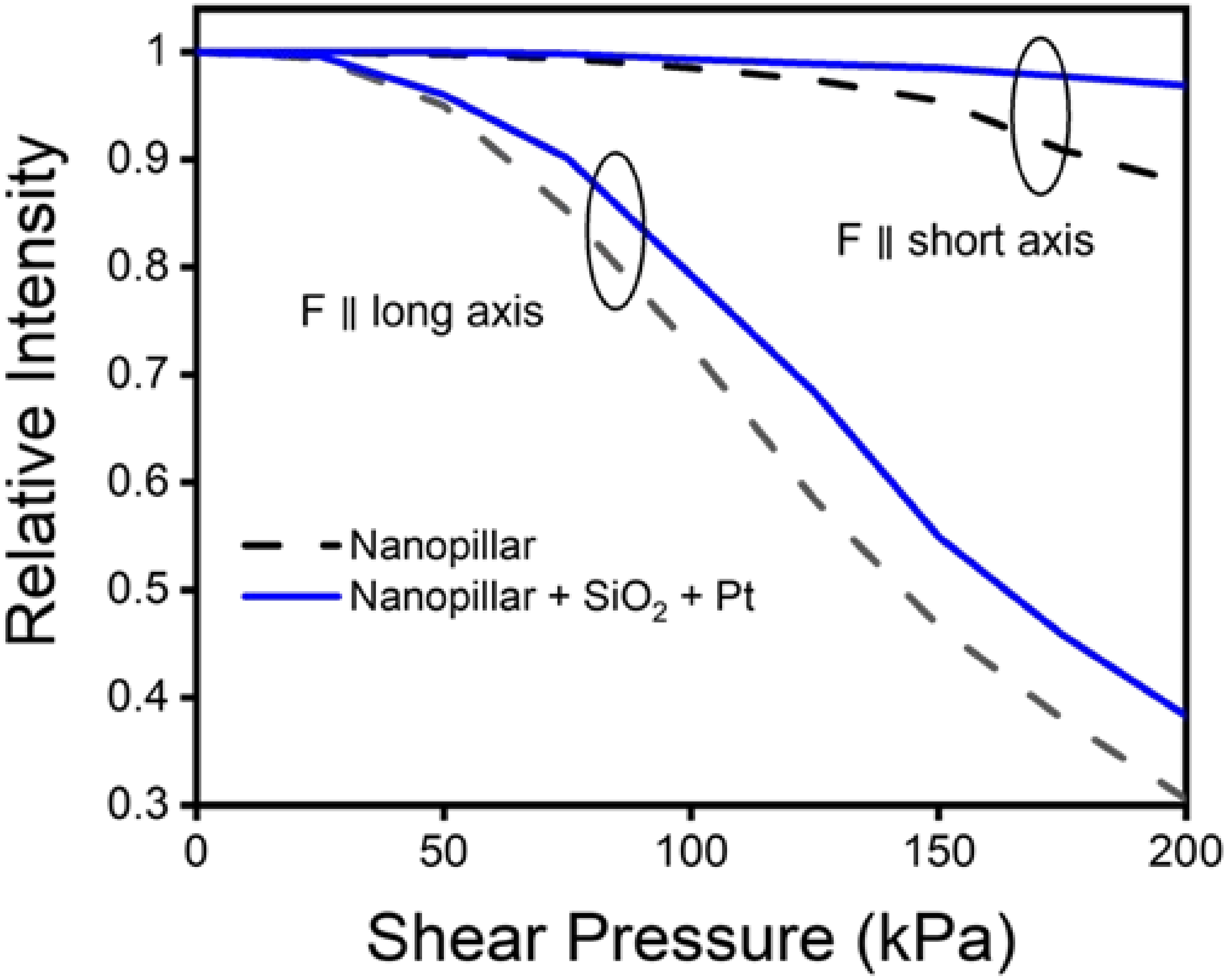

Figure 3-4: The intensity emitted from the nanopillar deformed by an external shear pressure normalized to the intensity at a zero stress. The nanopillar has an elliptical cross section of 360 nm x 120 nm and a height of 650 nm. Two variations are considered: a bare GaN nanopillar (dashed lines) and a GaN nanopillar coated with SiO_2 (10 nm) and Pt (10 nm). The SiO_2 only covers the sidewall while Pt encapsulates the entire structure. Two different force directions are considered: parallel to the elliptical cross section's long and short axes. Adapted from [82].

3.4 Contact Patch Simulations

Due to the compliant nature of the testing surfaces, it is possible the testing surface was pushed into the nanopillars. Moreover, the tactile sensor used in the experiment did not have nanopillars covering the entire sample area. Part of the testing surface may contact the sample area without nanopillars, even if the sample area is 650 nm below the tip of the nanopillars. To better understand the interaction between the testing surfaces and the tactile sensor, we performed numerical simulations using COMSOL's Solid Mechanics module to simulate the deformation of the testing surfaces when in contact with the tactile sensor. In the simulation, as shown in Figure 3-5, we created a 2 μm thick testing surface on a 2 μm thick sapphire substrate. The tactile sensor was modeled as two nanopillars with a height of 650 nm made of GaN on a 2 μm thick GaN substrate. Initially, the tip of the nanopillar was placed 200 nm away from the top of the testing surface. The top boundary of the GaN was constrained and not allowed to move. The bottom boundary of the testing surface underwent a prescribed displacement until the air gap was zero between the testing surface and the GaN substrate. The minimum normal force required to make contact was 0.212 and 0.140 N for the photoresist and silicone rubber, respectively. These forces are considerably smaller than the normal force applied by the testing surfaces in the experiment, suggesting that portions of both testing surfaces were in direct contact with the GaN surface of the tactile sensor, as shown in Figure 3-5.

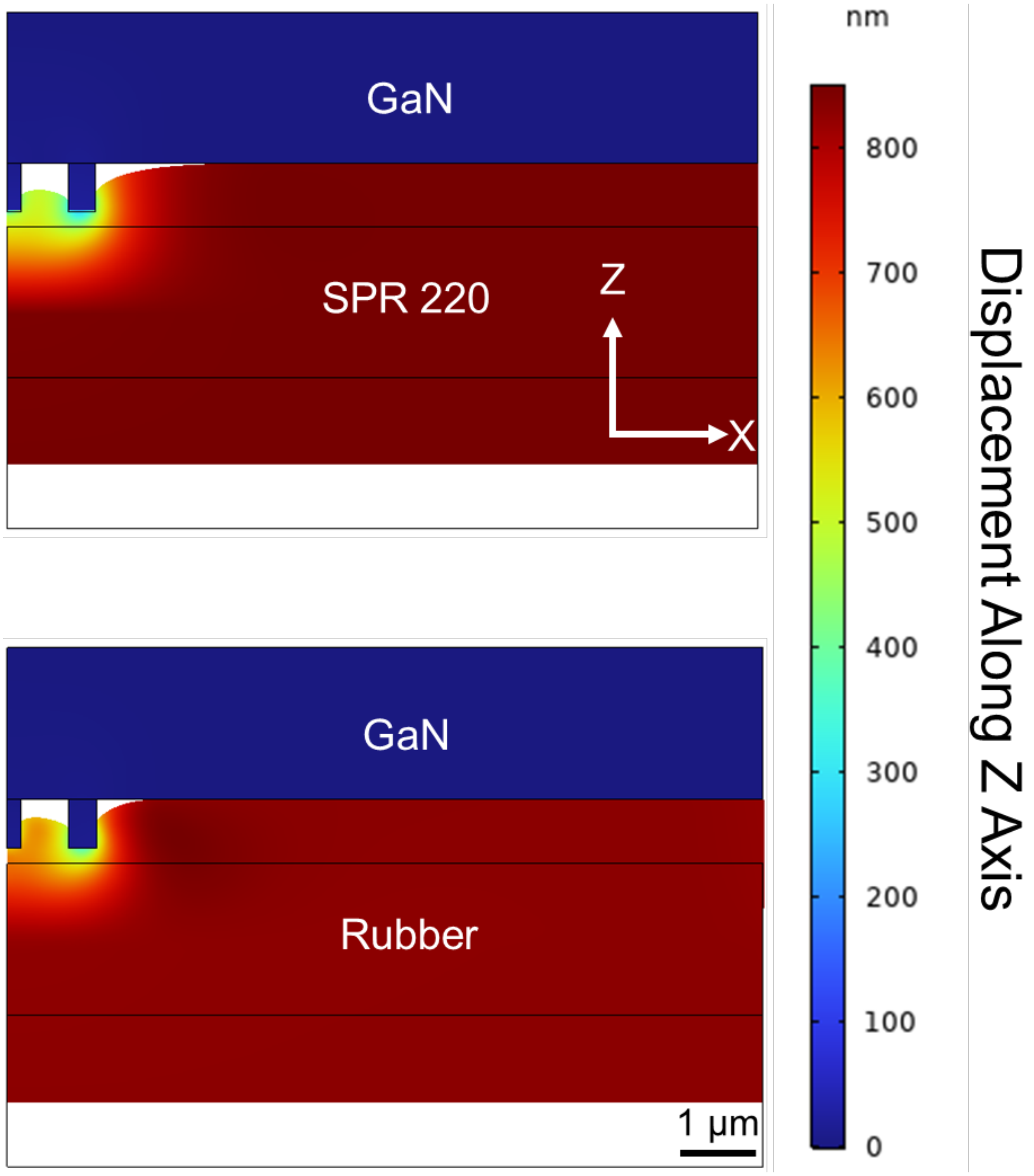

Figure 3-5: Simulation of testing surface's compliance when in contact with the tactile sensor, which is shown upside down and modeled by two nanopillars on the left and a GaN substrate on the right. Only a normal force was applied. The coloring of the simulation corresponds to the vertical displacement of the simulation mesh. The maximum displacement was 850 nm, and the test surface started 200 nm away from the nanopillar's tip. The top and bottom show the contact conditions of the SPR 220 photoresist and the silicone rubber, respectively. Adapted from [78].

Chapter 4 Verification of Tactile Sensing

In this chapter, validation of the MichTac configurations is performed [84]. We assess MichTac's ability to map a force field including both the force's magnitude and direction for both the optical and electrically biased configuration. We also confirm the simulated force results with a force/torque gauge. We found MichTac's spatial resolution is found to be limited only by the density of the nanopillars (1µm) or/and the image sensor's pixel size (3.72 µm). The sensor exhibited a dynamic range of 1 – 30 mN and an accuracy of ±1.3 mN. Finally, a successful demonstration of tactile sensing is demonstrated by gently gliding a human fingertip gently across MichTac.

4.1 Benchtop Tactile Sensing

A digital single-lens reflex (DSLR) camera with a pixel size of ~5 µm was used to record light emission from the sensor array. The experimental setup is shown in Figure 4-1. To apply the shear force, a stress applicator was fabricated by patterning a square of photoresist (SPR220, 2.2 µm) on a sapphire wafer using optical lithography. The photoresist wan then exposed again to ultraviolet light to render it transparent to visible wavelengths [71].

4.2 Methods

To create sufficient clearance for the stress applicator, we opted to use an imaging optics configuration to project the image of the sensor array to the DSLR camera. During measurements, the sample was excited by a 405 nm laser diode at an angle. We used a 425 nm long-pass filter in

Evaluation of MichTac, shown in Figure 4-2
and Figure 4-3, was assisted by Kobie Muller.

front of the camera to block the laser beam. To apply the force on the sensor, we first placed a 45º glass prism on the top of the stress applicator which was mounted on a translation stage. The photoresist pad was facing the sample. We adjusted the laser beam's angle such that total internal reflection (TIR) was observed when there was an air gap between the stress applicator and the sample. We also confirmed the laser beam can excite the entire sample without the prism. We then gradually lowered the stress applicator toward the sample and used a fiber-optic spectrometer placed underneath the sample to detect any tunneling of laser beam through the gap between the applicator and sample. When the spectrometer detected the laser, the air gap was on the order of the wavelength. We switched to monitor the camera while lowering the stress applicator more until we saw a slight drop in emission intensity. We defined this position as Z=0. To apply a shear force, we changed only the X and Y positions of the stress applicator.

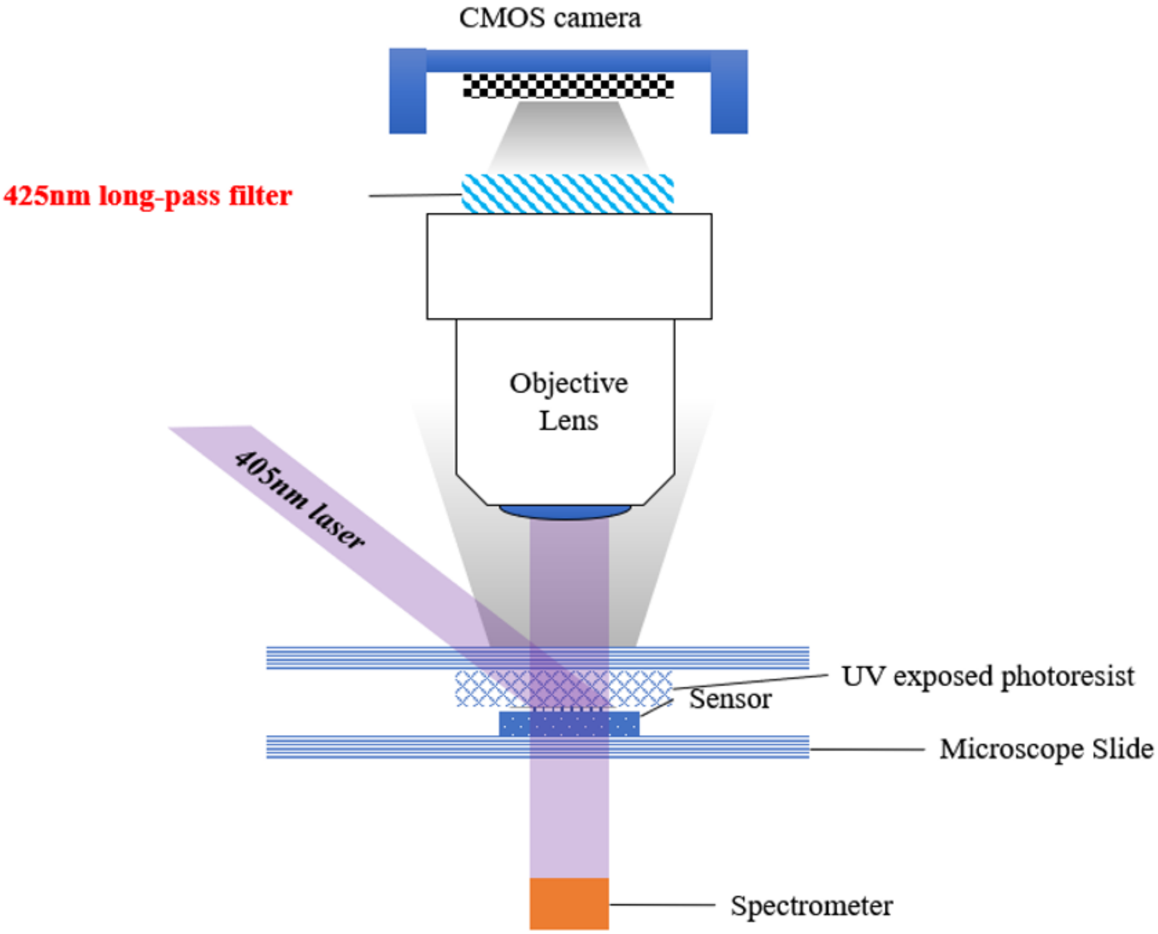

Figure 4-1: The schematic of the measurement setup. The tactile sensor was powered by a 405 nm diode laser. The CMOS camera recorded the emission pattern from the sensor array. Although not necessary for the sensor's functionality, an objective lens was used due to the distance between the sensor and the DSLR camera needed to accommodate the stress applicator used in the experiment. A fiber-optic spectrometer was placed underneath the sensor to monitor the distance between the stress applicator (UV exposed photoresist) and the sensor. Adapted from [72].

To characterize the tactile sensor, we used a photoresist-based stress applicator. First, we used a 5 mm × 5 mm stress applicator to apply a uniform force across the entire sensor array. The force’s magnitude was controlled by moving the stress applicator parallel to the device’s surface at a 50µm step. We recorded each LED’s emission intensity and compared that to the intensity without any horizontal translation to obtain the relative intensity as shown in Figure 4-2. We found a linear relationship between the relative intensity and the stress applicator’s horizontal movement. We then performed numerical simulations (see Section 3.2) which showed a linear relationship between the relative intensity and the shear force. These results suggested that the stress applicator can indeed controllably apply a shear force on the sensor array, and we can map the applicator's horizontal movement to the force. Figure 4-3 combines the data from the two independent sensor in each sensor node as shown in Figure 4-2. The two sets of lines correspond to the relative intensities measured by the X Sensor (blue lines) for an X-direction force and Y Sensor (red lines) for a Y-direction force, respectively. The blue and red lines' intersections determine a shear force's magnitude and direction. The dynamic range can be extrapolated to be 1 – 30 mN. The force measurement's accuracy is determined to be ±1.3 mN which is the root-mean-square error (RMSE) of the fitting in Figure 4-2.

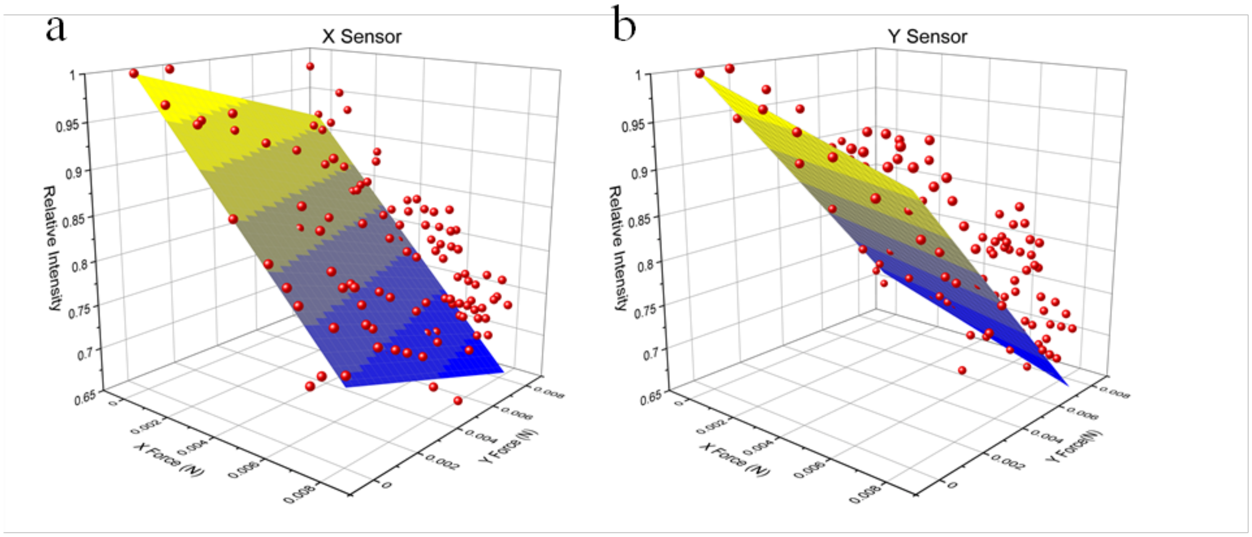

Figure 4-2: The relative intensities recorded at the two nanopillar LED sites in the same sensor node as a function of the X and Y forces. The X and Y sensors are labeled such that the X (Y) axis of the translation stage is parallel to the ellipse's long axis. The data points (dots) are fitted with a plane in each sensor. Adapted from [72].

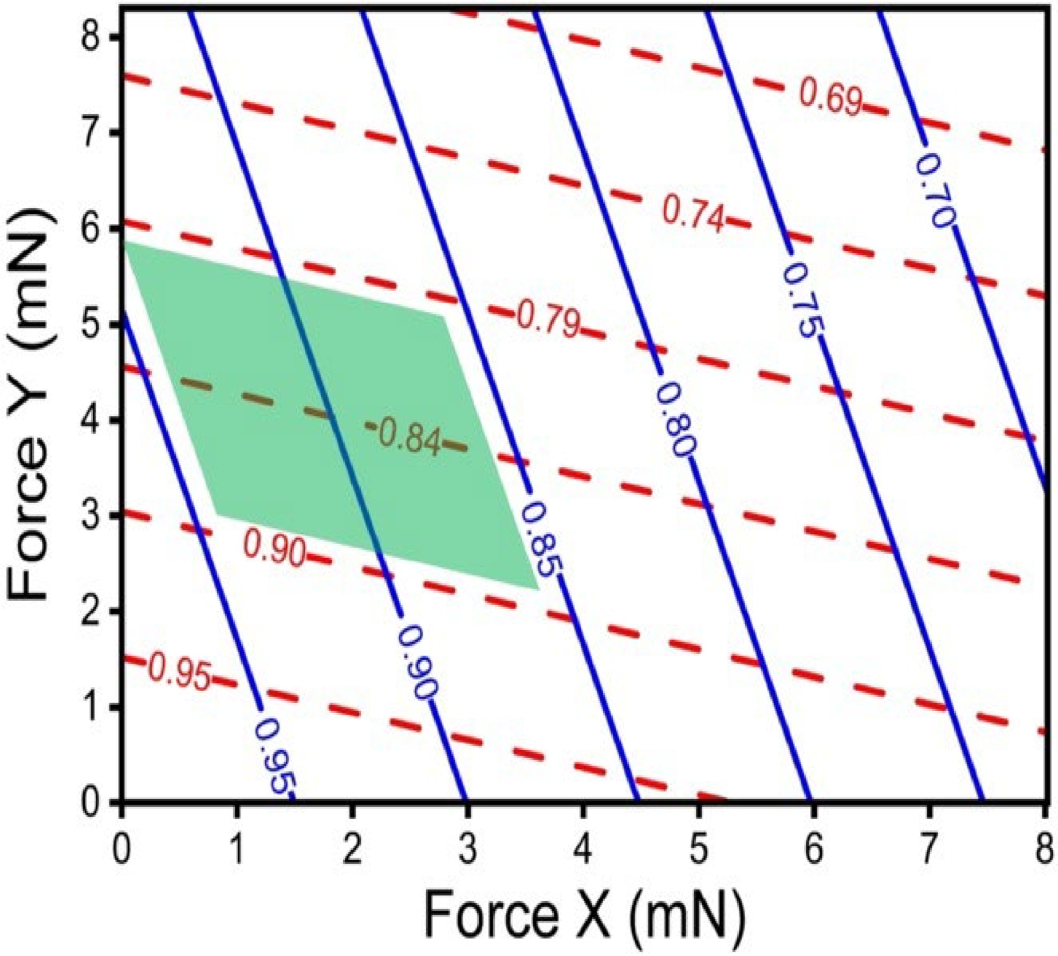

Figure 4-3: The relationship between the two nanopillar LEDs' relative intensities in each sensor node and the shear force's magnitude in the X and Y directions. The blue solid and red dashed lines correspond to the relative intensities measured from the X Sensor and Y Sensor, respectively. The shaded parallelogram corresponds to the RMSE of the fitting in Figure 4-2, ranging between (force – RMSE) and (force + RMSE). Adapted from [72].

4.3 Force Mapping using Time Evolution Analysis

We demonstrate the mapping of a moving shear force we changed to a smaller stress applicator. We chose an applicator with a size (1 mm^2) comparable to each sensor node and moved the applicator across the sensor array along a path shown in Figure 4-4A to test the sensor's ability to record the force's path. We recorded images at nine distinct locations marked by 1−9 in the order of time. The path went through five sensor nodes labeled by A−E. The force's magnitude and direction can be determined using the five sensor nodes measured relative intensities and data in Figure 4-3. The results are plotted in Figure 4-4B and Figure 4-4C for the force's magnitude and direction, respectively. Figure 4-4 shows that we can successfully identify the location and moving direction of the stress applicator. The ambiguity of colinear force directions was manually removed by corroborating with the location data of the force.

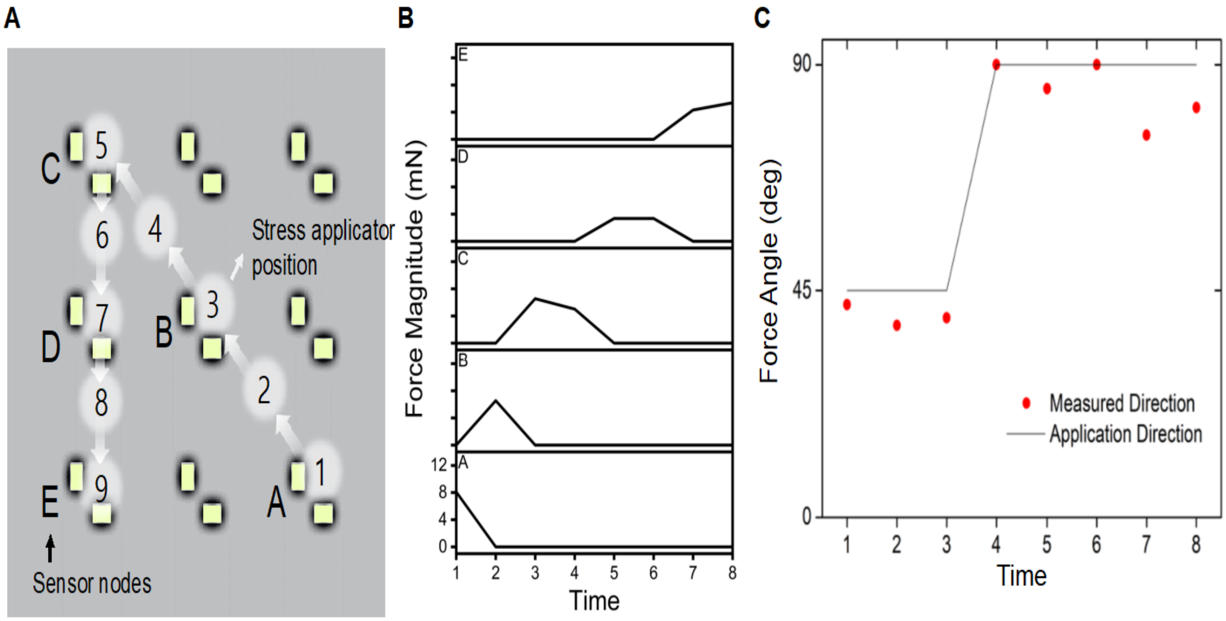

Figure 4-4: Mapping of a dynamic force field generated by a moving stress applicator. (A) The layout of the 3×3 sensor nodes monitored by the image sensor and the stress applicator's path. The size of the stress applicator is comparable to that of each sensor node. The path went through five sensor nodes labeled by letters A–E. A total of nine intensity maps were taken by the CMOS camera when the stress applicator was at locations marked by 1–9 in the order of time. (B) The shear force's magnitudes measured by sensor nodes A–E when the stress applicator was at locations 1–9. The x and y axes are identical in all plots. (C) The measured force's direction (dots) when the stress applicator was at locations 1–9. The solid line is for visual guidance only. Adapted from [72].

4.4 Microdetail Detection

To demonstrate our device's applicability for tactile sensing, we removed the stress applicator and flipped the optically biased MichTac upside down. The lead author then moved his index fingertip diagonally across the sensor array at an approximately 45° angle with the gentlest possible while still repeatable touch, 5 - 6 mN as determined using a weight scale. The goal was to simulate the action of feeling a soft surface and its texture, although in this case, the tactile sensor functioned as the fingertip and the fingertip as the surface. Light was collected from the substrate side by the same imaging optics setup shown in Figure 4-1. The CMOS camera was switched to the video mode, and video frame data was post-processed in Matlab to extract the green channel of the sensor array's intensity map as a function of time. Figure 4-5 shows an example of a snapshot. The fingerprint pattern can be seen clearly due to the reflection of LED emission by the fingertip captured by the camera, potentially providing additional information for tactile sensing if we choose to use imaging optics, albeit at the expense of a larger system size.

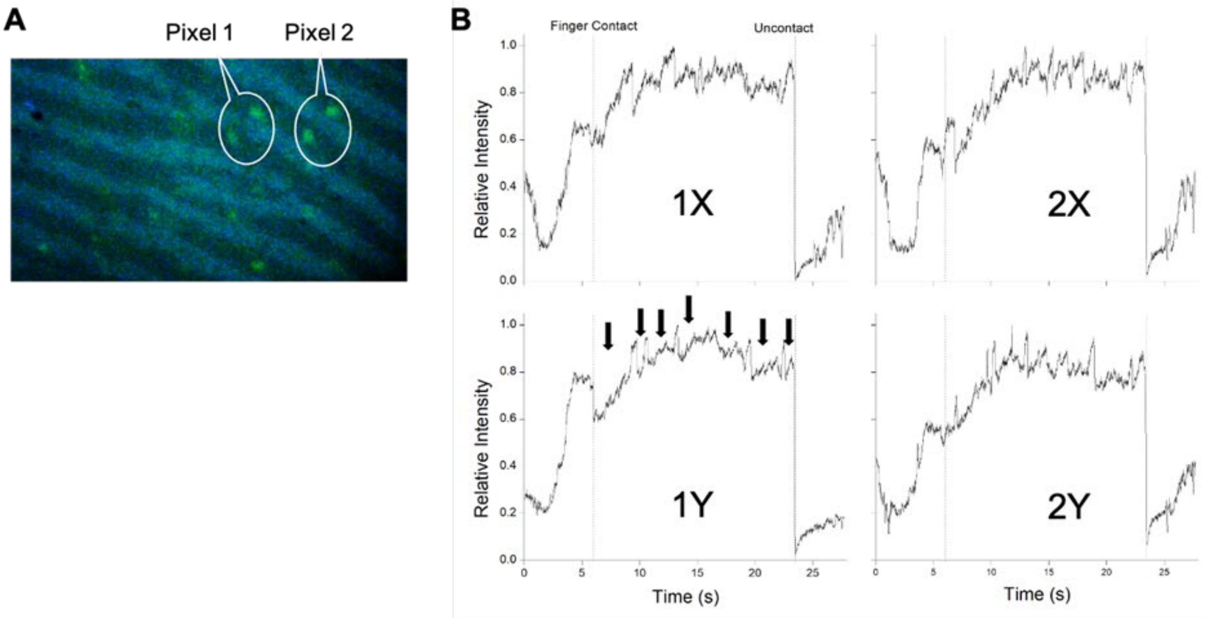

Figure 4-5: The demonstration of the proposed tactile sensor for tactile sensing of a relatively smooth but slightly curved surface, the lead author's fingertip. (A) An image of the fingertip in contact with the sensor captured by the camera. The fingerprint pattern and the emission from multiple sensor nodes can be seen. The two sensor nodes on the upper right corner of the image are labeled as Pixel 1 and Pixel 2 for the discussions. (B) The relative intensities from the four nanopillar LEDs in Pixels 1 and 2 as a function of time. The X and Y sensors in Pixels 1 and 2 are labeled as (1X, 1Y) and (2X, 2Y), respectively. As a reference, the vertical dashed lines indicate when the fingertip contacted and later removed from the sensor array by examining the camera image. Also, the black arrows mark the times when a fingertip's ridge passed the 1Y LED. Adapted from [72].

We will focus on intensity data from two sensor nodes in the following discussions, labeled Pixel 1 and Pixel 2. The relative intensities of each sensor node's X and Y sensors, labeled as 1X, 1Y, 2X, and 2Y, are plotted in Figure 4-6 as a function of time. First, we discuss the data qualitatively. We expect the intensity to decrease when a fingertip's ridge moves into and hence stresses the nanopillars. We also expect an increase of intensity when the valley is on top of the LED. Figure 4-6 plots the relative intensities of the four LEDs and compares the data with the images at four separate times. Ridge (R), valley (V), or partial ridge (PR) are identified by examining the photos and labeled in the intensity plots. A good agreement with the above assertion is observed. For example, the intensity drops in LED 1X between 13s and 13.13s when a ridge moves in. According to Figure 4-3, the amount of force can be determined to be roughly 6 mN which is consistent with the value estimated from a weight scale. The force's direction can also be obtained to be 40.7º and 40.4º from sensor 1's and sensor 2's data, respectively. The results are consistent with the diagonal travel of the fingertip across the sensor array.

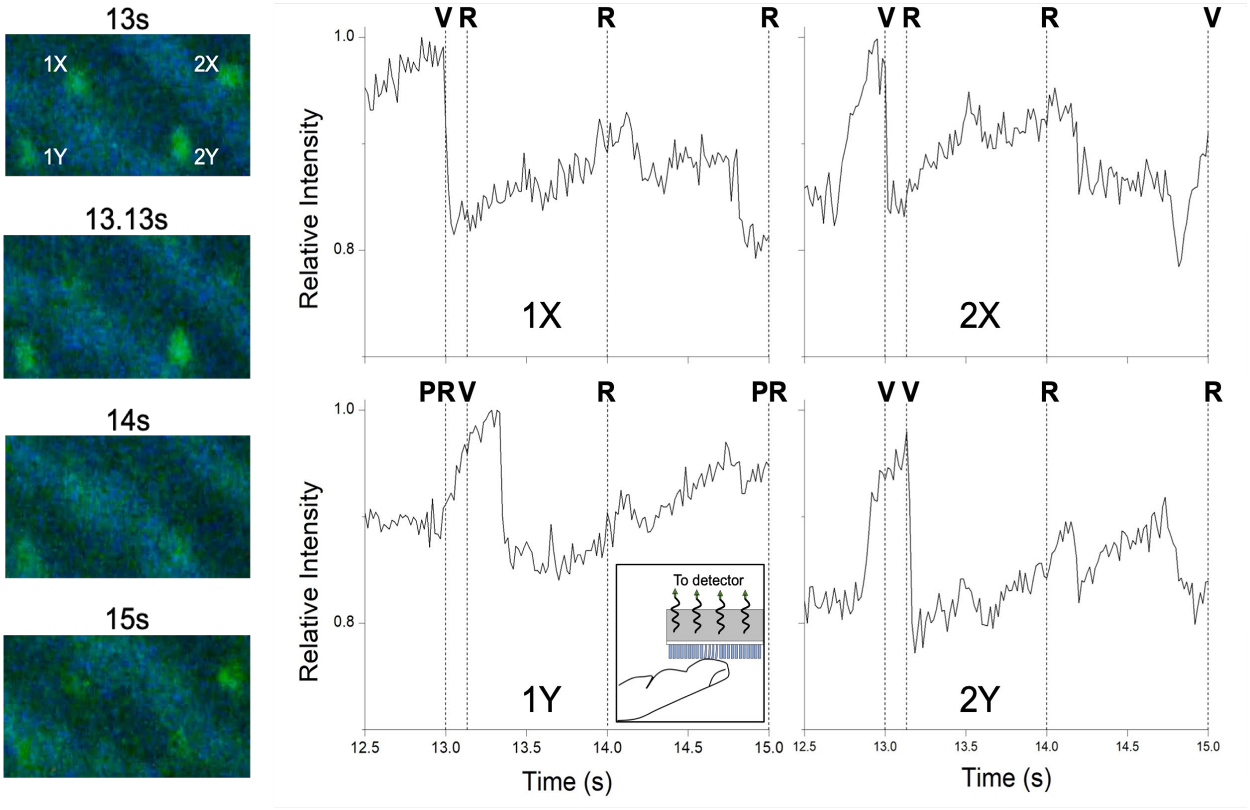

Figure 4-6: Demonstration of the proposed tactile sensor for tactile sensing of a relatively smooth but slightly curved surface using the lead author's fingertip. The sample is flipped, and light is collected from the substrate side as shown in the inset at the bottom. The left panel shows the video snapshots, and the right panel shows the relative intensity data recorded from the four nanopillar LEDs labeled 1X, 1Y, 2X, and 2Y. The fingerprint pattern can be correctly identified by the change of the intensity curve: a decrease means a ridge (R) moves into the sensor node; an increase when a valley (V) passes over; and a gradual increase when a ridge is transitioned to a valley. We also examined the camera images at four different times: 13s, 13.13s, 14s, and 15s and label the scenario for each LED: ridge (R) means a ridge is seen to be on top of the LED, valley (V) means a valley is seen to be on top of the LED, and a partial ridge (PR) means a ridge only covers part of the LED. Adapted from [72].

4.5 Direct Shear Stress Force Validation

This section presents the direct shear force measurement and mapping, including the force's magnitude and direction without any post-data processing required, using GaN nanopillar LED-based tactile sensor. We also show that the sensor can detect the oscillation between the slip and grasp states. Different force applicators are mounted onto a compliant holder to ensure flat contact is made between the tactile sensor and the test surface. The compliant holder is clamped into a 3D printed holder which is bolted to the force/torque sensor. The force/torque sensor is mounted on a 3-axis translation stage (Thor Labs NanoMax).

Previously, we have demonstrated the mapping of a two-dimensional shear force field. The force's absolute magnitude was determined by comparing the measured relative intensity change with numerical simulations. The calculated intensity changes as a function of the force's magnitude generated a lookup table to translate the measured intensity map to the force field [72]. In this section, we designed an experiment to directly measure the absolute magnitude of force applied to the tactile sensor, enabling the "lookup table" to be generated experimentally rather than numerically.

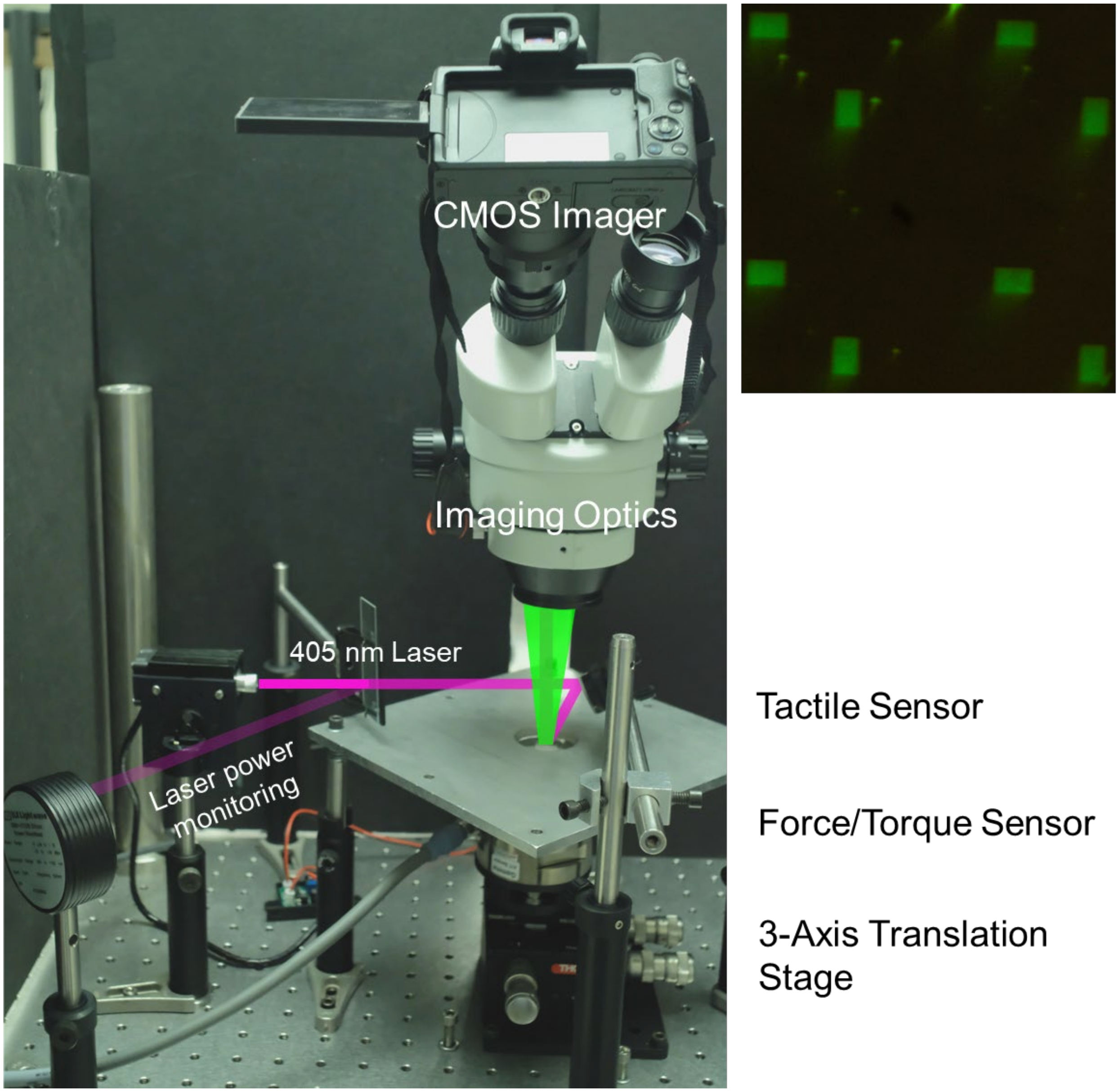

Figure 4-7: Schematic of the experimental setup consisting of a CMOS imager using a commercial DSLR camera and custom image optics, bias laser, optical power meter for monitoring the laser power, tactile sensor, and its holder (the square aluminum plate shown), and a 3-axis translation stage. The optical path of the laser is shown in purple, and the emission of the tactile sensor is shown in green. The 425 nm long pass filter is housed within the imaging optics to remove the optical bias. During the measurements, the tactile sensor remained stationary while the force was applied by moving the testing surface rigidly mounted to the force/torque sensor using the translation stage. An example image collected by the CMOS imager is shown in the upper right. The green rectangles are the nanopillar arrays used for tactile sensing. Adapted from [78].

4.5.1 Methods

The experimental setup is shown in Figure 4-7. We used a commercially available force and torque (F/T) sensor (ATI Gamma), which has an accuracy of 0.01 N. The force and torque sensor acts as the supporting plane for a testing surface which directly contacts MichTac. We chose two testing surfaces, a 500 µm thick rigid sapphire wafer coated with a thin photoresist (SPR 220 3.0, 2.2 µm thickness), and a flexible silicone rubber square. Each of these surfaces was attached rigidly to the sensing surface of the F/T sensor. The nanopillar tactile sensor was mounted with the nanopillars facing downward. It was optically biased [72] with a 405 nm laser for simplicity although an electrically biased version of the sensor was previously demonstrated [76]. The sensor response was recorded using a commercial DSLR camera equipped with a CMOS imager. A 425 nm long-pass optical filter was used to reject the biasing laser. Without the filter, the laser can saturate the imager's detection pixels and lead to an inaccurate intensity measurement.

To apply the force, we kept the tactile sensor stationary while moving the F/T sensor with a three-axis translation stage. Contact between the testing surface and the tactile sensor was determined by monitoring the reported force normal to the sup-porting plane of the F/T sensor. Once the contact was firmly made, the testing surface was moved in the shear direction with respect to the tactile sensor. We moved the translation stage in the X direction with a 50 µm step size up to 500 µm. The X direction was aligned to one of the ellipse's axes. At each displacement step, an image of the tactile sensor was captured with the CMOS imager, the F/T sensor data was collected, and a photodetector recorded the power of the biasing laser. We calculated the average green integer value reported by the CMOS imager for each visible array during each translation step. The green values were normalized against their respective arrays at the 0 µm translation image to determine the relative intensity emission of each nano-pillar array. The intensity change is expected to be more sensitive when the force is parallel to the long axis. Figure 4-8 shows the results. The two testing surfaces' normal forces applied to the tactile sensor are 0.739 and 1.009 N for the photoresist and silicone rubber, respectively. The amount of normal force was chosen by observing the reading of the F/T sensor when a small shear force was simultaneously applied. We increased the normal force until the reading became stable and not noisy, which was an intrinsic limitation of the F/T sensor requiring a small but steady normal force in accurately measuring the shear force.

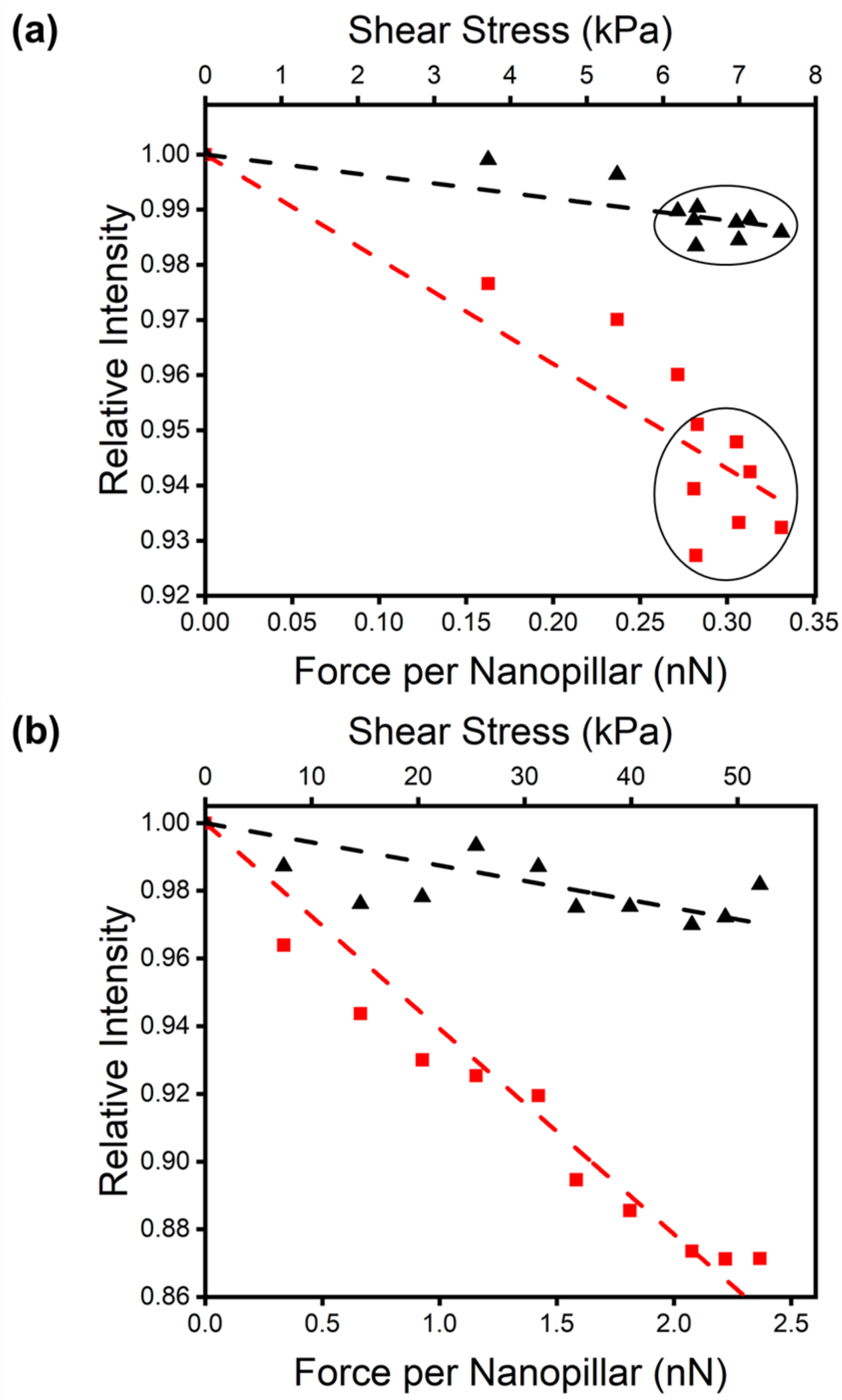

Figure 4-8: The response of the tactile sensor's emission intensity versus a shear force applied to two testing surfaces: (A) SPR 220 photoresist and (B) silicone rubber. The force reading from the F/T sensor is converted to the shear stress (top axis) and force experienced by each nanopillar (bottom axis) based on the contact area of each testing surface with the tactile sensor. In each graph, the two curves were measured from the two nanopillar LEDs with their ellipse cross-section's orientation orthogonal to each other. The black (red) curve corresponds to the LED with the ellipse's short (long) axis parallel to the force. The dashed lines are the linear fits of the measurement data. In (B), the fluctuation of the measured intensity within the two circles suggested a slip between the testing surface and the tactile sensor. Adapted from [78].

We calculated the shear stress applied during the measurements based on the simulation results. The contact areas for the photoresist and rubber are 51.7 and 8.722 mm^2, respectively. We also show the amount of force each nanopillar experienced in Figure 4-8. The results agreed qualitatively and quantitatively with the previous numerical simulations on the nanopillar LED's intensity's dependence on the external force [72]. The rubber testing surface had more "friction" with the tactile sensor and was able to create larger shear stress. In contrast, the photoresist testing surface was extremely smooth. It could only remain gripped to the tactile sensor until the incipient slip began to occur at around 6 kPa, in both X and Y directions. When the photoresist testing surface continued to glide across the tactile sensor, the fluctuation of the tactile sensor reading was observed in Figure 4-8B, from both the X and Y sensors. The photoresist slips from the tip of the nanopillar until the latter can grab the resist again as illustrated in Figure 4-9. Microscopically, the resist is not perfectly flat. Individual nanopillars do not always snap back to the same state each time. As a result, the slip leads to an intensity fluctuation which can be used to detect the incipient slip. Using a CMOS imager with a higher sensitivity can allow one to study the microscopic dynamics of the slip which will be investigated in future work. In contrast to the vision-based tactile sensor [9], [10], [54]–[59], our sensor's observation of the slip is direct and does not require any post-measurement computation.

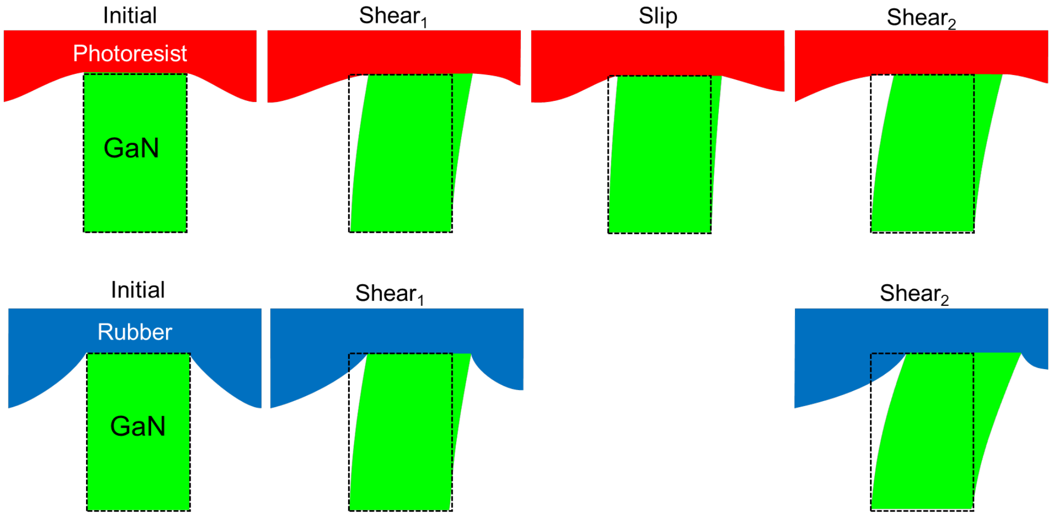

Figure 4-9: Schematic illustrating the light intensity from the nanopillar can start to fluctuate during the incipient slip. Without the slip (shown at the bottom panel), the nanopillar's deformation continues to increase with an increasing translation of the testing surface (photoresist or rubber) with respect to the tactile sensor. When the incipient slip occurs (shown at the top panel), the nanopillar can snap back. As the contacting surface between the testing surface and the nanopillar is not perfectly flat (see Figure 3-5), the snapback can vary from nanopillar to nanopillar. Further translation will continue to deform the nanopillar until another incipient slip. This process leads to intensity fluctuation as shown by the data points within the circles in Figure 4-8. The displacement shown of green nanopillars above are scaled by a factor of 20,000 for clarity. Adapted from [78].

4.6 Electrically Biased MichTac – Pushing the Minimization Limit

In this section, we overcame this challenge by using an ultrathin, conformally coated metallic layer as the p-type electrode. The ductility of the metal allows the electrode to deform together with the optically active elastic material without breaking. The sensor's performance was both theoretically and experimentally investigated. Using the principle of symmetry breaking, the direction of the force was determined by correlating the intensity data from two nanostructures of different spatial symmetry. We found our sensor's novelty is found in its ability to directly measure shear forces without complex interconnects. Previous optical tactile sensors rely on computer vision to estimate force vectors [26].

4.6.1 Methods

The tactile sensor was biased with a pulse mode (100 Hz, 10% duty cycle) to reduce the heating of the device which was not temperature controlled. We fixed the voltage and current at 6.9 V and 0.43 A, respectively. The distance between the electric probe for p-contact and the sensor was 1 mm with a resistance ~7 Ω which is attributed to the high operating voltage. It can be remedied by optimizing the layout of the electrical interconnects. The high operating current was due to the leakage current through pinholes in the electrical interconnects. GaN epilayers have a high density of defects which were enlarged into sizable V-shaped pits after the etching process. As a result, the planarization process used to remove SiO_2 covering the tips of the nanopillars may not completely cover all pits. Any insufficient covering led to the removal of the SiO_2 between n-GaN and the electrical interconnects. Indeed, we observed a short circuit for a small number of devices. An improved planarization process can improve the yield and the sensor's electrical property.

A stress applicator made with a UV-cured photoresist pad transparent at the wavelength of interest was mounted on a 3-axis translation stage. We monitored the frustrated total internal reflection to ensure proper contact between the resist pad and the tips of the nanopillars [72]. Once the contact was established, the Z-movement of the stress applicator was frozen, and a CMOS image sensor was set up to record the sensor's emission. We adjusted the frame rate of the CMOS image sensor so that each image recorded consisted of 160 emission pulses from our tactile sensor.

The measurement sequence is as follows. The stress applicator was translated either in the X or Y direction with a 50 μm increment. The image was then captured before the stress applicator was reset to the origin. The reset ensured that the relative intensity can be measured with respect to the zero-shear force. All images were recorded while the stress applicator was in a static state, and after the sensor was allowed to reach equilibrium. For each stress applicator translation step the average green channel value of each nanopillar array was extracted from the images collected by the CMOS imager. Relative intensity was calculated by normalizing the average green value from each sensor at each displacement against the respective 0 µm displacement image.

Figure 4-10 shows the relative intensity measured at different stress applicator positions. The results confirm that the tactile sensor is most sensitive to the shear force applied along the elliptical cross-section's long axis direction. By comparing the measured intensity of the nanopillars summarized in Figure 4-10 to the simulation results in Figure 3-4, we can deduce a shear force being applied with an increment of 8.9 kPa for every 50 µm of the applicator displacement. The sensitivity to the force along the long axis is 4 times that along the short axis.

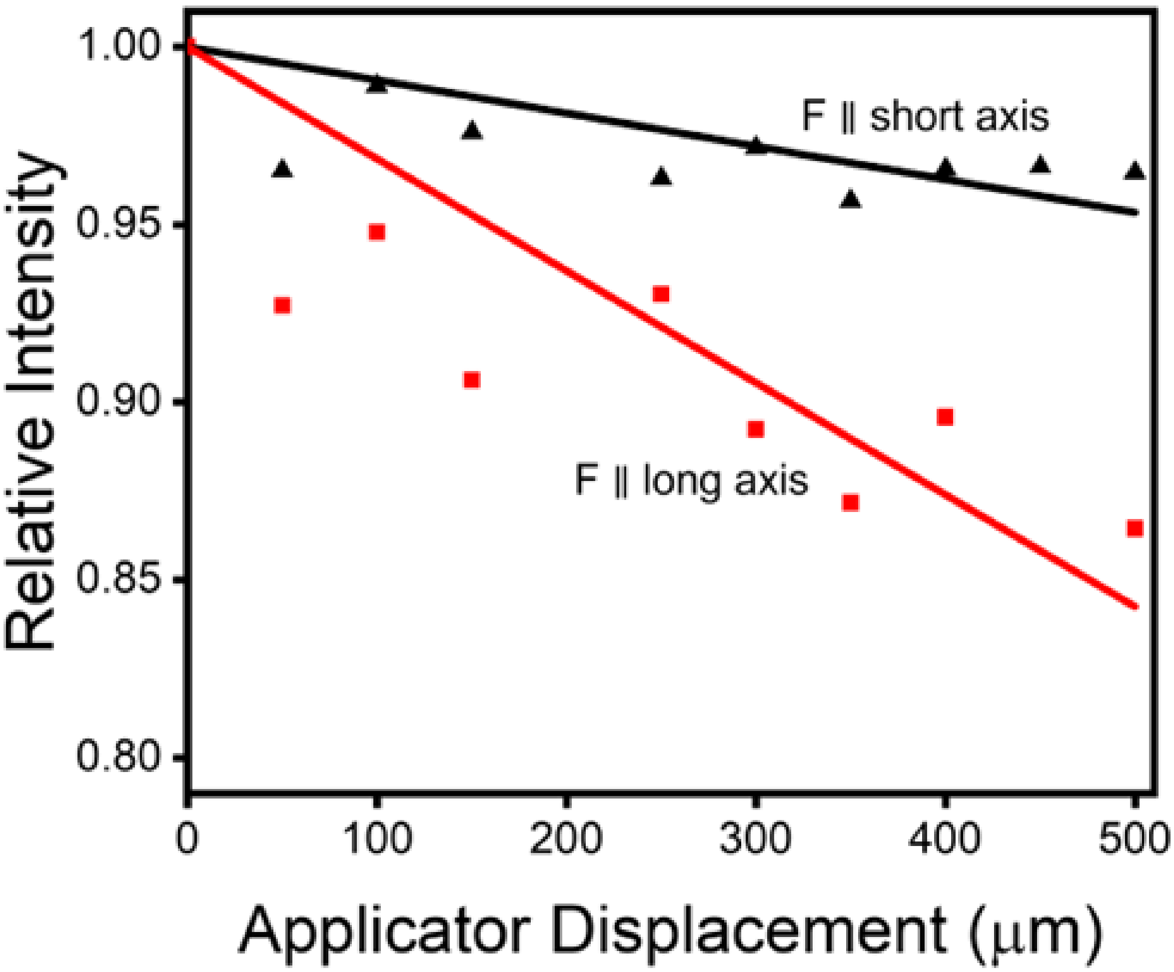

Figure 4-10: The response of the tactile sensor's emission intensity versus the stress applicator's displacement. The measured data is shown as points and the linear fit is shown as solid lines. The relative intensity is defined as the emission intensity at a certain applicator displacement divided by the intensity measured at a zero displacement. The red squares and line correspond to shear force which was parallel to the long axis of the nanopillars, and the black triangles and line correspond to shear forces parallel to the short axis. Adapted from [82].

4.7 Conclusion

In summary, we proposed and demonstrated a tactile sensor design with the potential of being implemented in an ultrathin form factor. We fabricated a proof-of-concept sensor array with a total area comparable to a fingertip. The sensor showed a dynamic range of 1 – 30 mN and an accuracy of ±1.3 mN. The sensor's building block is two sets of elliptically shaped and orthogonally oriented GaN nanopillar. The sensor operates with the principle that the separation of the electrons and holes in the nanopillar's radial direction depends on the force's magnitude while the nanopillar's dimension limits the total travel of the electrons. The latter enables the sensitivity to the force's direction. By focusing on the relative intensity of individual nanopillars before and after the force was applied, we showed that the sensor's performance did not depend on the array's uniformity. Furthermore, the use of an off-the-shelf image sensor eliminated the need for a custom 2D readout circuit.

The nanopillar LED consists of multiple disk-shaped InGaN quantum wells. Without an external force, the radial confinement potential confines the electrons and holes around the center of the nanodisk. With an external shear force applied, the electrons move off the center toward the force while the holes move away, albeit only slightly due to the heavy effective mass. Therefore, the emission intensity decreases with the force's magnitude. Decreasing the nanopillar's diameter limits the electrons' travel and the reduction of the emission intensity. Using these principles, an elliptically shaped nanopillar emits different intensities when the force is along a different direction of the ellipse. The combination of two different sets of nanopillars with their elliptical cross sections orienting orthogonal to each other allows us to measure the force's direction and magnitude in real-time. The current design distinguishes two forces with opposite directions using the time evolution data as shown in Figure 4-4.

We examined the limit of spatial resolution for our sensor. All the intensity data were obtained in the above discussions by averaging over each nanopillar LED's area 100 µm × 150 µm. Figure 4-11 compares the intensity data from sensor 1Y recorded during the fingertip experiment (see Figure 4-5(B)) with different averaging areas. As expected, the data becomes noisier when the area of integration becomes smaller. Nevertheless, sudden intensity drops identifying the passing of fingertip ridges can still be unambiguously identified (black arrows) in the data from a single camera pixel. In our setup (Figure 4-1), each CMOS imager pixel (4.3µm x

4.3μm) captures emission from a sample area of ~1 μm^2 which contains a single nanopillar, suggesting the lower limit of the sensor's spatial resolution is determined either by the density of nanopillars or by the imager's pixel size. In the limit when no optics is used, the imager's pixel size sets the spatial resolution. In both cases, the resolution limit can exceed the human capability (~40 μm).

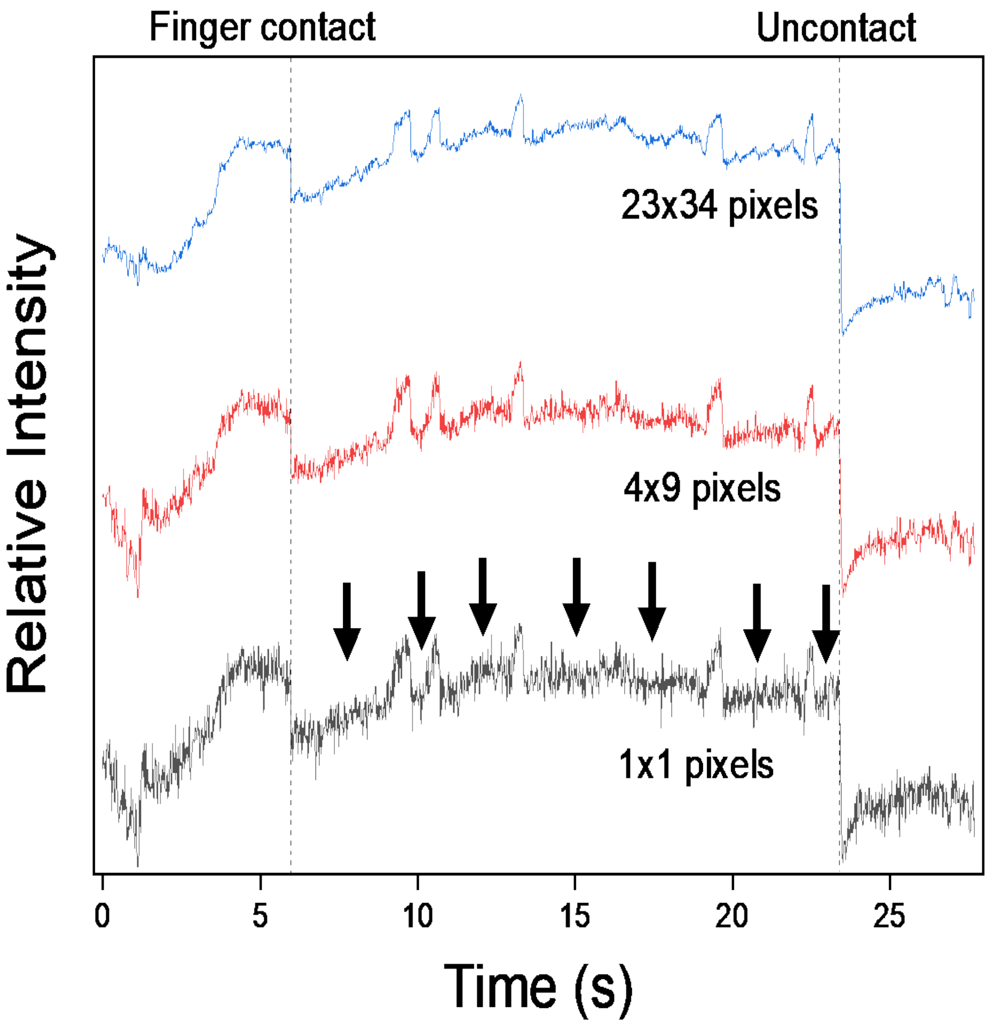

Figure 4-11: Determination of Sensor's Spatial Resolution. Comparison of the relative intensity of sensor 1Y recorded during the fingertip experiment using different areas of integration in terms of the number of imager sensor pixels. A series of black arrows marking the times when the fingertip's ridge passed sensor 1Y, as determined by the real-time camera image (Figure 4-5A) are also shown. Adapted from [72].

In our first experimental setup, we employed imaging optics to project the sensor array's image to a CMOS camera which was placed tens of centimeters away from the sensor. It is worth noting that the imaging optics is not essential for the sensor's functionality. What is critical is the ability to measure the relative intensities of individual nanopillar LEDs in real-time. Without the imaging optics, however, the divergence of LED's emission necessitates a close distance between the LED and the image sensor, which can be achieved by removing the sensor array's substrate, to maintain a high spatial resolution of the sensor. We showed that the smallest detectable area for our sensor is limited by the nanopillar's spacing (1 μm). Without the imaging optics, the divergence of the LED emission reduces the tactile sensor's spatial resolution. However, with the vertical stacking of a high-frame-rate image sensor after removing the tactile sensor's substrate, we expect the proposed design can detect a shear force riveling the human capabilities which have a spatial resolution of 40 μm and transient response as fast as 400Hz. It is also possible to design a flexible tactile sensor for prosthetic skin applications by integrating an organic image sensor.

Our second experiment demonstrated the direct measurement of a shear force with a calibrated magnitude using a GaN nanopillar LED-based tactile sensor. Both the magnitude and direction of the force were directly measured without the need to fit the data through a theoretical model or perform complex computations as in other vision-based tactile sensors. In other words, we experimentally validated the capability of the GaN tactile sensor to function as a force/torque sensor by itself. The torque measurement, while not directly demonstrated in this chapter, can be easily achieved with a multipoint measurement as has been shown previously[72]. All nanopillars are decoupled mechanically and electronically from each other. The change in emission intensity from each nanopillar is the result of a localized misalignment between the electron and hole wavefunctions. As a result, the mapping of the force field can be achieved with an extremely high spatial resolution, limited primarily to the resolution and sensitivity of the CMOS imager.

We also reported the capability of directly observing the incipient slip from the sensor reading without requiring any computation or prior assumptions of the testing surface's characteristics. As the force applied by the testing surface on the tip of the nanopillar exceeds the friction between them, the nanopillar "snaps back" until the friction and the applied force are in balance. This behavior mimics our subconscious modulation of the force between two fingertips when grasping an object to prevent a slip. The results pave the way for using our sensor with robot proprioception and visual feedback to complete grasping, pose estimation, and item discovery tasks requiring robots to determine the size and shape of an applied shear force.

In our third experiment, we demonstrated an electrically driven shear stress tactile sensor. The sensor design utilized light-emitting elastic semiconductor nanostructures whose emission intensity changed when the nanostructures were subject to an external shear force. The symmetry breaking of the light-emitting active region using an elliptical cross section leads to the sensor's sensitivity to the force's direction. Electrical operation was enabled using an ultrathin and conformally coated p-contact. Both the p-contact and the insulating dielectric were deposited using ALD. The sensor's functionality was not affected by these extra layers, validated both theoretically and experimentally. The thickness of the sensor's active layers is <1 μm. With the substrate's removal, the proposed design is readily compatible with a flexible sensing platform.

The simplicity of our sensor's interconnects allows our sensor to be easily scaled onto larger tactile sensor and custom-tailored to fit custom tactile sensing applications. The response of our sensor is ~100 Hz. Our sensor is not limited in response by the design of the nanopillar, but by the refresh rate of the CMOS imager. Future sensor platforms could utilize highspeed CCD imagers to push the detectable sensor response beyond ~1000 Hz.

Chapter 5 Applications of Tactile Sensing

This chapter presents MichTac's capability of superhuman tactile perception on an unmatched scale, providing contact location detection and quantified force feedback. Based on an array of GaN LEDs, our MichTac sensor showcases high sensitivity and speed in response to environmental forces and variations. MichTac aims to offer super superhuman resolution touch perception with calibrated force feedback to enable various novel capabilities previously not possible. We demonstrate several key tactile perception capabilities: reading microscale messages encoded onto a near perfectly flat plane, sensing pipe leakage, wide temperature operational range (-195 ºC to 120 ºC), material classification through touch, as well as evaluating against several existing vision-based tactile sensors. This chapter's objectives are to show our MichTac sensor's compatibility with a standard robot arm and evaluate unique capabilities beyond several existing sensors.

5.1 MichTac End Effector

We retrofitted a mature tactile sensing platform (GelSlim) with our optical sensor to add superhuman tactile perception to a robotic arm (Kuka R820 Med robot). Our sensor design easily enables this capability and demonstrates its utility and versatility for robotics applications. The MichTac platform is fabricated from a 3D printed housing, Raspberry Pi, Raspberry Pi spy camera, a 425 nm longpass filter, and six 405 nm UV commercial prepackaged LEDs. The completed tactile sensor was mounted to the Kuka and used for detecting small leaks on a pipe of compressed air. We used the MichTac End Effector for the material classification experiments, and the Micro-

Xili Yi developed the Surface Material Classification algorithm depicted in Figure 5-5.

Morse Code reading experiments described below, and the MichTac End Effector the sensor was mounted on a translation stage. The translation stage was driven by stepper motor for accurate speed and position control. For comparison experiments for material classification, GelSlim sensor and Soft Bubble sensors were mounted to the fingers of WSG50 gripper, which is mounted at the end effector of a commercialized robot arm (Kuka R820 Med robot). MichTac End Effector and GelSlim, the image signals are acquired using raspberry 3B and sent to a desktop via ROS network.

5.2 Micro-Morse Code

The phrase "Hello World" was encoded onto a single side polished sapphire wafer (Ra<0.35 nm and the wafer thickness is 530 μm) with photoresist (SPR 220 3.0) using contact lithography. We represented "dits" with a 200 μm wide photoresist stripe and the "dahs" by a 400 μm wide photoresist stripe. Within each letter, a pulse of "dit" or "dah" is separated by a 200 μm bare wafer stripe. Letters were separated by an 800 μm bare wafer stripe, and words were separated by a 1600 μm bare wafer stripe. The Morse code pattern height was measured via a Dektak XT stylus profilometer to be 1800 nm, or 2.76 times the height of the nanopillars. The Morse code wafer was translated across the nanopillar tactile sensor at a rate of 22 μm/sec and nanopillar responses were recorded at 120 frames/sec for 100 sec. To ensure consistent translation speed of the Morse code message the translation stage was driven with a stepper motor controlled by a waveform generator (Keysight 33600A). For each frame in the video the mean green value for the nanopillar arrays was monitored. The mean green values were smoothed using a Savitsky-Golay filter [83] to eliminate intrinsic noise from the CMOS imager. The peaks of the smoothed curve were fitted with a gaussian distribution and the full widths at half maximum (FWHM) of each peak were extracted.

Since the velocity of translation is constant the difference between the “dits” and “dahs” pulses can be determined by the FWHM of each peak. The median peak width of the “dahs” is twice the width of the “dits” which is consistent with the fabricated width of the respective pulse units.

The superhuman resolution of the nanopillar tactile sensor is put to the test when reading micro-scale morse code. The ability to encode imperceivable meta data onto a surface opens the possibility of a new way to teach tool manipulation to robotic arms and grippers. The identity and relevant parameters could be encoded onto the surface of a tool and read with the same gripper which handles them, eliminating the need for computer vision systems. We demonstrate superhuman tactile perception by reading the phrase “Hello World” which has been encoded in micro-scale morse code. The morse code was written on using polymer stripes with a height of 0.0018 mm, which is undetectable to human sight. Building upon Johansson's research, it is noteworthy that when a human finger slides across a surface, the dynamic nature of contact change and lateral force during motion yields a richer source of information, leading to enhanced Morse code reading proficiency, as compared to static contact [85], [86]. With this in mind, we read the micro-Morse code by sliding our tactile sensor across the message at a constant velocity rather than poking different areas. Our sensor detects the differences between a short or long pulse within the Morse code via morse code. The distinction between a short or long pulses versus time allows for the decoding of the micro-scale morse code [85], [86]. With this in mind, we read the micro-Morse code by sliding our tactile sensor across the message at a constant velocity rather than poking different areas. Our sensor detects the differences between a short or long pulse within the Morse code. The distinction between a short or long pulses versus time allows for the decoding of the micro-scale morse code.

In our first task, we demonstrate that our tactile sensor can read the phrase “Hello World” encoded as morse code onto an ultrasmooth surface, a single side polished sapphire wafer. A single pulse of the message is 0.0018 mm tall, about 1/100th the thickness of a human hair. The robot brings the nanopillar tactile sensor into contact with the sapphire wafer and translates the sensor across the wafer at a constant speed. The message’s pulses impart a force on the nanopillars, therefore by monitoring the decrease in emission of the nanopillar arrays the morse code message can be read and decoded. The constant speed of translation across the sensor enables the message pulses to be sorted into “dits” (short pulse) and “dahs” (long pulse). The nanopillar tactile sensor discerns between "dit" and "dah" pulses by capturing force data, in the form of relative light intensity decrease ($\Delta I\ /\ I\_0$), as it traverses the message at a uniform rate. Subsequently, the raw force data undergoes a refinement process through a Savitsky-Golay smoothing algorithm, which effectively eliminates thermal and flicker noise from the CMOS imager. The resultant smoothed force data is then subjected to Gaussian curve fitting, where individual peaks emerge to represent the distinct pulses of the message, this is demonstrated in Figure 5-1 Left Side. The critical metric of full width at half maximum (FWHM) is extracted from each fitted peak, and these FWHMs are methodically organized into a distribution where the median widths and outlying widths are identified. Finally, with the aid of this distribution, the sensor confidently assigns the appropriate labels of "dit" or "dah" to the respective peaks of the message, facilitating the precise reconstruction of the message. The assignment of peaks and the distribution of the peaks is shown in Figure 5-1 Bottom Right. The ground truth is plotted along the x-axis and the peak assignment is plotted along the y-axis. The nanopillar sensor sorted the peaks with 100% accuracy. We attempted to read the micro-Morse code message using a Gel-Slim tactile sensor, but the micro-morse code could not be detected.

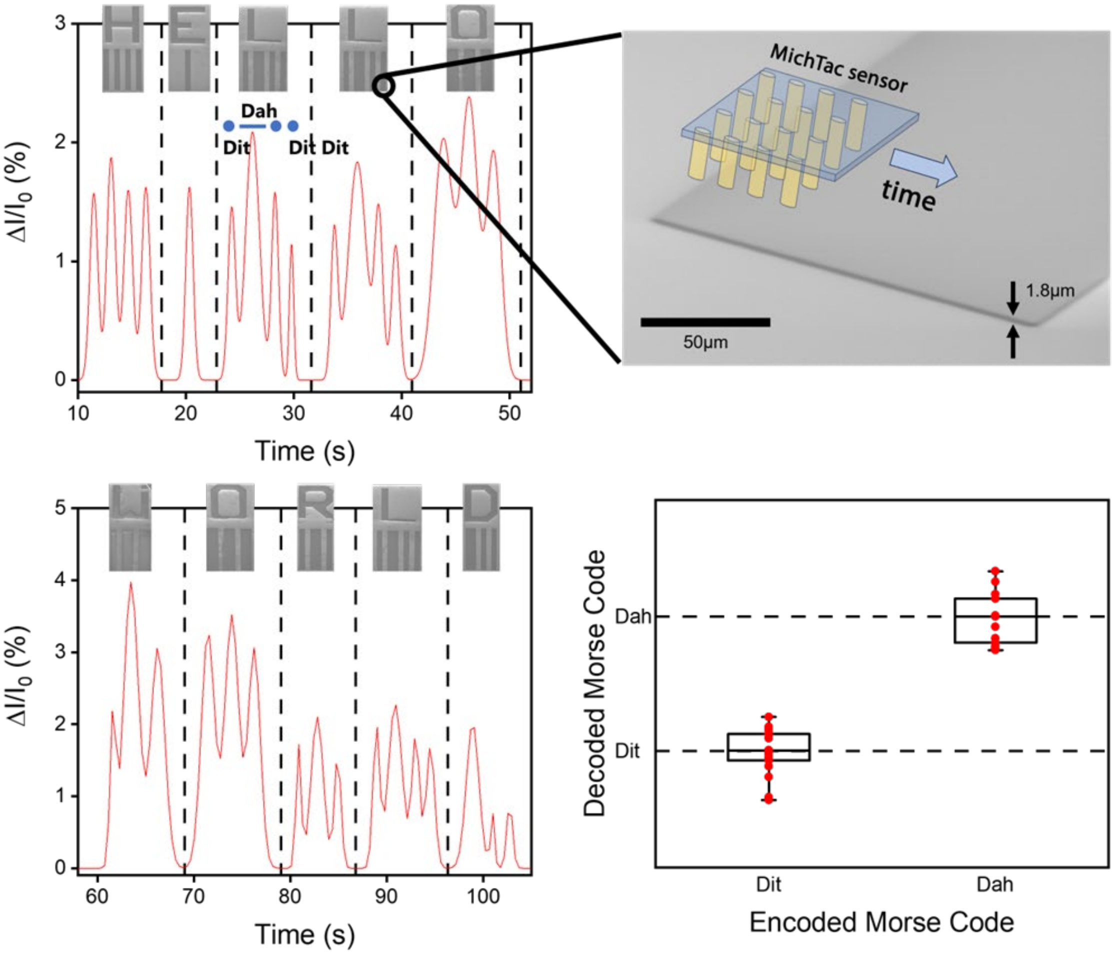

Figure 5-1: (Left Side) Sensor fitting of the micro-morse code. SEM micrographs are shown above each letter pulses for clarity. (Top Right) Cartoon of MichTac interacting with a SEM micrograph pf a “dit” stripe within the letter “L”. (Bottom Right) Morse code decoding distribution. The ground truth is illustrated on the x-axis, and the assigned value of each peak is shown on the y-axis. Each pulse length distribution is a box and whisker plot showing the median, 25th and 75th percentiles, and outliers.

5.3 Leak Detection

We built a controlled leaky pipe using PVC and compressed air. A 600 mm by 63.5 mm PVC pipe was fitted with end caps and glued together to maintain an airtight fit. A 1.5 mm hole was drilled into the pipe side wall to simulate a leak. One end cap was fitted with a ball valve to allow controlled pressurization of the PVC pipe. The entire pipe was painted black to obscure the 1.5 mm hole. The goal of painting the pipe was to make the hole impossible to see with vision-based systems. The ball valve was connected to a compressed air regulator set to 20 psi. Eight on/off cycles were completed with varying length of the on or off states. We chose to vary the on or off states to check the sensors accuracy.

Since our sensor relies on monitoring changes in nanoscale LED emission brightness, we do not want changes in environmental brightness to create false positives during leak detection. To combat this, we 3D printed a cover to block light from the environment and direct airflow across the sensing surface.

Measuring ultrafine fluid flow is a challenging capability requiring fine spatial resolution sensing. This capability has numerous applications, here we focus on detecting minute flows such as those found during house inspections for leaking gas lines, detection of signs of life through breath, and blood flow in the arterial line. Sensing leaks remotely using a robotic system is essential for hazardous and remote environments. Critical infrastructure for transporting fluids often exists in environments which are not easily accessed by humans, require additional protective equipment to inspect the infrastructure, or even the fluid being transported is hazardous to human inspectors.

The task is visualized in Figure 5-2. The goal of the robot is to detect the unknown location of a minute leak along the pipe. The robot translates the sensor perpendicular to the surface of the pipe to detect the small leak autonomously. We simulated a leaky pipe using a 63.5 mm diameter PVC pipe with a 1.5 mm diameter aperture along the sidewall to function as a leak. 20 psi of compressed air is supplied via a ball valve to the pipe. The pipe has been painted black to demonstrate our sensor's ability to find leaks where vision based tactile sensors cannot. We validated the effectiveness of our tactile sensor in detecting leaks on a simulated leakage by intermittently activating and deactivating the air supply to the pipe and recording the state of the ball valve (on or off). Simultaneously, the tactile sensor was allowed to operate continuously, capturing, and collecting force data throughout the experiment. Figure 5-2B demonstrates the validation of our tactile sensor through the congruence observed between the sensor data and the ground truth data. The sensor's data mirrored the moments when the air supply was engaged or halted, effectively and reliably identifying the occurrences of leaks. This tangible alignment between the sensor's readings and the known ground truth confirmed the sensor's ability to detect leaks accurately and efficiently on the simulated leaky pipe, underscoring its robust performance and practical applicability. Figure 5-2C and Figure 5-2E depict autonomous leak detection.

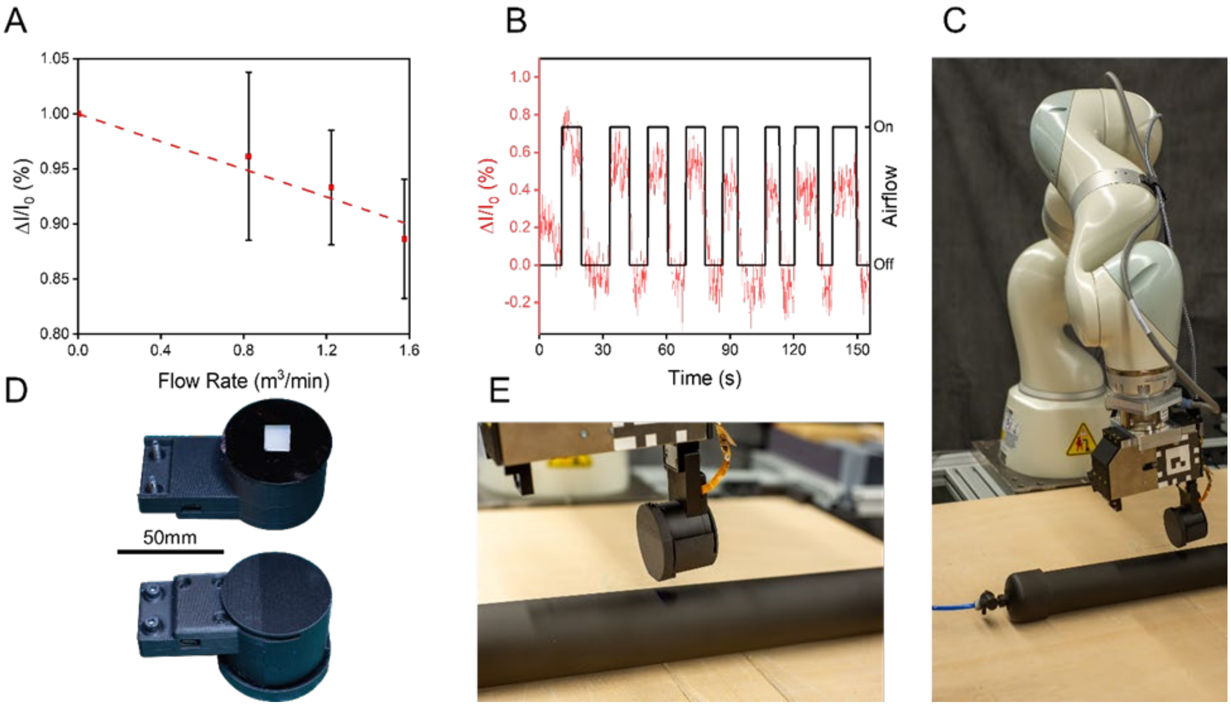

Figure 5-2: (A) Calibration Experiment. (B) leaky pipe detection. The red curve shows the intensity change of the tactile sensor and the black curve shows the ground truth of the airflow. The airflow was cycled on and off 8 times with varying widths to check the sensors accuracy. (C) Kuka robotic arm checking for leaks. (D) Close up of the tactile sensor. (D top) Tactile perception packaging and (D bottom) airflow sensing airduct attachment. (E) Close up of leak detection test.

5.4 Extreme Temperature Tactile Sensing

Temperature control was achieved with a cold finger continuous flow cryostat (Janis ST-100) equipped with a resistive heater and liquid nitrogen as the cryogen. Due to the small internal volume of the vacuum jacket a custom translation stage needed to be designed to apply shear force. The translation stage consisted of a stepper motor (Adafruit NEMA-8) with 200 steps per revolution which drove a 250 µm per revolution lead screw thus achieving a minimum step size of 1.25 µm. The lead screw moved a silicon rubber stress applicator. Silicon rubber was chosen for its compliant nature and resistance to elevated temperatures. The compliant nature of the silicone rubber ensured consistent contact with the tactile sensor. The structural components of the translation were 3D printed from nylon embedded with carbon fiber (Markforged Onyx Filament), which is rigid at temperatures below 140 ºC. FIGURE depicts the experimental design of the translation stage and the experiential design for extreme environment tactile sensing.

The CMOS imager viewed the tactile sensor via an optical access port on the cryostat, thus decoupling the tactile sensor from the data collection and processing equipment. A microscope was used as the imaging optics with a 425 nm longpass filter fitted in the optical path of the microscope to block the pump laser emission. The decoupling of the sensor and analysis components allows our tactile sensor to operate in extreme environments. To demonstrate this claim, we achieve tactile sensing at both extreme cold (-195 ºC) and hot (120 ºC).

A single tactile stress measurement is collected as follows. The stress applicator is translated over the tactile sensor in 50 µm steps and at each step an image is collected and normalized against the 0 µm translation image, thus giving us the relative intensity of the tactile sensing arrays versus displacement. To ensure consistency and repeatability of the measurement both the translation stage and CMOS imager were operated autonomously via a microcontroller (Arduino Mega 2560) and the tactile sensor was not removed from the cryostat between measurements. The translation stage was bolted directly to the sample mount of the cryostat to ensure the same normal force was applied for every data collection run.

A baseline measurement of the tactile sensor's sensitivity was recorded at room temperature (20 ºC). The resistive heater driver ensured there were no temperature fluctuations during this experiment to ensure only the brightness change of the nanopillars was in fact from shear force application and not temperature fluctuation. Next, the tactile sensor was heated to 120ºC with the resistive heater and allowed to stabilize. Another tactile sensing measurement was recorded at 120ºC. After the conclusion of the 120 ºC measurement, we began cooling the sample with liquid nitrogen. We then conducted tactile measurements at: 0 ºC, -20 ºC, -40 ºC, -50 ºC, -100 ºC, -150ºC, and -196ºC, respectively. The temperature of the tactile sensor was stabilized with the resistive heater during each measurement. We found that if the tactile sensor was cooled directly to -196ºC the stepper motor would freeze up, so we opted to take the measurement previously listed to keep the internal components of the stepper motor warm and functional. We achieved directional tactile sensing within extreme environments with similar sensitivity to room temperature operation. Demonstrated in Figure 5-3 is the response of our MichTac to applied shear force.

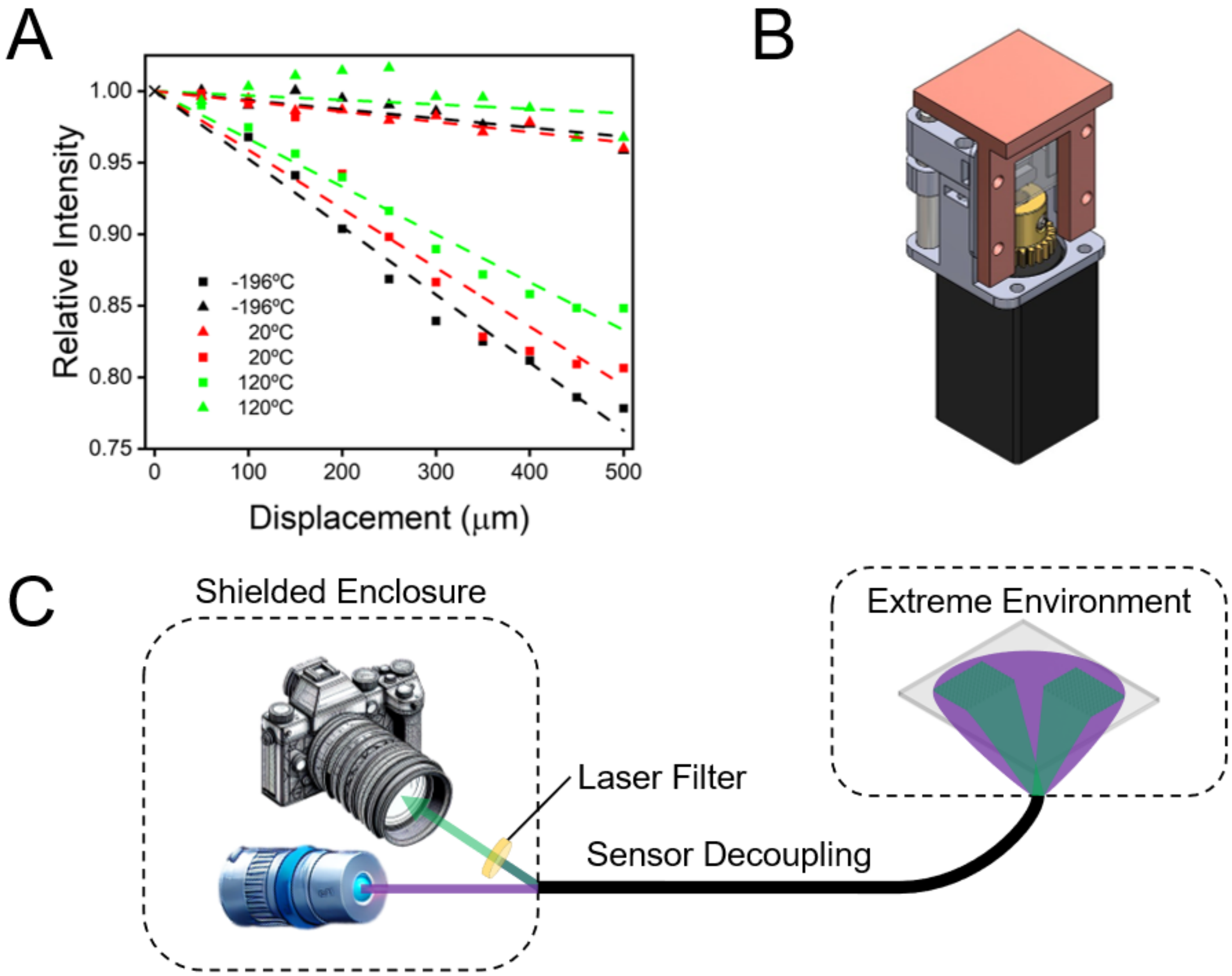

Figure 5-3: (A) MichTac sensor response. Square points refer to the response of the sensor array with sensitivity parallel to the applied shear force and triangular points refer to the sensor array perpendicular to the applied shear force. Room temperature (20 ºC) measurements are represented in red, high temperature (120 ºC) in green, and extreme cold (-196 ºC) in black. Linear fitting of the data is represented with a dashed line of the respective color. (B) 3D CAD model of the translation stage used for the experiment. (C) Conceptual figure of extreme environment tactile sensing. The laser filter is a 425 nm long pass filter, which blocks 405 nm bias laser and allows the 540 nm emission of the nanopillars to reach the CMOS image sensor.

5.5 Surface Material Classification through Touch Frequency Data

Classifying materials through tactile sensing is an important ability for manipulating. Owing to both the sensor's high spatial resolution and shear measurements, it is possible to infer micro-scale material properties such as texture and friction that are key to inferring object categories when aggregated across space and time. Much like micro-Morse code, integral role of shear forces in reading and texture estimation provides more information of the contact surface.

[87]. Similarly, by sliding our tactile sensor on different surfaces, and analyzing the signal along both spatial and time horizon, we can discern different surfaces.

The experimental setup is depicted in Figure 5-4. The robot is equipped with a tactile sensor and brushes each of the 6 test objects (shown in Figure 5-4A) with a constant velocity. The goal of the experiment is to guess the object category given tactile sensory feedback. We evaluate the efficacy of our sensor against two common vision-based tactile sensors (Soft Bubble and GelSlims), which is also shown in Figure 5-4B**.**

We take a data-driven approach to analyze images from our sensor. We employ a Long-Short Term Memory Convolutional Neural Network (LSTM-CNN) (details in Methods section) whose inputs are sequences of image reading from sensor, the speed of motion, and desired normal force, and output is a label prediction. We train the model on our dataset, which is collected on 6 different surfaces. We evaluate the model on unseen surfaces of the same materials. The results are presented in the confusion matrices in Figure 5-4C**.** and Table 5-1**.** The table suggests that our tactile sensor is outperforming classification 28% better than Soft Bubble, and 45% better than GelSlim. Figure 5-4C**.** shows the confusion matrices of classification using all three sensors. With only 6 classes, our MichTac sensor can distinguish between all test surfaces successfully, while the other sensors all struggle with some surfaces, due to the lack of high resolution and sensitivity.

Our Nanopillar sensor can classify materials by interacting with the materials' surface using high spatial and time resolution measurements. To utilize these properties, we need to first pre-process and then use a LSTM-CNN structured network to get the accurate surface classification.

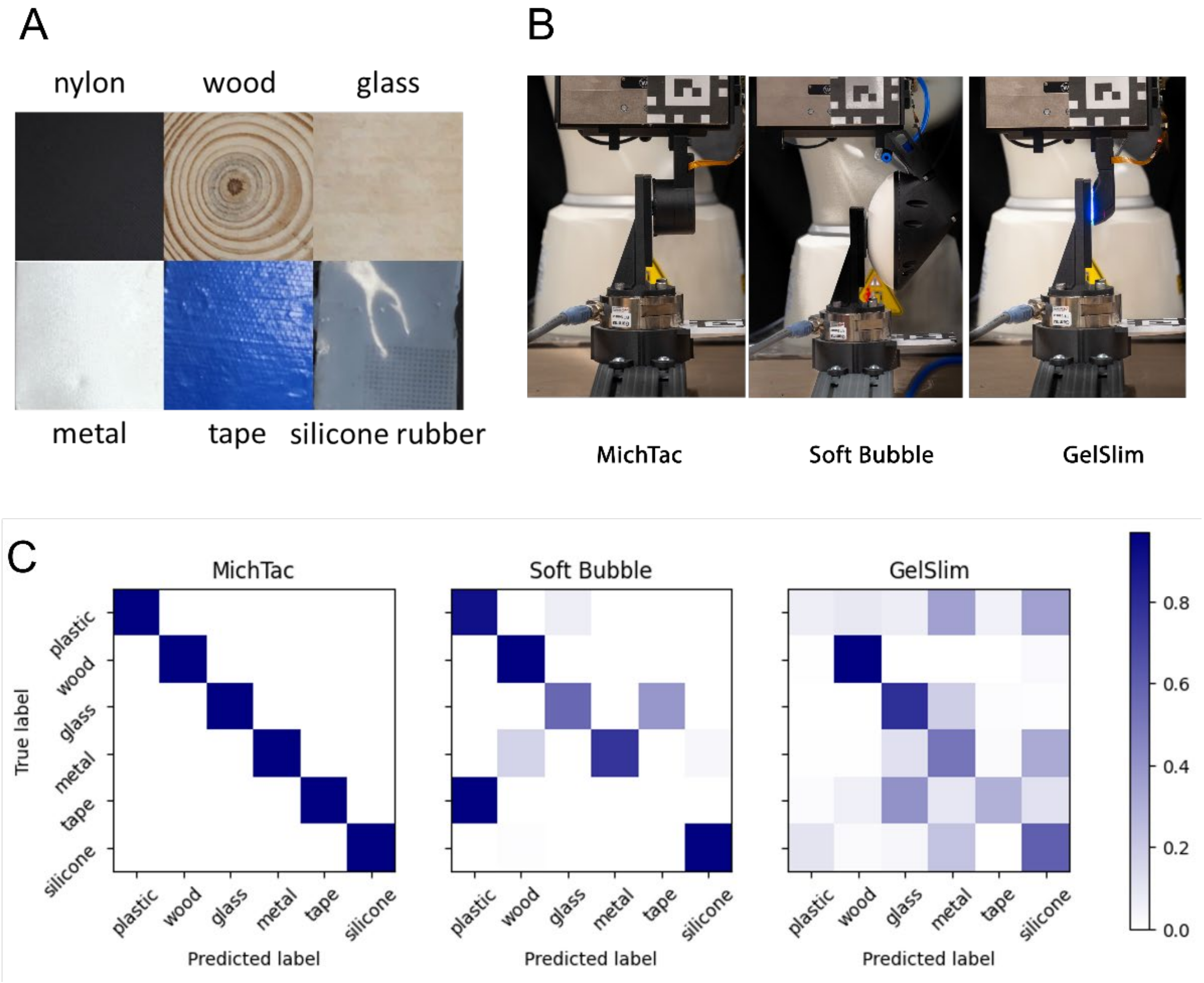

Figure 5-4: (A) Pictures of 6 test surfaces for classification, they are nylon, wood, glass, metal, duct tape, and silicone rubber. (B) Pictures of experiment setup for our MichTac sensor, Soft Bubble, and Gelslim sensors. The sensor is attached to a robot arm, and test surface material is attached to a vertical plane mounted on an ATI gamma 6DOF force/torque sensor. (C) Surface detection results of these 3 different tactile sensors, shown as confusion matrices. The rows represent material ground truth, and the color in each block represents the percentage of prediction that think it belongs to the material of the corresponding column.

5.5.1 Pre-processing:

For raw image measured from CMOS, we crop the area with nanopillar, and combined them with their relative pose. Considering that there are two sets of nanopillars, one sensitive to along x-axis, the other sensitive to along y-axis, we make them into two image channels.

Considering that different materials have different reflection rate, which may influence the measurement of illumination of each pixel, also to get more information from texture reading by different illumination signal, we pre-process images with FFT, then apply low pass filter of 6 pixels on it to reduce the non-texture signals.

5.5.2 Network structure:

The input includes processed FFT images, desired normal force, and desired speed. In the network, we first pass each image in images queue through CNN, which is used to extract texture information from raw images and reduce the size, then concatenate with nominal force and nominal speed. After that, we pass the sequence of concatenated image, force, and speed information through LSTM, which can utilize the information along path of certain path. We use cross-entropy Loss in this model, as this is a standard classification task.

5.5.3 Comparison experiments:

To compare the capability of this new type of tactile sensor with contemporary vision-based tactile sensors such as Soft Bubble or Gelslim, we design experiments to match their capacity, though they have different scales in size, measurement range, and stiffness. In our experiments design, we make all sensors under similar contact pressure, but not force. However, to show the ability of detecting micro-structure of varied materials, we keep the same test materials for all sensors, but varied sizes.

As for speed, we keep similar pixel-wise speed while sliding on test surfaces, which means we keep the similar same with unit of [pixel/sec]. Since different sensors use different visual signals with different physical meaning, for each sensor we stack all channels together and use the same classifier structure for comparison. Moreover, we resize and crop all images to keep the same resolution as nanopillar input size for fair comparison. For Soft Bubble sensor, we stack the depth images with shear flow images. For GelSlim sensor, we stack the RGB channels. The other parameters of the network also change with dimension differences, but we keep the same resolution. We also keep constant exposure parameter for each sensor to obtain stable and repeatable measurement.

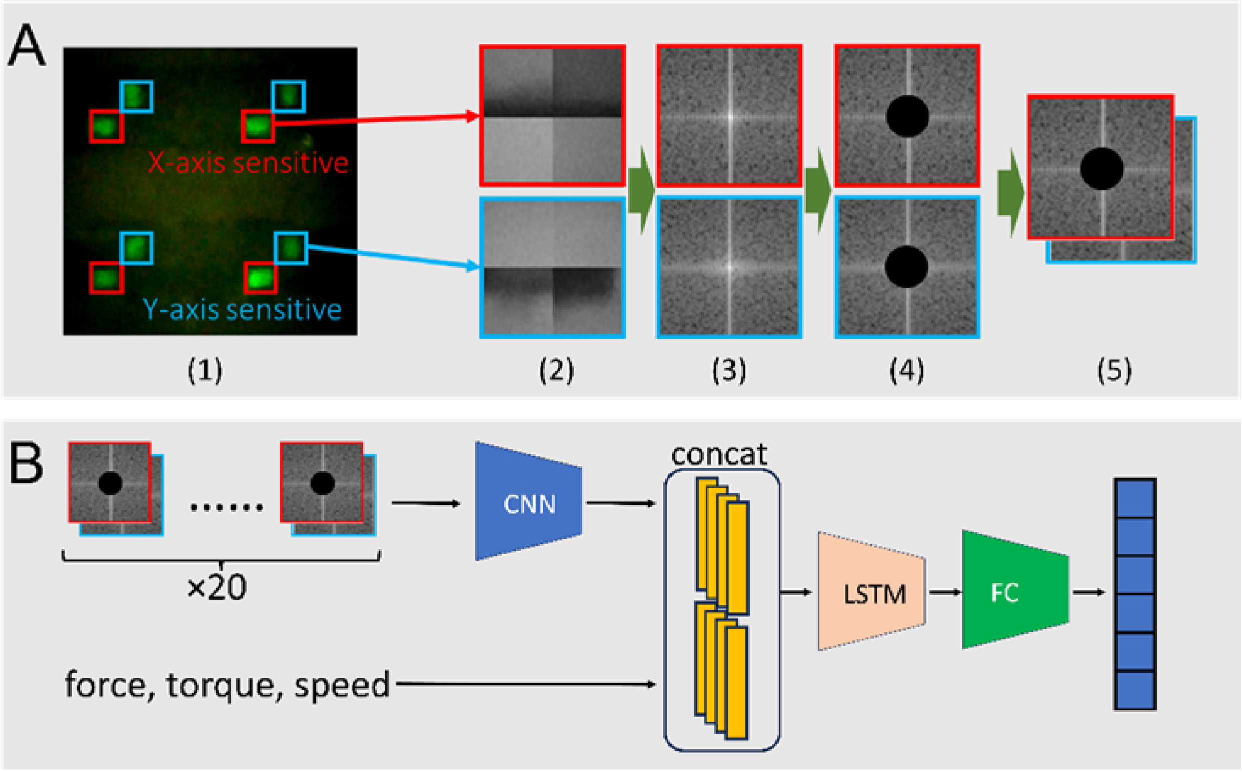

Figure 5-5: Illustration of the data process procedure. (A) Pre-processing procedure: (1) picking the sensing area, (2) reshape to square, (3) FFT of the image, (4) low-pass filter on FFT image, (5) stack to a new 2-channel image. (B) network structure: we pass image queue to CNN, then concatenate with nominal force and nominal speed information, then pass them through LSTM and a FC network, the output of this network is predicted label.

Table 5-1: Classification accuracy of the same materials among MichTac, Soft Bubble and GelSlim sensors.

Sensor	MichTac	Soft Bubble	GelSlim
Classification accuracy	100%	72%	54%

5.6 Conclusion

MichTac embodies a host of inherent attributes that set it apart. Its diminutive size, combined with an abundant array of tactile sensing elements and a low fill factor, render it exceptionally versatile for a wide spectrum of applications. These attributes enable the utilization of cost-effective materials, including LED epitaxial layers with high defect concentrations, which bolster the sensor's robustness and adaptability across a myriad of use cases. From small-scale devices to large, complex robotic platforms, our sensor seamlessly integrates into various systems, ushering in a new era of tactile perception in robotics and fostering widespread adoption across diverse industries.

The foundation of our sensor's robustness lies in the extensive arrays of tactile sensing elements, our methodology for measuring relative intensity change, and the carefully chosen sensor material system. These elements combine to create a level of resilience that is truly unparalleled. The low fill factor, characterized by a reduced surface area for individual sensing elements, significantly minimizes the impact of material defects, especially when compared to resistive and capacitive devices that are highly susceptible to such issues. Furthermore, the sensor's abundant tactile sensing elements are strategically positioned to distribute the sensing workload, ensuring consistent performance, adaptability to various surfaces, and stress resilience.

An instrumental component of our sensor's robustness is our approach to measuring relative intensity change. This method, which allows for continuous monitoring and real-time adjustments, safeguards the sensor against degradation, ensuring that sensor accuracy remains unaffected, even in the face of damaged sensing elements. This method compensates for data loss by discerning relative changes in intensity, thus preserving the accuracy of tactile sensing.

Throughout this investigation, we have established GaN nanopillar LEDs as highly capable tactile sensors in environments exhibiting extreme thermal variations, such as those found on extraterrestrial surfaces like the International Space Station (ISS). Our study not only demonstrates the viability of GaN as a superior material for constructing resilient, high-fidelity sensors but also validates the innovative application of GaN nanopillar LEDs as tactile transducers under both cryogenic and elevated temperatures. The unique optomechanical properties of our GaN nanopillar LEDs have provided a pathway to tactile sensors that can withstand and function under severe thermal stresses where traditional sensors would fail. Through rigorous testing, we have shown that these sensors can operate across a wide temperature range, remaining sensitive to minute pressure changes and offering spatial resolution capable of enhancing robotic and human tactile interfaces in space exploration scenarios. We observed that the tactile sensor reported less force applied by the stress sensor at elevated temperatures. We concluded the stress applicator became more pliable at elevated temperatures thus imparting a smaller force for an equivalent displacement at room temperature. The opposite was observed for the cryogenic temperatures. When the stress applicator was cooled it became more rigid, thus becoming less pliable and imparting a greater force on the tactile sensor.

Tool manipulation within a temperature range of -157 to 121 ºC occurs on the hull of the International Space Station. We demonstrated MichTac, in an optically biased format, achieving tactile sensing at temperatures as low as -195 ºC and as high as 120 º C. The adoption of this tactile sensing technology promises a variety of advancements. In space, the implementation of our GaN nanopillar LED sensors on external manipulators, tools, and suits could provide astronauts and robots with improved tactile feedback, significantly enhancing operation safety, dexterity, and task completion efficiency. Moreover, the robustness of our sensor design encourages their utilization in hostile environments found in deep-sea exploration, high-temperature processing industries, and in various defense applications.

In conclusion, the collective power of a low fill factor, an extensive array of tactile sensing elements, and our approach to measuring relative intensity change empowers our sensor with exceptional robustness. It thrives in real-world applications, demonstrating an innate ability to adapt and provide uninterrupted tactile sensing, even in the presence of individual element failures or adverse conditions. This technology is poised to redefine the boundaries of tactile perception and sensor design, offering unparalleled flexibility and resilience in a rapidly evolving technological landscape.

Chapter 6 Conclusion

Within this work we have developed a novel tactile sensor, MichTac, which used stoichiometric wurtzite gallium nitride nanopillar light emitting diodes (650 nm x 360 nm x120 nm) to measure and map the size, shape, direction, and magnitude of low magnitude shear forces. MichTac was fabricated using standard semiconductor processing techniques (photolithography, dry etching, wet etching, physical vapor deposition) MichTac can successfully complete tactile sensing tasks in a laboratory setting or complete real-word tasks with the help of a highly trained and practiced operator.

First, we proposed a new method of sensing and mapping low magnitude shear forces. Under an applied tactile force, the band structure of MichTac LED nanopillar transducers changes. We can observe and quantify this change through monitoring of the light emission of the LED and derive a relationship between light emission intensity and applied shear force. This method of tactile sensing yields a simple to measure and nearly instant direct force measurement. MichTac possesses the unique ability to fill many roles because it can be custom tuned for a specific application (i.e. addition of electrodes for ultrathin applications, modification of nanopillar dimensions to change dynamic sensing range, addition of imaging optics for high resolution tactile sensing).

Second, we designed a toolkit for application specific tuning of MichTac. This toolkit combined quantum simulations with mechanical force simulations to best model the expected behavior. This toolkit allowed us to predict the behavior of MichTac before fabrication, which streamlined production and focused evaluation experiments. Essentially, we knew how to test MichTac effectively before it was even fabricated.

Third, we evaluated the performance of MichTac and compared observed results with the expected behavior predicted by the design toolkit. We demonstrated MichTac could sense the direction and magnitude of and applied shear force. MichTac could also determine the shape of the force contact patch and map the movement of the force in two dimensions. This evaluation extended to two configurations of MichTac, an optically biased large footprint configuration and an ultrathin electrically biased configuration. We found MichTac's dynamic range of sensitivity of 0-1MPa and a spatial resolution of 3.72 µm which exceeds the ~40 µm resolution of human fingertips.

Lastly, we tested MichTac against real-world tasks. MichTac was able to detect and reconstruct a micro-morse code message which was imperceivable to human sight. A leak on a pipe could be remotely located using MichTac and a robotic arm. Characterization of an unknown surface could be completed using MichTac with 100% accuracy, which outperforms other robotic tactile perception sensors by a wide margin (28% improvement when compared to Soft Bubble). MichTac could also perform tactile sensing with regions of extreme heat (120 ºC) and cold (-196 °C) at low pressure (10^{-6} Torr).

6.1 Future Work

The future of MichTac envisions a refined platform with commercial viability. We foresee five topics of research where if completed could transfer MichTac from laboratory operation which requires highly skilled individual to operate into a household commodity. First, removal of the ridged substrate would allow MichTac to be integrated onto arbitrary surfaces which would promote the next generation of prosthetic devices. Second, improved packaging design for ultrathin, artificial skin platforms. Third, improvements of low temperature measurements. Fourth, expansive study of integrating machine learning into MichTac's operation to remove the need for a skilled operator. Fifth, increased comparative testing between MichTac and other mature tactile sensing technologies to better understand where MichTac performs best.

6.1.1 Thin Film Integration:

The ridged substrate of MichTac limits potential applications. Removal of the rigid substrate will allow MichTac to be integrated onto prosthetic devices and smart clothing. The intermediate goal is to remove the rigid carrier substrate from the GaN nanopillar tactile sensor and transfer it to the fingertip pad of an artificial finger. Within semiconductor manufacturing there already exists a mature technology for separating epitaxial layers from their growth substrate using laser ablation. Finding such a system and collaborating with the system's owner would solve this research challenge. The next step to improve MichTac would require developing a method to safely bond the free epitaxial layer, which is the MichTac sensor, to an arbitrary surface such as a fingertip or flexible image sensor.

6.1.2 Artificial Skin Packaging

There are two research challenges which hinder MichTac's ability to serve as an artificial skin.

1. Elimination of ambient light noise.
2. Resolution of nanopillar arrays without imaging optics.

Development of an ultrathin light cladding layer which is opaque would improve the performance of MichTac in bright environments. The cladding must be ultrathin to maintain the low profile and flexibility of the nanopillars LED on MichTac. A conformal layer with a material which can be deposited via ALD would be ideal.

Artificial skin applications require a sensor profile which is too thin to include imaging optics. Without imaging optics, the emission from multiple sensor arrays on MichTac overlap and tactile sensing becomes impossible. The addition of a mask to the back side of MichTac with windows for the arrays would eliminate cross talk between the array of MichTac. A bonus of this back side mask is a reduction in noise from ambient light.

6.1.3 Improvements of Low Temperature Measurements

Chapter 5 discussed and demonstrated tactile sensing within an extreme environment. The results demonstrated should be regarded as a proof-of-concept experiment since measurement of force was not achieved. Improvement upon this idea requires further testing and experimental design. The experiment performed in chapter 5 was limited in its scope due to the size constraint of the vacuum jacket of the cryostat (1.25 inches in diameter). Further works should focus on the inclusion of a small footprint semiconductor load transducer or a larger cryostat to accommodate a commercial load cell. Continued experiments should be performed at various temperatures, not just extreme cold, to uncover new applications of MichTac.

6.1.4 Machine Learning Expansion

Further investigations of integrating the MichTac platform with a machine learning algorithm will create a robust generalizable platform for tactile sensing. Development of a convolution neural network (CNN) with a long short-term memory (LSTM) architecture to analyze the shape, size, direction, velocity, and applied magnitude of applied shear forces will solve this research goal. To build this algorithm, MichTac will need to be exposed to a wide array of surfaces, contact pressures, and translation velocities. The intermediate goal of my research would be to collect enough data sets with a large variance to effectively train the CNN-LSTM algorithm. A successful algorithm will be able to determine the contact patch size, motion of the contact, force applied, and material imparting the shear force. The experiment outlined in chapter 5 should be used as a jumping off point for future investigations.

With enough data collected analysis of the generalizability of MichTac as a tactile perception can be completed. The goal is to make the MichTac tactile perception algorithm robust enough so that any arbitrary surface can be grasped by a robot.

6.1.5 Comparative Testing:

As mentioned in chapter 5, the standard for gripping applications has been set by GelSlim and Soft-Bubble. Comparing the effectiveness of the GaN nanopillar tactile sensor and CNN-LSTM algorithm to GelSlim and Soft-Bubble would provide a valuable benchmark. The intermediate goal of this objective would be to complete a rigorous test gauntlet to evaluate each sensor on grasping and material categorization tasks. The gauntlet will include pose estimation, material classification, and force measurement exercises. Each sensor will be evaluated for accuracy and precision when completing each task.

Appendices

Appendix A: Nextnano Device Simulation

All nextnano Simulations are available at https://drive.google.com/drive/folders/1_jfU8-7kCQH6vHMXbXkddzyO_pbCQ0Xm?usp=sharing.

Appendix B: Mechanical Strain Simulations

All COMSOL Simulations are available at https://drive.google.com/drive/folders/1_jfU8-7kCQH6vHMXbXkddzyO_pbCQ0Xm?usp=sharing.

Appendix C: Strain Addition

The Python code to generate the total strain profile from the intrinsic strain from nextnano and the mechanical strain profiles is available at https://drive.google.com/drive/folders/1_jfU8-7kCQH6vHMXbXkddzyO_pbCQ0Xm?usp=sharing.

Appendix D: Light Emission Calculation

The Matlab code which calculates the emission intensity is available at https://drive.google.com/drive/folders/1_jfU8-7kCQH6vHMXbXkddzyO_pbCQ0Xm?usp=sharing.

Bibliography

[1] V. E. Abraira and D. D. Ginty, "The Sensory Neurons of Touch," *Neuron*, vol. 79, no. 4, pp. 618–639, Aug. 2013, DOI: 10.1016/j.neuron.2013.07.051

[2] J. W. Morley, A. W. Goodwin, and I. Darian-Smith, "Tactile discrimination of gratings," *Experimental Brain Research*, vol. 49, no. 2, pp. 457–472, Feb. 1983, DOI: 10.1007/BF00238588

[3] M. R. Tremblay, W. J. Packard, and M. R. Cutkosky, "Utilizing sensed incipient slip signals for grasp force control," *Flexible Automation 1992*, pp. 1237–1243, 1992.

[4] Y. N. Turrell, F. X. Li, and A. M. Wing, "Estimating the minimum grip force required when grasping objects under impulsive loading conditions," *Behavior Research Methods, Instruments, and Computers*, vol. 33, no. 1, pp. 38–45, 2001, DOI: 10.3758/BF03195345

[5] R. W. Van Boven and K. O. Johnson, "The limit of tactile spatial resolution in humans," *Neurology*, vol. 44, no. 12, pp. 2361–2361, Dec. 1994, DOI: 10.1212/WNL.44.12.2361

[6] J. D. Lieber and S. J. Bensmaia, "High-dimensional representation of texture in somatosensory cortex of primates," *Proceedings of the National Academy of Sciences*, vol. 116, no. 8, pp. 3268–3277, Feb. 2019, DOI: 10.1073/pnas.1818501116

[7] L. Skedung, M. Arvidsson, J. Y. Chung, C. M. Stafford, B. Berglund, and M. W. Rutland, "Feeling small: Exploring the tactile perception limits," *Scientific Reports*, vol. 3, 2013, DOI: 10.1038/srep02617

[8] R. Dahiya, N. Yogeswaran, F. Liu, L. Manjakkal, E. Burdet, V. Hayward, and H. Jorntell,

“Large-Area Soft e-Skin: The Challenges beyond Sensor Designs,” *Proceedings of the IEEE*, vol. 107, no. 10, pp. 2016–2033, 2019, DOI: 10.1109/JPROC.2019.2941366

[9] E. Donlon, S. Dong, M. Liu, J. Li, E. Adelson, and A. Rodriguez, “GelSlim: A High-Resolution, Compact, Robust, and Calibrated Tactile-sensing Finger,” *IEEE International Conference on Intelligent Robots and Systems*, pp. 1927–1934, 2018, DOI: 10.1109/IROS.2018.8593661

[10] A. Alspach, K. Hashimoto, N. Kuppuswamy, R. Tedrake, N. Kuppuswarny, and R. Tedrake, “Soft-bubble: A highly compliant dense geometry tactile sensor for robot manipulation,” *RoboSoft 2019 - 2019 IEEE International Conference on Soft Robotics*, pp. 597–604, Apr. 2019, DOI: 10.1109/ROBOSOFT.2019.8722713

[11] Y. Yan, Z. Hu, Z. Yang, W. Yuan, C. Song, J. Pan, and Y. Shen, “Soft magnetic skin for super-resolution tactile sensing with force self-decoupling,” *Science Robotics*, vol. 6, no. 51, p. eabc8801, Feb. 2021, DOI: 10.1126/scirobotics.abc8801

[12] J. Park, M. Kim, Y. Lee, H. S. Lee, and H. Ko, “Fingertip skin-inspired microstructured ferroelectric skins discriminate static/dynamic pressure and temperature stimuli,” *Science Advances*, vol. 1, no. 9, pp. e1500661–e1500661, 2015, DOI: 10.1126/sciadv.1500661

[13] Z. Zou, C. Zhu, Y. Li, X. Lei, W. Zhang, and J. Xiao, “Rehealable, fully recyclable, and malleable electronic skin enabled by dynamic covalent thermoset nanocomposite,” *Science Advances*, vol. 4, no. 2, pp. 1–9, 2018, DOI: 10.1126/sciadv.aaq0508

[14] C. Mu, Y. Song, W. Huang, A. Ran, R. Sun, W. Xie, and H. Zhang, “Flexible Normal-Tangential Force Sensor with Opposite Resistance Responding for Highly Sensitive Artificial Skin,” *Advanced Functional Materials*, vol. 28, no. 18, May 2018, DOI: 10.1002/adfm.201707503

[15] C. W. Ma, L. S. Hsu, J. C. Kuo, and Y. J. Yang, "A flexible tactile and shear sensing array fabricated using a novel buckypaper patterning technique," *Sensors and Actuators, A: Physical*, vol. 231, pp. 21–27, 2015, DOI: 10.1016/j.sna.2014.09.016

[16] X. Sun, J. Sun, T. Li, S. Zheng, C. Wang, W. Tan, J. Zhang, C. Liu, T. Ma, Z. Qi, C. Liu, and N. Xue, "Flexible Tactile Electronic Skin Sensor with 3D Force Detection Based on Porous CNTs/PDMS Nanocomposites," *Nano-Micro Letters*, vol. 11, no. 1, Dec. 2019, DOI: 10.1007/s40820-019-0288-7

[17] M. K. Kang, S. Lee, and J. H. Kim, "Shape optimization of a mechanically decoupled six-axis force/torque sensor," *Sensors and Actuators, A: Physical*, vol. 209, pp. 41–51, 2014, DOI: 10.1016/j.sna.2014.01.001

[18] J. Zhang, L. J. Zhou, H. M. Zhang, Z. X. Zhao, S. L. Dong, S. Wei, J. Zhao, Z. L. Wang, B. Guo, and P. A. Hu, "Highly sensitive flexible three-axis tactile sensors based on the interface contact resistance of microstructured graphene," *Nanoscale*, vol. 10, no. 16, pp. 7387–7395, 2018, DOI: 10.1039/c7nr09149d

[19] N. F. Lepora, U. Martinez-Hernandez, M. Evans, L. Natale, G. Metta, and T. J. Prescott, "Tactile Superresolution and Biomimetic Hyperacuity," *IEEE Transactions on Robotics*, vol. 31, no. 3, pp. 605–618, 2015, DOI: 10.1109/TRO.2015.2414135

[20] C. M. Boutry, M. Negre, M. Jorda, O. Vardoulis, A. Chortos, O. Khatib, and Z. Bao, "A hierarchically patterned, bioinspired e-skin able to detect the direction of applied pressure for robotics," *Science Robotics*, vol. 3, no. 24, pp. 1–10, Nov. 2018, DOI: 10.1126/scirobotics.aau6914

[21] L. Viry, A. Levi, M. Totaro, A. Mondini, V. Mattoli, B. Mazzolai, and L. Beccai, "Flexible Three-Axial Force Sensor for Soft and Highly Sensitive Artificial Touch,"

Advanced Materials, vol. 26, no. 17, pp. 2659–2664, May 2014, DOI: 10.1002/adma.201305064

[22] H. K. Lee, J. Chung, S. Il Chang, and E. Yoon, “Real-time measurement of the three-axis contact force distribution using a flexible capacitive polymer tactile sensor,” *Journal of Micromechanics and Microengineering*, vol. 21, no. 3, Mar. 2011, DOI: 10.1088/0960-1317/21/3/035010

[23] Z. Chu, P. M. Sarro, and S. Middelhoek, “Silicon three-axial tactile sensor,” *Sensors and Actuators, A: Physical*, vol. 54, no. 1–3, pp. 505–510, 1996, DOI: 10.1016/S0924-4247(95)01190-0

[24] B. Ward-Cherrier, N. Pestell, L. Cramphorn, B. Winstone, M. E. Giannaccini, J. Rossiter, and N. F. Lepora, “The TacTip Family: Soft Optical Tactile Sensors with 3D-Printed Biomimetic Morphologies,” *Soft Robotics*, vol. 5, no. 2, pp. 216–227, Apr. 2018, DOI: 10.1089/soro.2017.0052

[25] G. Palli, L. Moriello, U. Scarcia, and C. Melchiorri, “Development of an optoelectronic 6-axis force/torque sensor for robotic applications,” *Sensors and Actuators, A: Physical*, vol. 220, pp. 333–346, Dec. 2014, DOI: 10.1016/j.sna.2014.09.023

[26] W. Yuan, S. Dong, and E. H. Adelson, “GelSight: High-Resolution Robot Tactile Sensors for Estimating Geometry and Force,” *Sensors*, vol. 17, no. 12, p. 2762, Nov. 2017, DOI: 10.3390/s17122762

[27] H. Wang, G. De Boer, J. Kow, A. Alazmani, M. Ghajari, R. Hewson, and P. Culmer, “Design methodology for magnetic field-based soft tri-axis tactile sensors,” *Sensors (Switzerland)*, vol. 16, no. 9, 2016, DOI: 10.3390/s16091356

[28] C. Ledermann, S. Wirges, D. Oertel, M. Mende, and H. Woern, “Tactile sensor on a

magnetic basis using novel 3D Hall sensor - First prototypes and results," *INES 2013 - IEEE 17th International Conference on Intelligent Engineering Systems, Proceedings*, pp. 55–60, 2013, DOI: 10.1109/INES.2013.6632782

[29] T. P. Tomo, M. Regoli, A. Schmitz, L. Natale, H. Kristanto, S. Somlor, L. Jamone, G. Metta, and S. Sugano, "A New Silicone Structure for uSkin - A Soft, Distributed, Digital 3-Axis Skin Sensor and Its Integration on the Humanoid Robot iCub," *IEEE Robotics and Automation Letters*, vol. 3, no. 3, pp. 2584–2591, 2018, DOI: 10.1109/LRA.2018.2812915

[30] Y. Wu, Y. Liu, Y. Zhou, Q. Man, C. Hu, W. Asghar, F. Li, Z. Yu, J. Shang, G. Liu, M. Liao, and R. W. Li, "A skin-inspired tactile sensor for smart prosthetics," *Science Robotics*, vol. 3, no. 22, pp. 1–9, 2018, DOI: 10.1126/scirobotics.aat0429

[31] J. Ge, X. Wang, M. Drack, O. Volkov, M. Liang, G. S. Cañón Bermúdez, R. Illing, C. Wang, S. Zhou, J. Fassbender, M. Kaltenbrunner, and D. Makarov, "A bimodal soft electronic skin for tactile and touchless interaction in real time," *Nature Communications*, vol. 10, no. 1, pp. 1–10, 2019, DOI: 10.1038/s41467-019-12303-5

[32] P. Piacenza, S. Sherman, and M. Ciocarlie, "Data-Driven Super-Resolution on a Tactile Dome," *IEEE Robotics and Automation Letters*, vol. 3, no. 3, pp. 1434–1441, Jul. 2018, DOI: 10.1109/LRA.2018.2800081

[33] Y. Zhao, Y. Liu, Y. Li, and Q. Hao, "Development and application of resistance strain force sensors," *Sensors (Switzerland)*, vol. 20, no. 20, pp. 1–18, 2020, DOI: 10.3390/s20205826

[34] W. Kester, *Strain, Force, Pressure and Flow Measurements*. Analog Devices, Inc., 2005. DOI: 10.1016/B978-075067844-5/50131-4

[35] K. Yellapantula, H. Devaraj, M. Assadian, L. Stuart, C. Y. Lo, W. C. Gan, and K. Aw,

"Soft and flexible sensor array using carbon black pillars for object recognition via pressure mapping," *Measurement: Journal of the International Measurement Confederation*, vol. 159, p. 107781, 2020, DOI: 10.1016/j.measurement.2020.107781

[36] Hyung-Kew Lee, Jaehoon Chung, Sun-Il Chang, and Euisik Yoon, "Normal and Shear Force Measurement Using a Flexible Polymer Tactile Sensor With Embedded Multiple Capacitors," *Journal of Microelectromechanical Systems*, vol. 17, no. 4, pp. 934–942, Aug. 2008, DOI: 10.1109/JMEMS.2008.921727

[37] C. Sferrazza, A. Wahlsten, C. Trueeb, and R. D'Andrea, "Ground Truth Force Distribution for Learning-Based Tactile Sensing: A Finite Element Approach," *IEEE Access*, vol. 7, pp. 173438–173449, 2019, DOI: 10.1109/ACCESS.2019.2956882

[38] C. Pan, L. Dong, G. Zhu, S. Niu, R. Yu, Q. Yang, Y. Liu, and Z. L. Wang, "High-resolution electroluminescent imaging of pressure distribution using a piezoelectric nanowire LED array," *Nature Photonics*, vol. 7, no. 9, pp. 752–758, Sep. 2013, DOI: 10.1038/nphoton.2013.191

[39] H. Khamis, B. Xia, and S. J. Redmond, "A novel optical 3D force and displacement sensor – Towards instrumenting the PapillArray tactile sensor," *Sensors and Actuators, A: Physical*, vol. 291, pp. 174–187, 2019, DOI: 10.1016/j.sna.2019.03.051

[40] S. Samuel, A. Kumar, and C. K. Mukhopadhyay, "Fiber Bragg grating tactile sensor for imaging," *Optik*, vol. 198, no. May, p. 163062, 2019, DOI: 10.1016/j.ijleo.2019.163062

[41] E. Lee, J. Kim, and T. K. An, "Direct growth of CVD graphene on 3D-architectured substrates for highly stable tactile sensors," *Chinese Journal of Physics*, vol. 67, pp. 569–575, Oct. 2020, DOI: 10.1016/j.cjph.2020.08.006

[42] Y. Liu, R. Bao, J. Tao, J. Li, M. Dong, and C. Pan, "Recent progress in tactile sensors and

their applications in intelligent systems," *Science Bulletin*, vol. 65, no. 1, pp. 70–88, 2020, DOI: 10.1016/j.scib.2019.10.021

[43] J. Wang, J. Jiang, C. Zhang, M. Sun, S. Han, R. Zhang, N. Liang, D. Sun, and H. Liu, "Energy-efficient, fully flexible, high-performance tactile sensor based on piezotronic effect: Piezoelectric signal amplified with organic field-effect transistors," *Nano Energy*, vol. 76, no. April, p. 105050, 2020, DOI: 10.1016/j.nanoen.2020.105050

[44] Y. Chen, Y. Liu, J. Ren, W. Yang, E. Shang, K. Ma, L. Zhang, J. Jiang, and X. Sun, "Conformable core-shell fiber tactile sensor by continuous tubular deposition modeling with water-based sacrificial coaxial writing," *Materials and Design*, vol. 190, p. 108567, 2020, DOI: 10.1016/j.matdes.2020.108567

[45] U. Büyükşahin and A. Kırlı, "A low-cost, human-like, high-resolution, tactile sensor based on optical fibers and an image sensor," *International Journal of Advanced Robotic Systems*, vol. 15, no. 4, pp. 1–13, 2018, DOI: 10.1177/1729881418783631

[46] J. Missinne, E. Bosman, B. Van Hoe, R. Verplancke, G. Van Steenberge, S. Kalathimekkad, P. Van Daele, and V. Jan, "Ultra thin optical tactile shear sensor," *Procedia Engineering*, vol. 25, pp. 1393–1396, 2011, DOI: 10.1016/j.proeng.2011.12.344

[47] A. H. Esa, B. Ali, and M. A. Ayub, "Normal force calibration for optical based silicone tactile sensor," *Procedia Engineering*, vol. 41, no. Iris, pp. 210–215, 2012, DOI: 10.1016/j.proeng.2012.07.164

[48] M. Ohka, A. Tsunogai, T. Kayaba, S. C. Abdullah, and H. Yussof, "Advanced design of columnar-conical feeler-type optical three-axis tactile sensor," *Procedia Computer Science*, vol. 42, no. C, pp. 17–24, 2014, DOI: 10.1016/j.procs.2014.11.028

[49] A. Takagi, Y. Yamamoto, M. Ohka, H. Yussof, and S. C. Abdullah, "Sensitivity-

enhancing All-in-type Optical Three-axis Tactile Sensor Mounted on Articulated Robotic Fingers," *Procedia Computer Science*, vol. 76, no. Iris, pp. 95–100, 2015, DOI: 10.1016/j.procs.2015.12.286

[50] R. Ahmadi, S. Arbatani, J. Ozhikandathil, M. Packirisamy, and J. Dargahi, "A multi-purpose optical microsystem for static and dynamic tactile sensing," *Sensors and Actuators, A: Physical*, vol. 235, pp. 37–47, 2015, DOI: 10.1016/j.sna.2015.09.035

[51] H. Zhang, D. Peng, W. Wang, L. Dong, and C. Pan, "Mechanically Induced Light Emission and Infrared-Laser-Induced Upconversion in the Er-Doped CaZnOS Multifunctional Piezoelectric Semiconductor for Optical Pressure and Temperature Sensing," *Journal of Physical Chemistry C*, vol. 119, no. 50, pp. 28136–28142, 2015, DOI: 10.1021/acs.jpcc.5b10302

[52] E. Fujiwara, Y. T. Wu, M. F. M. dos Santos, E. A. Schenkel, and C. K. Suzuki, "Development of a tactile sensor based on optical fiber specklegram analysis and sensor data fusion technique," *Sensors and Actuators A: Physical*, vol. 263, pp. 677–686, Aug. 2017, DOI: 10.1016/j.sna.2017.07.031

[53] X. Wang, M. Que, M. Chen, X. Han, X. Li, C. Pan, and Z. L. Wang, "Full Dynamic-Range Pressure Sensor Matrix Based on Optical and Electrical Dual-Mode Sensing," *Advanced Materials*, vol. 29, no. 15, p. 1605817, Apr. 2017, DOI: 10.1002/adma.201605817

[54] A. R. Ian H. Taylor, Siyuan Dong, I. Taylor, S. Dong, and A. Rodriguez, "GelSlim3.0: High-Resolution Measurement of Shape, Force and Slip in a Compact Tactile-Sensing Finger," *arXiv*, vol. 2103.12269, pp. 10781–10787, Mar. 2021, Accessed: Dec. 15, 2021. [Online]. Available: http://arxiv.org/abs/2103.12269

[55] A. Yamaguchi, C. G. Atkeson, S. Asano, M. Muroyama, T. Nakayama, Y. Hata, and S. Tanaka, “Combining Finger Vision and Optical Tactile Sensing: Reducing and Handling Errors While Cutting Vegetables,” *Humanoid2017*, vol. 2, pp. 516–519, 2017.

[56] M. Bauza, E. Valls, B. Lim, T. Sechopoulos, and A. Rodriguez, “Tactile Object Pose Estimation from the First Touch with Geometric Contact Rendering,” no. CoRL, 2020, [Online]. Available: http://arxiv.org/abs/2012.05205

[57] N. Kuppuswamy, A. Alspach, A. Uttamchandani, S. Creasey, T. Ikeda, and R. Tedrake, “Soft-bubble grippers for robust and perceptive manipulation,” *IEEE International Conference on Intelligent Robots and Systems*, pp. 9917–9924, 2020, DOI: 10.1109/IROS45743.2020.9341534

[58] A. Yamaguchi and C. G. Atkeson, “Implementing tactile behaviors using FingerVision,” *IEEE-RAS International Conference on Humanoid Robots*, pp. 241–248, 2017, DOI: 10.1109/HUMANOIDS.2017.8246881

[59] D. Ma, E. Donlon, S. Dong, and A. Rodriguez, “Dense tactile force estimation using gelslim and inverse FEM,” *Proceedings - IEEE International Conference on Robotics and Automation*, vol. 2019-May, pp. 5418–5424, 2019, DOI: 10.1109/ICRA.2019.8794113

[60] S. Dong, D. Ma, E. Donlon, and A. Rodriguez, “Maintaining grasps within slipping bounds by monitoring incipient slip,” in *2019 International Conference on Robotics and Automation (ICRA)*, May 2019, vol. 2019-May, no. October 2018, pp. 3818–3824. DOI: 10.1109/ICRA.2019.8793538

[61] J. Park, Y. Lee, J. Hong, Y. Lee, M. Ha, Y. Jung, H. Lim, S. Y. Kim, and H. Ko, “Tactile-Direction-Sensitive and Stretchable Electronic Skins Based on Human-Skin-Inspired Interlocked Microstructures,” *ACS Nano*, vol. 8, no. 12, pp. 12020–12029, Dec. 2014,

DOI: 10.1021/nn505953t

[62] A. Chortos, J. Liu, and Z. Bao, “Pursuing prosthetic electronic skin.,” *Nature materials*, vol. 15, no. July, p. 937, Sep. 2016, DOI: 10.1038/nmat4671

[63] S. Toyama, S. Shirogane, T. Nakamura, K. Watanabe, and K. Hara, “Development of Thin Shear Force Sensor Aimed at Improving QOL for Persons with Disabilities,” in *EUROSENSORS 2018*, Dec. 2018, vol. 2, no. 13, p. 704. DOI: 10.3390/proceedings2130704

[64] S. Toyama, Y. Tanaka, S. Shirogane, T. Nakamura, T. Umino, R. Uehara, T. Okamoto, and H. Igarashi, “Development of wearable sheet-type shear force sensor and measurement system that is insusceptible to temperature and pressure,” *Sensors (Switzerland)*, vol. 17, no. 8, Aug. 2017, DOI: 10.3390/s17081752

[65] A. Weckenmann, G. Peggs, and J. Hoffmann, “Probing systems for dimensional micro- and nano-metrology,” *Measurement Science and Technology*, vol. 17, no. 3, pp. 504–509, Mar. 2006, DOI: 10.1088/0957-0233/17/3/S08

[66] E. Peiner, M. Balke, and L. Doering, “Form measurement inside fuel injector nozzle spray holes,” *Microelectronic Engineering*, vol. 86, no. 4–6, pp. 984–986, Apr. 2009, DOI: 10.1016/j.mee.2008.12.016

[67] P. Bingger, M. Zens, and P. Woias, “Highly flexible capacitive strain gauge for continuous long-term blood pressure monitoring,” *Biomedical Microdevices*, vol. 14, no. 3, pp. 573–581, Jun. 2012, DOI: 10.1007/s10544-012-9636-9

[68] L. Löfdahl and M. Gad-el-Hak, “MEMS-based pressure and shear stress sensors for turbulent flows,” *Measurement Science and Technology*, vol. 10, no. 8, pp. 665–686, Aug. 1999, DOI: 10.1088/0957-0233/10/8/302

[69] J. Dargahi and S. Najarian, "Human tactile perception as a standard for artificial tactile sensing - a review," *International Journal of Medical Robotics and Computer Assisted Surgery*, vol. 01, no. 01, p. 23, 2004, DOI: 10.1581/mrcas.2004.010109

[70] X. Wang, H. Zhang, R. Yu, L. Dong, D. Peng, A. Zhang, Y. Zhang, H. Liu, C. Pan, and Z. L. Wang, "Dynamic pressure mapping of personalized handwriting by a flexible sensor matrix based on the mechanoluminescence process," *Advanced Materials*, vol. 27, no. 14, pp. 2324–2331, 2015, DOI: 10.1002/adma.201405826

[71] J. Sui, K. Chung, F. Tian, and P.-C. C. Ku, "A tensorial shear stress sensor based on light-emitting GaN nanopillars," *Applied Physics Letters*, vol. 115, no. 2, p. 021103, Jul. 2019, DOI: 10.1063/1.5111129

[72] N. Dvořák, K. Chung, K. Mueller, and P. C. Ku, "Ultrathin Tactile Sensors with Directional Sensitivity and a High Spatial Resolution," *Nano Letters*, vol. 21, no. 19, pp. 8304–8310, 2021, DOI: 10.1021/acs.nanolett.1c02837

[73] L. Zhang, L. K. Lee, C. H. Teng, T. A. Hill, P. C. Ku, and H. Deng, "How much better are InGaN/GaN nanodisks than quantum wells - Oscillator strength enhancement and changes in optical properties," *Applied Physics Letters*, vol. 104, no. 5, 2014, DOI: 10.1063/1.4864083

[74] Q. Zheng, M. Peng, Z. Liu, S. Li, R. Han, H. Ouyang, Y. Fan, C. Pan, W. Hu, J. Zhai, Z. Li, and Z. L. Wang, "Dynamic real-time imaging of living cell traction force by piezo-phototronic light nano-antenna array," *Science Advances*, vol. 7, no. 22, pp. 1–9, May 2021, DOI: 10.1126/sciadv.abe7738

[75] N. Dvořák, N. Fazeli, and P. Ku, "Direct Shear Stress Mapping Using a Gallium Nitride LED-Based Tactile Sensor," *Micromachines*, vol. 14, no. 916, pp. 1–8, 2023, DOI:

10.3390/mi14050916

[76] N. A. Dvořák and P. C. Ku, “Low-Profile Shear Force Tactile Sensor Based on Optical Methods,” *IEEE Electron Device Letters*, vol. 43, no. 7, pp. 1081–1084, 2022, DOI: 10.1109/LED.2022.3174096

[77] N. A. Dvořák, K. Chung, K. Mueller, and P.-C. Ku, “Mapping tensorial shear stress with light-emitting GaN nanopillars,” *Proceedings of SPIE - The International Society for Optical Engineering*, vol. 11686, 2021, DOI: 10.1117/12.2577640

[78] N. Dvořák, N. Fazeli, and P. C. Ku, “Direct Shear Stress Mapping Using a Gallium Nitride LED-Based Tactile Sensor,” *Micromachines*, vol. 14, no. 5, p. 916, 2023, DOI: 10.3390/mi14050916

[79] J. Chen and W. D. Brewer, “Ohmic Contacts on p-GaN,” *Advanced Electronic Materials*, vol. 1, no. 8, Aug. 2015, DOI: 10.1002/aelm.201500113

[80] C. Huh, S. W. Kim, H. M. Kim, D. J. Kim, and S. J. Park, “Effect of alcohol-based sulfur treatment on Pt Ohmic contacts to p-type GaN,” *Applied Physics Letters*, vol. 78, no. 13, pp. 1942–1944, Mar. 2001, DOI: 10.1063/1.1358356

[81] J.-S. Jang, S.-J. Park, and T.-Y. Seong, “Formation of low resistance Pt ohmic contacts to p-type GaN using two-step surface treatment,” *Journal of Vacuum Science & Technology B: Microelectronics and Nanometer Structures*, vol. 17, no. 6, p. 2667, 1999, DOI: 10.1116/1.591045

[82] N. A. Dvorak and P. C. Ku, “Low-Profile Shear Force Tactile Sensor Based on Optical Methods,” *IEEE Electron Device Letters*, vol. 43, no. 7, pp. 1081–1084, 2022, DOI: 10.1109/LED.2022.3174096

[83] A. Savitzky and M. J. E, “Smoothing and Differentiation of Data by Simplified Least

Squares Procedures," 1951. [Online]. Available: https://pubs.acs.org/sharingguidelines

[84] K. Chung, J. Sui, B. Demory, C.-H. Teng, and P.-C. Ku, "Monolithic integration of individually addressable light-emitting diode color pixels," *Applied Physics Letters*, vol. 110, no. 11, Mar. 2017, DOI: 10.1063/1.4978554

[85] R. S. Johansson and J. R. Flanagan, "Coding and use of tactile signals from the fingertips in object manipulation tasks," *Nature Reviews Neuroscience*, vol. 10, no. 5, pp. 345–359, 2009, DOI: 10.1038/nrn2621

[86] G. Robles-De-La-Torre, "Comparing the role of lateral force during active and passive touch: Lateral force and its correlates are inherently ambiguous cues for shape perception under passive touch conditions," *Proceedings of eurohaptics*, pp. 159–164, 2002.

[87] A. Russomanno, S. O'Modhrain, R. B. Gillespie, and M. W. M. Rodger, "Refreshing refreshable braille displays," *IEEE Transactions on Haptics*, vol. 8, no. 3, pp. 287–297, 2015, DOI: 10.1109/TOH.2015.2423492